AN EXPERIMENTAL INVESTIGATION OF THE EFFECT OF TEMPORAL EQUIVALENCE RATIO FLUCTUATIONS ON NO_x EMISSIONS IN PREMIXED FLAMES

by

Douglas Allen Wirth

Dissertation submitted to the Faculty of the

Virginia Polytechnic Institute and State University

in partial fulfillment of the requirements for the degree of

Doctor of Philosophy

in

Mechanical Engineering

APPROVED

J. Robert Mahan, Chairman

David L. Cox

L. Berkley Davis

Larry A. Roe

Richard J. Roby

Uri Vandsburger

October, 1993

Blacksburg, Virginia

c.2

LD
5655
V856
1992
W578
c.2

AN EXPERIMENTAL INVESTIGATION OF THE EFFECT OF TEMPORAL EQUIVALENCE RATIO FLUCTUATIONS ON NO_x EMISSIONS IN PREMIXED FLAMES

by

Douglas Allen Wirth

J. Robert Mahan, Chairman

Mechanical Engineering

(ABSTRACT)

The effect of temporal variations in equivalence ratio on the NO_x emissions of a premixed methane-air flame was measured in a burner. The NO_x emissions are compared among steady flames with spatially uniform equivalence ratio distributions, steady flames with spatially nonuniform equivalence ratio distributions, and unsteady flames with temporal equivalence ratio fluctuations. Time-varying equivalence ratio was measured optically, time-varying temperatures were measured with thermocouples, and mean NO_x emissions were measured by probe sampling and a chemiluminescent analyzer. These measurements quantify the effect of temporal unsteadiness and spatial nonuniformity of equivalence ratio on NO_x emissions.

For lean flames, both spatial nonuniformities and temporal fluctuations in equivalence ratio contribute to an increase in NO_x emissions with respect to steady

uniform flames at the same mean flame temperatures. For lean flames, higher amplitude temperature fluctuations result in larger increases in NO_x with respect to steady flames. The dissertation also describes the optical technique for nonintrusive temporal measurements of equivalence ratio fluctuations and techniques for thermocouple compensation at frequencies up to 10 Hz.

ACKNOWLEDGEMENTS

I would first like to thank my advisory committee chairman, Dr. J. Robert Mahan, for his guidance and mentorship. In particular, I must acknowledge his role in broadening my education in the areas of combustion pressure dynamics, signal processing, and French culture. A six-month stay at the *Ecole Centrale Paris* was the highlight of my graduate school experience, and I am grateful for his efforts on my behalf in arranging it.

I would also like to thank the gentlemen who have generously served on my advisory committee: Professors David Cox, Larry Roe, and Uri Vandsburger of Virginia Tech, Dr. Rick Roby of Hughes Associates, and Dr. L. Berkley Davis of General Electric. I would especially like to thank Dr. Davis for providing the financial support for the research. I thank Professor Uri Vandsburger for his valuable and frequent advice on experimental techniques. Finally, I owe a great debt to Dr. Rick Roby for his expert advice on NO_x kinetics and for his guidance during my master's research, which prepared me well for Cornell and for the current research.

I am indebted to Mr. Ben Poe for his cheerful support of my experiments and for his valiant efforts against uncooperative PCs. My advisors at Cornell, Professor Fred Gouldin and Professor George Wolga, were responsible for many experiences that I feel

greatly enhanced my graduate studies, particularly the study of infrared spectroscopy. Dr. Sébastien Candel and Dr. Nasser Darabiha of *Ecole Centrale Paris* improved my knowledge of combustion modeling, an invaluable experience for an experimentalist. I gratefully acknowledge the French Embassy to the United States and M. François Armanet for granting me the "Sejour Scientifique de Haut Niveau."

One of the most enjoyable aspects of graduate school is the companionship of my fellow graduate students. I have quite a few to thank for their friendship and help over the past six years: Dave Foss, Andrew Hamer, Mike Skelly, Dan Gottuk, David Pastel, Michelle Peatross, James Reaney, Jim Hunderup, Linda Blevins, Robert Aftel, Paulus Bucher, Steve LePera, Pierre Villeneuve, Martial Haeffelin, and Nour Tira.

I owe all success to my parents, who instilled in me the desire to do my best, to be persistent, and to work hard because it's the right thing to do. Finally, I would not have been able to complete this quest for the Ph.D. without the support of my wonderful wife Suzanne.

TABLE OF CONTENTS

Page

ABSTRACT ii

ACKNOWLEDGEMENTS iv

TABLE OF CONTENTS vi

LIST OF FIGURES xi

LIST OF TABLES xv

NOMENCLATURE xvi

INTRODUCTION 1

1.1 MOTIVATION 1

1.2 LITERATURE REVIEW 3

1.3 SUMMARY OF THE EXPERIMENT 26

EXPERIMENTAL APPARATUS 31

2.1 OVERVIEW 31

2.2 TYPES OF FLAMES STUDIED 34

2.3 ROTAMETER CALIBRATIONS 36

2.4 GAS CYLINDERS 39

2.5 OPTICAL MEASUREMENTS 41

2.5.1 Extinction Theory 41

2.5.2 Optical Components 43

2.5.3 Calibration of The Optical System 47

2.6 GAS ANALYZERS AND SAMPLING 49

2.6.1 Sampling System 49

2.6.2 The NO_x Analyzer 51

2.6.3 The THC Analyzer 52

2.6.4 Spatial Equivalence Ratio Measurements 54

2.7 THERMOCOUPLES 56

2.7.1 Temperature Measurement System 56

2.7.2 Thermocouple Probes 58

2.7.3 Thermocouple Modeling 60

2.7.4 The Model 61

2.7.5 Thermocouple Cool-Down Tests 63

2.7.6 Thermocouple Temperature Corrections 66

2.7.7 Thermocouple Frequency Response 70

2.8 PULSE BURNERS 72

2.8.1 Design and Development 72

2.8.2 Version One: Solenoid Valve Burner 80

2.8.3 Version Two: Coaxial Twist Burner 85

2.8.4 Version Three: Cam-Driven Burner 87

2.9 DATA ACQUISITION 91

RESULTS 93

3.1 CALIBRATION OF OPTICAL SYSTEM 93

3.2 STEADY, HOMOGENEOUSLY PREMIXED FLAMES 96

3.3 STEADY, SPATIALLY NONUNIFORM FLAMES 104

3.3.1 Spatial Equivalence Ratio Distributions 104

3.3.2 Comparison to Homogeneously Premixed Flames 111

3.4 PULSING FLAMES 115

3.4.1 Temperature Trends 123

3.4.2 Equivalence Ratio Fluctuations 125

3.4.3 Comparison to Other Flames 127

DISCUSSION AND INTERPRETATION OF RESULTS 134

4.1 EMPIRICAL MODEL USING EQUIVALENCE RATIO DISTRIBUTIONS 135

4.2 EMPIRICAL MODEL USING TEMPERATURE FLUCTUATIONS 148

4.2.1 Extrapolation Procedure 149

4.2.2 Results of Extrapolation 152

4.2.3 Optically Estimated Flame Temperatures 159

4.2.4 Temporal Model 164

CONCLUSION 171

5.1 SUMMARY 171

5.2 CONCLUSIONS 172

5.3 RECOMMENDATIONS FOR FUTURE WORK 174

REFERENCES 179

APPENDIX A THERMOCOUPLE TRANSIENT RESPONSE PROGRAM 186

APPENDIX B THERMOCOUPLE TEMPERATURE CORRECTION PROGRAM 190

APPENDIX C SPATIAL EQUIVALENCE RATIO DISTRIBUTIONS . 195

APPENDIX D TEMPERATURE EXTRAPOLATION PROGRAM 198

APPENDIX E UNCERTAINTY ANALYSIS 209

VITA 214

LIST OF FIGURES

Page

Figure 1 Dependence of the Exponential Term of Nitric Oxide Formation Rate on Temperature 6

Figure 2 Schematic of Experimental Apparatus 32

Figure 3 Calibration for Air Rotameter (Matheson Size 6 with Type HA5 Needle Valve, Housing Model FM-1050B-HA) 37

Figure 4 Calibration for Methane Rotameter (Matheson Size 602 with Type HA3 Needle Valve, Housing Model FM-1050B-HA) 38

Figure 5 Optical System for Nonintrusive Equivalence Ratio Measurements 44

Figure 6 Gas Sampling System 50

Figure 7 Sampling Pattern Over Flameholder Screen for Equivalence Ratio Distribution Measurements 55

Figure 8 Construction of Thermocouple Probes 59

Figure 9 Thermocouple Model 62

Figure 10 Thermocouple Cool-Down Tests. 65

Figure 11 Radiation/Conduction Correction Curves for Large and Fine Thermocouples 69

Figure 12 Response of 6.9-mil Fine Thermocouple to Sinusoidally Varying Gas Temperature 71

Figure 13 Methane Diffusion Between Adjacent Pulses 76

Figure 14 Correlations Between NO_x Emissions and Equivalence Ratio or Temperature for Steady Flames 78

Figure 15 Solenoid Valve Burner 81

Figure 16 Control Circuit for Solenoid Valve 83

Figure 17 Coaxial Twist Burner 86

Figure 18 Cam-Driven Burner 88

Figure 19 Cam for Cam-Driven Burner 90

Figure 20 Calibration of Optical Equivalence Ratio Measurement System . . . 94

Figure 21 Experimental Measurements for the Steady Flames 98

Figure 22 Spatial Equivalence Ratio Distribution for Experiment 81 $\bar{\phi} = 1.0, s = 0.08$ 106

Figure 23 Spatial Equivalence Ratio Distribution for Experiment 82 $\bar{\phi} = 0.79, \ s = 0.06$ 108

Figure 24 Spatial Equivalence Ratio Distribution for Experiment 83 $\bar{\phi} = 0.86, \ s = 0.21$ 109

Figure 25 Spatial Equivalence Ratio Distribution for Experiment 84 $\bar{\phi} = 0.71, \ s = 0.06$ 110

Figure 26 Spatial Equivalence Ratio Distribution for Experiment 87a $\bar{\phi} = 0.78,\ s = 0.13$ 112

Figure 27 Spatial Equivalence Ratio Distribution for Experiment 87b $\bar{\phi} = 0.74,\ s = 0.10$ 113

Figure 28 Comparison of Spatially Nonuniform Flame Measurements to Steady Flames 114

Figure 29 Variation of Nondimensionalized NO_x Emissions with Spatial Unmixedness 116

Figure 30 Spatial Equivalence Ratio Distribution for Experiment 80 $\bar{\phi} = 0.76,\ s = 0.06$ 122

Figure 31 Axial Temperature Profiles in the Pulsing Flames 124

Figure 32 Equivalence Ratio Fluctuations for the Pulsing Flames 126

Figure 33 Comparison of Experimental Measurements from Pulsing, Spatially Nonuniform, and Steady Flames 128

Figure 34 Comparison of Experimental Measurements from Pulsing, Spatially Nonuniform, and Steady Flames. Detail of NO_x Emissions as a Function of Flame Temperature 130

Figure 35 Results of Model for Spatial Nonuniformity of Equivalence Ratio 137

Figure 36 Comparison of Lower and Upper Mean Equivalence Ratio Estimates for Spatially Nonuniform Flames 147

Figure 37 Procedure to Extrapolate Flame Temperatures in Pulsing Flames 150

Figure 38 Autospectrum of Temperature Measurements in Pulsing Flames, Comparison of Original and Extrapolated Autospectra 153

Figure 39 Comparison of Original Fluctuating Temperature Measurements and Extrapolated Estimates of Flame Temperatures 156

Figure 40 Probability Density Functions for the Extrapolated Flame Temperatures of the Pulsing Flames 158

Figure 41 Comparison of Thermocouple-Extrapolated and Equivalence Ratio-Estimated Pulsing Flame Temperatures 160

Figure 42 Comparison of Probability Density Functions for Extrapolated and Optically-Estimated Flame Temperatures 162

Figure 43 Comparison of Autospectra from Thermocouple-Extrapolated and Equivalence Ratio-Estimated Temperatures 163

Figure 44 Prediction of NO_x Emissions from Pulsing Flames 166

LIST OF TABLES

		Page
Table 1	Experimental Data of Richter, Reamer, and Sage [8]	7
Table 2	Steady Homogeneously Premixed Flames	97
Table 3	Steady, Spatially Nonuniform Flames	105
Table 4	Unsteady (Pulsing) Flames	120
Table 5	Comparison of Mean Equivalence Ratio Measurements and Estimates for Spatially Nonuniform Flames	144
Table 6	Evaluation of Gouldin's Inequality Using Pulsing Flame Data	168
Table 7	Spatial Equivalence Ratio Distributions for Experiments 80, 81, 82, and 83	196
Table 8	Spatial Equivalence Ratio Distributions for Experiments 84, 87a, and 87b	197

NOMENCLATURE

A_c	Cross-sectional area (m^2)
A_s	Surface area (m^2)
A(f)	Thermocouple frequency response function (-)
α	Absorption coefficient (m^{-1})
C	Species concentration (-), also capacitance (f)
c	Methane concentration (-)
c′	Methane concentration fluctuation (-)
c_p	Thermocouple junction specific heat ($J \cdot kg^{-1} \cdot K^{-1}$)
D_{AB}	Bimolecular diffusion coefficient ($m^2 \cdot s^{-1}$)
D_1	Thermocouple junction diameter (m)
D_2	Thermocouple lead diameter (m)
E	Activation energy for chemical reaction (J/mol)
E	Uncertainty or random error (-)
ϵ	Emissivity (-)
ϕ	Equivalence ratio (-)
h_1	Convection heat transfer coefficient for a sphere ($W \cdot m^{-2} \cdot K^{-1}$)
h_2	Convection heat transfer coefficient for a cylinder ($W \cdot m^{-2} \cdot K^{-1}$)
I_o	Reference infrared beam intensity (W)
I	Transmitted infrared beam intensity (W)
k	Thermocouple lead thermal conductivity ($W \cdot m^{-1} \cdot K^{-1}$)

L	Path length of infrared beam through medium (m)
λ	Wavelength (m)
P	Perimeter of thermocouple lead; $P = \pi D_2$ (m)
R	Universal gas constant ($J \cdot mol^{-1} \cdot K^{-1}$), also resistance ($\Omega$)
r^2	Correlation coefficient (-)
ρ	Thermocouple junction density (kg/m^3)
s	Unmixedness parameter; $s = \sigma / \bar{\phi}$ (-), also distance in absorbing medium (m)
σ	Standard deviation, also Stephan-Boltzmann constant ($W \cdot m^{-2} \cdot K^{-4}$)
T	Instantaneous temperature (K)
$\bar{T}$	Mean temperature (K)
T'	Temperature fluctuation; $T' = T - \bar{T}$ (K)
T_c	Thermocouple junction temperature (K)
T_{fin}	Thermocouple lead (fin) temperature (K)
T_g	Gas temperature (K)
T_w	Wall temperature (surroundings) (K)
t	Time (s)
τ	Time delay (s)
U	Unmixedness parameter (-) [26]
V	Thermocouple junction volume (m^3), also flow velocity (m/s)

CHAPTER 1

INTRODUCTION

1.1 MOTIVATION

Gas turbine power plants can achieve tens of parts per million or less of nitric oxide emissions with water injection. The gas turbine industry is being driven to achieve the same low emissions in "dry" combustors. Current emissions targets are being met in many regions with natural gas-fueled, premixed combustors operating at 10 atm of pressure. However, as "best available control technology" drives emissions limits lower, the performance targets are becoming increasingly difficult to achieve. Combustor designers are now required to address all aspects of turbulent premixed combustion to control NO_x emissions [1-3].

One aspect of turbulent premixed combustion that requires further attention is the relationship between pressure dynamics and NO_x emissions. Pressure dynamics represents the pressure and related temperature fluctuations associated with acoustic-scale fluctuations in a combustor. General Electric has observed higher NO_x emissions when

their combustors have stronger pressure dynamics, and the presence of dynamics can make the difference between meeting and failing to meet a performance goal. One explanation states that larger acoustic oscillations increase the net rate of the NO_x formation reactions [4]. A second explanation suggests that coupling between the acoustics and the fuel feed system cause fluctuations in the richness of the combustion zone [5]. This second mechanism could potentially produce stronger fluctuations in temperature and chemical species than the first mechanism, and may therefore have a stronger effect on NO_x emissions. The research presented in this dissertation focusses on the second mechanism. Pressure dynamics are decoupled from the problem, and fluctuations in equivalence ratio are considered the direct cause of increased NO_x emissions. This approach is more general, since fluctuations in equivalence ratio can arise from other sources such as turbulent mixing.

The research presented here is a study of the relationship between temporal equivalence ratio fluctuations and NO_x emissions in premixed, laminar combustion of methane in air. The goal is to quantify and explain any effect of the amplitude and frequency of temperature fluctuations on the yield of NO_x, and to compare the influence of temporal equivalence ratio fluctuations to the influence of spatial equivalence ratio nonuniformities within the flame. Whereas spatial nonuniformities are currently measured through probe sampling and gas analysis in industry, the possible effects of temporal equivalence ratio fluctuations have been largely ignored. The current research

experimentally quantifies the importance of temporal effects and develops a nonintrusive optical technique for measuring temporal equivalence ratio fluctuations. In order to put the research into perspective, a literature review follows.

1.2 LITERATURE REVIEW

The following paragraphs summarize the findings of other investigators chronologically. Several early articles report experiments or analytical studies investigating the effect of temperature oscillations on a high activation-energy reaction (i.e. the thermal or Zeldovich NO_x mechanism [6]). However, in some of these studies the effects of varying equivalence ratio or incomplete mixing are not separated from strictly thermal effects. These articles show that mixing and temperature effects cannot be separated in practical combustors, and that the effects of imperfect fuel-air mixing are likely to dominate the effects due to acoustically-driven temperature fluctuations. The focus of the literature review then shifts to articles on turbulent reacting flows, especially the effects of mixing on NO_x emissions.

Perhaps one of the first investigations into the effects of unsteadiness on NO_x production was carried out in 1962 by Richter, Wiese, and Sage [7]. The investigators used a tubular burner with premixed methane-air combustion. They found that as they varied both the stoichiometry and the total flow rate of the reactants, they were able to

change the acoustic conditions in the burner. At near stoichiometric conditions they observed strong pressure oscillations corresponding to the quarter-wave acoustic mode of the burner tube. The frequency of the oscillations increased with the flow rate of fuel and air. At a richer equivalence ratio, they achieved less regular oscillations. Richter et al. correctly summarize the expected effect of temperature oscillations on NO_x emissions when they state:

> During screaming or oscillatory unstable combustion in premixed flames there are regular fluctuations in the measured pressure which sometimes are as large as 20 per cent of the average pressure. Such perturbations introduce a corresponding local change in temperature. As a result the equilibrium and kinetic characteristics of the reaction of nitrogen and oxygen, the increase in temperature associated with the local rise in pressure is favourable to the formation of nitric oxide. The subsequent decrease in pressure tends to freeze the reaction, and the net effect is an increase in the average concentration of the oxides of nitrogen because of the nonlinear effect of temperature on the rate of reaction.

The nonlinear effect of temperature on NO_x emissions is an important concept. It stems from the rate-determining step of the thermal NO_x mechanism,

$$N_2 + O \rightleftarrows NO + N \quad . \tag{1}$$

In most practical combustion systems, the majority of NO_x consists of NO and the majority of NO is formed through the thermal mechanism described by equation (1). The rate of NO formation is given by the Arrhenius-type equation

$$\frac{d[NO]}{dt} = [N_2]\,[O]\,A \exp\left[\frac{-E}{RT}\right] \quad . \tag{2}$$

It is clear from equation (2) that the relationship between NO formation and temperature is nonlinear. Due to the high activation energy E for this particular reaction, the rate of NO formation is very sensitive to small changes in temperature.

Figure 1 shows the dependence of the exponential term on temperature. The dashed lines show the effect of 100 K temperature fluctuations about a mean temperature of 1900 K. When the temperature decreases by 100 K, the rate of NO formation decreases by 67 percent. However, a temperature increase of 100 K increases the NO formation rate by 170 percent. The overall effect of temperature fluctuations is to increase NO emissions relative to a steady flame at the same mean temperature. This concept applies whether the temperature differences are spatial or temporal in nature.

In a subsequent paper, Richter, Reamer, and Sage [8] present more detailed results from the same burner and arrive at more specific conclusions. The results of the experiment are summarized in Table 1. Richter and coworkers conclude that the frequency of the pressure oscillations is the factor controlling NO_x emissions levels, since they observe the highest emissions at the highest frequencies. They are unable to draw clear conclusions based on the amplitude of the oscillations because the lowest amplitudes occur at the intermediate frequencies; the amplitudes do not seem to correlate with the emissions. However, several reasons lead us to disagree with the authors' conclusions. Their neglect of the effect of stoichiometry on NO emissions is particularly important.

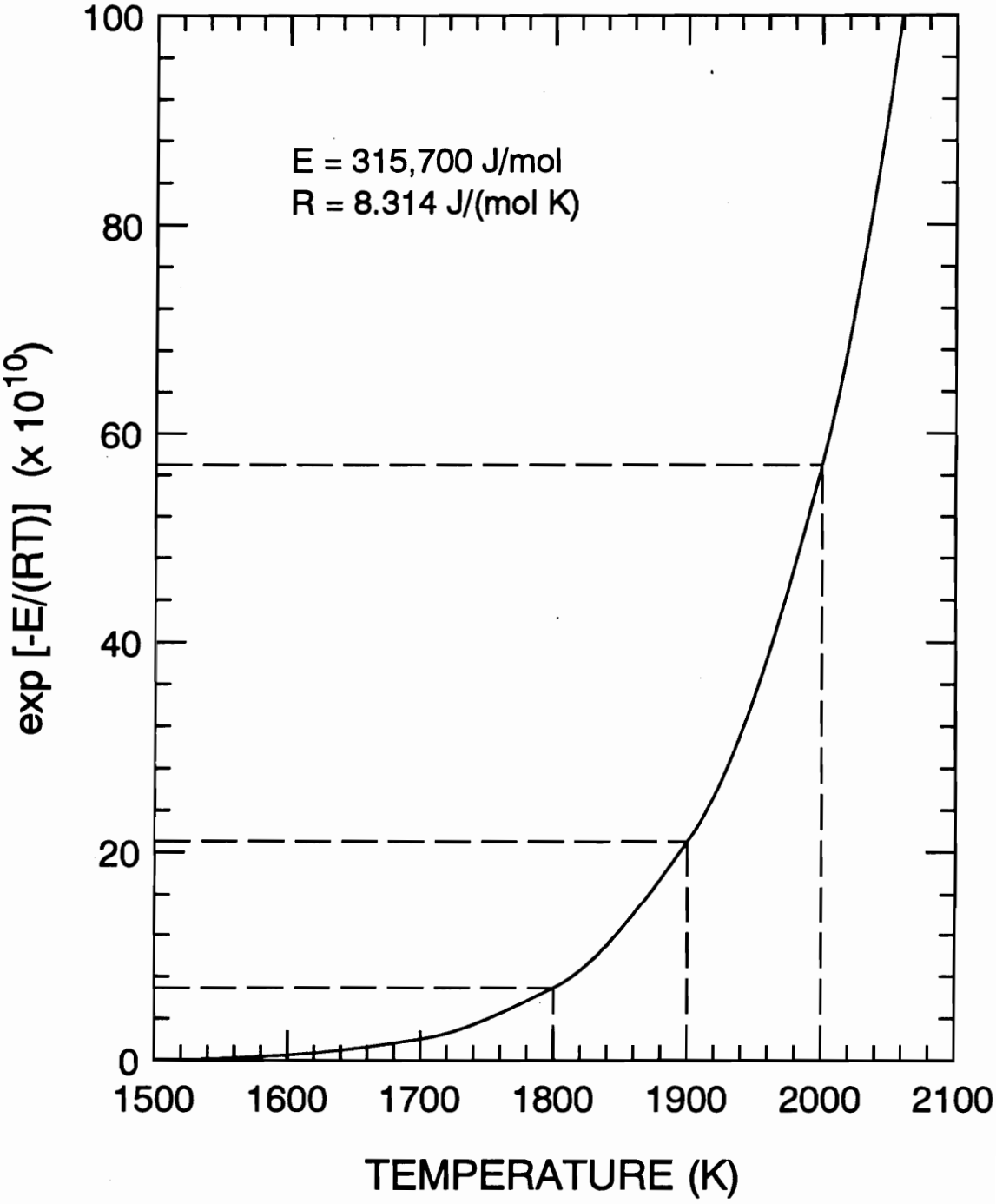

Figure 1 Dependence of the Exponential Term of Nitric Oxide Formation Rate on Temperature

Table 1 Experimental Data of Richter, Reamer, and Sage [8]

EQUIVALENCE RATIO	GAS FLOW RATE	COMBUSTION DESCRIPTION	FREQ. (Hz)	NO_x (ppm)
1.0	LOW	UNSTEADY OSCILLATORY	580	50-60
1.0	HIGH	OSCILLATORY	950	60-70
1.4	MEDIUM	IRREGULAR	28	5-20

It is now known that NO emissions peak near stoichiometric combustion, where the flame temperatures are the highest. The low emissions at an equivalence ratio of 1.4 are explained on this basis. Considering the two cases with stoichiometric equivalence ratios, the data indicate that the combustor temperature was higher for the higher flow rate. At a higher mass flow rate of fuel and air, the combustor would run hotter due to a larger energy release. The speed of sound would be faster under these conditions, and this is reflected in the higher frequency of the acoustic oscillations. The higher NO_x emissions are consistent with higher temperatures in the post-flame zone. In summary, the cited experiment failed to investigate the effect of combustor instabilities on NO_x emissions independently of other factors which are known to strongly affect NO_x emissions.

In 1970, Opsahl and Seagrave modeled Richter et al.'s burner [9]. The burner was modeled as a back-mix reactor flame zone followed by a plug-flow reactor cooling section. They studied the effect of various amplitudes and frequencies of pressure-temperature oscillations on NO_x production. Although the NO_x emissions did respond to changes in the frequency of the oscillations, the effect was stronger for changes in the amplitude of the oscillations. From this, they conclude that "Pressure-temperature oscillations significantly affect the concentrations of several 'trace' components which contribute to air pollution," and "the amplitude of the temperature oscillations seems to be of more importance than the frequency of the oscillations." Opsahl and Seagrave also

object to the conclusions of Richter et al., stating that "the apparent enhancement of total oxides of nitrogen measured by Sage and co-workers is more likely to be due to a shift in the longitudinal temperature profile than to any chemical kinetic phenomena."

In 1971, Fletcher and Heywood developed a model which accounts for nonhomogeneities in equivalence ratio and predict the effect on NO_x emissions [10]. They reason:

> In the primary zone, a mean flow pattern with recirculation ... can be defined. However, substantial turbulent fluctuations about this mean occur, resulting in wide variations in residence time and composition within the zone. The fuel, air, and burnt gases are not uniformly mixed, and parts of the flow are significantly leaner and parts are richer than the mean fuel/air ratio. ... [D]istributions in fuel/air ratio about the mean substantially change the concentrations of major species and flame temperatures, and would be expected to significantly affect nitric oxide formation rates.

Fletcher and Heywood modeled this phenomenon by assuming a normal distribution of equivalence ratios about the mean; the standard deviations were varied to simulate different degrees of "mixedness." The results show that the initial degree of mixedness has a significant effect on NO_x emissions:

> The initial degree of mixedness in the primary zone is predicted to play a significant part in determining the over-all emission level of nitric oxide. Its significance is shown to increase as the equivalence ratio in the primary zone approaches the stoichiometric value. At this point the results suggest that the nitric oxide levels can vary by a factor of at least two with changes in mixing characteristics.

The results also show that when the mean equivalence ratio is stoichiometric, the larger the standard deviation (unmixedness), the lower the emissions. This is analogous to stratified charge combustion in internal combustion engines; burning at either the lean or the rich side of stoichiometric lowers the flame temperature and therefore the NO_x production. However, the results of the model show the opposite effect at lean mean equivalence ratios. At leaner equivalence ratios, the larger the standard deviation, the larger the NO_x emissions. In this case, the deviation toward stoichiometric produces more NO_x than the reduction in NO_x that occurs if the deviation is away from stoichiometric. This is due to the nonlinear effect of temperature on NO formation rates.

The effect of mixing on NO_x emissions was followed up in several papers in 1972. Pompei and Heywood ran a kerosene-fueled liquid-spray burner and measured both CO and NO_x emissions [11]. They found that both pollutants were affected by the degree of mixing (note that they measured only "spatial" unmixedness). The data for NO agree well with Fletcher and Heywood's model. As the nozzle pressure was increased the mixing became more uniform, and as a result emissions decreased for overall lean equivalence ratios and increased for stoichiometric combustion. The measured emissions agree better with a model which takes unmixedness into account than with a model which assumes a homogeneous mixture of reactants.

In another 1972 work, Appleton and Heywood study the relationship between mean equivalence ratio, degree of mixedness, and thermal versus fuel-bound nitrogen NO formation mechanisms [12]. They use the same burner as in the experiment above, and in some cases they dope the kerosene fuel with pyridene to generate fuel NO_x. Fuel NO_x differs from thermal NO_x in its dependence on nitrogen radicals supplied from the fuel itself, rather than from the air. Additionally, fuel NO_x is more chemistry-dependent than temperature-dependent. Appleton and Heywood found that the degree of mixedness affects NO_x emissions. Their conclusions with respect to fuel-bound NO are:

> Experiments using kerosene doped with a small amount of pyridene similarly illustrated that the degree of conversion of fuel nitrogen to NO is strongly influenced by the initial degree of fuel-air mixing. Indeed, the measurements demonstrated that, for good initial mixing, the degree of conversion of fuel nitrogen to NO approached 100% for lean operation and that the NO created from the fuel nitrogen was far in excess of that formed from the nitrogen in the air.

This indicates that there may be a tradeoff between the improved thermal NO_x emissions and worsened fuel-NO_x emissions achieved through better mixing. It cannot be determined from this study whether prompt NO_x (where the source of nitrogen is the combustion air) would be affected by the degree of mixing.

In a third 1972 publication, Thompson et al. study a burner with pressure-temperature oscillations in the 500-1250 Hz range, and conclude that "No significant changes in NO formation, due to oscillations, were observed. [13]" In this case, one must assess what the authors mean by 'significant.' Later in the paper, the authors

support the observation by Opsahl and Seagrave that temperature oscillations should have at least some effect on NO emissions:

> Consider a sinusoidal temperature oscillation as a series of elemental periods during which a certain temperature displacement from the mean occurs. Then, for each element time during one-half cycle, an element occurs exactly one-half cycle later with exactly equal and opposite displacement from the mean. As the reaction rate is nonlinearly temperature dependent, the mean element yield of reaction products during these two element-residence times will exceed the yield from the same residence time at the mean temperature. The gain in yield during one cycle residence will depend on the gain over all such element pairs during a cycle.
>
> In the case of a 134.5-kcal activation-energy reaction in a system undergoing oscillations of 30K half-wave amplitude about a mean of 1950K, the reaction rates for extreme elements are 1.69 and 0.58 x mean temperature rate, and thus the mean rate is (1.69 + 0.58)/2 = 1.13 times the mean temperature rate. For the remainder of the cycle, the gain is smaller, because the temperature displacement is smaller, and hence the over-all gain for oscillations under 30K is insignificant, and, even at 50K, amplitude is only 11%.

The author of this dissertation has analyzed seven runs in the tabulated data where the equivalence ratio is the same (ϕ = 0.92) but the frequency of the oscillations varies. Under quiescent conditions, they measured 48.4 ppm NO. For the oscillatory cases, the mean was 37.8 ppm NO and the standard deviation was 5.9 ppm. This means it is 96 percent certain that the NO measurements are significantly different. The NO yield is not well correlated to the frequency of the oscillations, and the amplitude of the oscillations under the different conditions are not reported (other than that all oscillations were less than 30K). One problem with these data is that the mean temperature for the oscillatory cases varies greatly from the quiescent case, yet the authors claim that there

is no significant effect of oscillatory combustion on emissions. (An insufficient number of data sets at the other equivalence ratios precludes statistical generalizations about means and standard deviations. In only one case out of six are the quiescent and oscillatory NO measurements within 10 percent of each other.) The second problem with the data is that for this experiment, the oscillatory combustion leads to *lower* emissions, in contradiction to Fletcher and Heywood's model. With the large amount of spread in their data, one might suggest that conclusive statements about NO emissions would be inappropriate.

In 1973, Gouldin discussed the characteristics of an ideal combustor [14]. He concludes that emissions of NO_x, CO, unburned hydrocarbons, and soot could be kept very low only if (a) the reactor section is operated at high mass loading rates (high mass flow, low pressure and velocity), and (b) the mixing is perfectly controlled. He refers not only to the degree of mixedness of the reactants, but also to the ability to add secondary air to quench NO_x reactions without quenching CO, unburned hydrocarbons, and soot burnout. From fluid mechanical considerations, Gouldin shows that complete mixing in a practical combustor cannot be achieved without a prohibitively large pressure drop. Vranos reached a similar conclusion in a paper published a year later [15]. While it appears that better mixing can be achieved through smart design of real combustors, "perfectly premixed" combustors may remain a laboratory-scale phenomenon.

Gouldin followed up this work in 1974 with an analysis of the effect of turbulence-induced temperature fluctuations on NO chemistry [16]. He considered the reaction F + O → P, with the Arrhenius-type rate expression d[P]/dt = [F][O] $AT^n \exp(-E/RT)$. This approach is identical to equations (1) and (2). He neglects the effect of turbulent fluctuations in the reactant concentrations and works on the temperature terms. He finds that the effect of turbulent temperature fluctuations can be ignored if

$$\frac{\overline{T'^2}}{\overline{T}^2} \left[\frac{E}{RT} \right]^2 \ll 1 \quad . \tag{3}$$

The temperature fluctuation T' is defined by $T' = T - \overline{T}$, where $\overline{T}$ is the mean temperature and T is the instantaneous temperature. Gouldin then models a hot air jet mixing with a concentric jet of cool air, using an assumed probability density function for the temperature oscillations. He shows that for his test case, the NO yield can increase by an order of magnitude due to temperature fluctuations. Unfortunately, it is difficult to evaluate equation (3) and check its relevance to the previous experiments. Time-resolved temperature measurements are required to test Gouldin's theory.

The next important developments in the study of temperature oscillations on NO formation were reported at the 16th and 17th International Combustion Symposia. In 1976, Semerjian and Vranos discussed an experiment where they allowed Jet-A fuel to

homogeneously mix with the combustion air before reaching a flameholder [17]. Although it was not the primary focus of their investigation, they studied the effect of the combustor acoustics on the NO_x emissions. They state:

> Temperature measurements ... have indicated the presence of large amplitude temperature oscillations .... The effect of these oscillations on NO_x formation has been investigated by using different combustion chamber configurations which have varied the RMS value of the temperature oscillations from 50 to 400 K. However, no corresponding change has been observed in the NO_x levels. This was in agreement with the findings of Thompson et al. Details of this work will be published shortly.

To my knowledge, the details were not subsequently published. This is unfortunate, because their claims seem to require further investigation. Assuming linear acoustic theory and a ratio of specific heats of 1.4, temperature oscillations of 400 K would have to be accompanied by pressure fluctuations of more than 10 psi in an atmospheric pressure burner. This seems unreasonable, and there should be some explanation other than acoustically-induced temperature fluctuations. One must also ask if the differences in NO_x emissions were measureable, but considered 'insignificant' by the authors. As environmental regulations have become more strict, today's researchers have become concerned with increases of only a few parts per million.

Next, Semerjian and co-workers studied the effect of different degrees of mixedness on NO_x emissions [18]. They used the same burner, but moved the fuel injector closer to the flameholder plate to inhibit homogeneous premixing of the

reactants. They measured the spatial equivalence ratio distribution in the plane of the flameholder and estimated the degree of mixedness by the spread of the distribution. Their results agree qualitatively with Fletcher and Heywood's model:

> ...non-uniform introduction of fuel can increase exit plane levels of NO_x, CO, and hydrocarbons significantly relative to premixed flames. In very lean flames the increased level of pollutants are attributed to large statistical fluctuations in local equivalence ratio. In richer flames ($0.6 < \phi < 1.0$), NO_x levels are below premixed levels, while CO levels are higher.

In reference 18, Semerjian et al. do not mention any effects due to oscillatory combustion, nor do they elaborate on their comments in the previous paper. It at least appears that they were able to measure significant changes in NO_x associated with the degree of mixedness at a fixed mean equivalence ratio, but they may not have been able to measure significant changes in NO_x due to acoustic temperature oscillations. One could conclude that mixing effects on NO_x will dominate the thermo-acoustic effects, at least under their experimental conditions.

Lyons reached similar conclusions in 1981 [19]. The distance between the fuel injector and the flameholder was fixed in the burner, and the fuel split among seventeen injection ports was changed to control the uniformity of the final air-fuel distribution. Increased spatial nonuniformity of equivalence ratio produced higher NO_x for flames leaner than $\bar{\phi} = 0.7$, up to a point. For sufficiently severe nonuniformity of equivalence ratio, NO_x emissions were slightly less than their peak value. This is due to the

existence of locally rich regions despite the globally lean equivalence ratio. Based on theoretical considerations, the author claims that at mean equivalence ratios greater than 0.7, any increased spatial nonuniformity should lead to decreased NO_x emissions. This claim was not supported with experimental measurements, however.

In 1982, Noyce and Sheppard performed a similar experiment in a full-scale gas turbine combustor at atmospheric pressure [20]. They used swirl stabilization, which seemed to give their combustor more of a diffusional-burning character than the previously mentioned experiments. They mapped the spatial equivalence ratio distribution across radial planes at different axial locations in the combustor using probe sampling. They found that rich pockets occurred ($\phi > 1$) even when the overall equivalence ratio was very lean ($\phi = 0.25$). Indeed, nonhomogeneities had to be present, because the overall equivalence ratio for two test cases was below the lean flammability limit of $\phi = 0.53$ [22]. The authors found that the NO_x emissions were lower when there was better mixing, and that the degree of mixedness was related to the momentum of the fuel and air jets. The minimum NO_x occurred at an overall equivalence ratio of about 0.5. One would expect the NO_x to have decreased further at lower equivalence ratios, but two factors may have interfered. One factor is the partially diffusional-type burning due to the high unmixedness and very rich regions, which could cause a deviation from the assumed "premixed" combustion. The other factor is that the momentum of the fuel jet decreases with the overall equivalence ratio, so that the

intensity of turbulent mixing decreases along with the equivalence ratio. The minimum CO occurred at an overall equivalence ratio of about 0.35, which suggests that it may not be possible to minimize both CO and NO_x emissions in the same burner [4].

In 1987, Hegde et al. studied the interaction of combustor acoustics, fluid mechanics, and combustion [23]. They used a dump-style combustor and used a heated wire as the flameholder. They observed that burning vortices were shed from the wire at the fundamental acoustic frequency of the combustor. As the equivalence ratio was increased toward stoichiometric, the strength of the interaction increased in response to the higher heat release rate. The authors found that Rayleigh's criterion was satisfied in the burner. They conclude that "... it is believed that the interactions between the fluid mechanical instability of the flame and the system's acoustic field affect the heat release rates from the flame and provide a mechanism for the driving of longitudinal mode instabilities." These results could have several significant consequences. First of all, it is possible that Semerjian and Vranos [17] were measuring the temperature of convected burning vortices when they reported temperature fluctuations of 400 K. A second important point is the correlation between acoustics and fluctuating heat release rates. This implies that the temperature and chemistry in the flame zone can vary with time, and the source of the temperature fluctuations is not necessarily limited to acoustic perturbations alone. This connection between combustor acoustics and mixing could have a significant effect on NO formation rates.

The interaction of acoustics and fluid vortices was studied further by Kailasanath and coworkers in 1989 [24]. Their analytical model used a variable-geometry dump combustor, where the lengths of the inlet and the combustor regions could be independently changed. The length of the two regions affects the natural acoustic modes, and the authors studied the effect of these natural modes on the vortex shedding from the step. They found that the basic vortex shedding frequency was controlled by the natural acoustic mode of the combustor region. However, the natural frequency of the inlet could affect the rate of merging of successive vortices in the combustor. The authors note the possible application to the design of premixing combustors, for these results indicate that mixing can be enhanced or hindered depending on the natural acoustic modes of the inlet and the combustor.

In 1992 Maughan et al. studied the effect of fuel-air mixing on NO_x emissions [25]. While they tried to discriminate between the uniformity of the initial fuel distribution (spatial effects) and the amount of time allowed for mixing (temporal and spatial effects), they admit that "No attempt is made here to distinguish between spatial and temporal unmixedness." Their results agree with those of Semerjian et al., reemphasizing the importance of homogeneously premixed reactants for minimized NO_x emissions in lean flames. Uniform distribution of fuel, although greatly desired, cannot be achieved in practice and subsequent mixing is required. Increased turbulent mixing

intensity and a greater distance between the site of fuel injection and the flameholder are the most important contributors to improved NO_x emissions.

Very recent work on the effect of fuel-air unmixedness on NO_x emissions has been presented by Fric [26]. He used laser-induced fluorescence to measure the spatial and temporal variations in equivalence ratio of a fuel jet mixing with a coannular flow of air. He compared the effect of temporal variations on the yield of NO_x for two cases at the same mean equivalence ratio. He concludes:

> The primary conclusion from this work is that it is not sufficient to consider only spatial nonuniformities in fuel mixture when quantifying the effectiveness of a premixer to minimize NO_x emissions. Temporal unmixedness, or concentration fluctuations, contribute significantly to higher NO_x emissions. The results show that seemingly small levels of temporal unmixedness, c'/c on the order of 10% or $U \approx 0.0004$, can double NO_x emissions relative to a perfectly premixed flame, given spatially uniform mean concentration profiles in both cases.

For other experimental cases, Fric is unable to separate the effects of temporal and spatial unmixedness on the NO_x emissions. Although he states that his burner was nonadiabatic, he did not measure flame temperatures.

Although Fric's work and the subject of this dissertation appear to be quite similar in some respects, there are several significant differences. Both studies use methane-air burners and measure the temporal fluctuations in equivalence ratio, and try to relate the

NO_x emissions to the degree of unmixedness in the flow. The significant differences are listed below:

FLAMEHOLDERS: In Fric's experiment, the flame was anchored in the burner by a combination rearward-facing step and a cross-hair-shaped bluff body. He measured the temporal and spatial fluctuations of the flow field entering the burner without the bluff body or a quartz chimney in place. These two items were subsequently replaced in the burner for the combusting tests, and he assumed that neither would significantly change the flow field and mixing processes. However, a bluff body flame stabilizer works on the principle of disturbing the flow and the creation of recirculation zones.

In the current experiment, the flameholder is a stainless-steel screen which acts as a flame arrestor, and with a laminar flow the disturbances should be negligible. Spatial equivalence ratio distributions are measured with the flameholder in place, so that any flameholder-induced mixing is accounted for. Optical measurements of the temporal equivalence ratio fluctuations are obtained just upstream of the flameholder, and it must be assumed that the flameholder would have negligible mixing effects in the axial direction. Indeed, there is no reason to expect that it would.

EQUIVALENCE RATIO: Fric worked with a fixed equivalence ratio of 0.5. He was only able to separate temporal and spatial effects of equivalence ratio on NO_x

emissions for two cases. It cannot be inferred whether the effects would be more or less significant at other equivalence ratios.

The current experiment covers a range of equivalence ratios. This not only helps separate the temporal and spatial effects, but the consequences are found for flames in the range between the lean flammability limit and stoichiometric.

TEMPERATURE MEASUREMENTS: Fric has no measurements of temperature, and supposed effects of temperature on NO_x must be inferred from the equivalence ratio measurements. In the lean-to-stoichiometric equivalence ratio range, NO_x formation is directly temperature related, and the equivalence ratio is important primarily for its effect on the flame temperature. However, the assumed relationship between equivalence ratio and temperature can be changed by burner nonadiabaticity and wall reactions, both of which can change as the flow patterns and flame structure in the burner are varied.

The experiment reported in this dissertation measures the temperatures with thermocouples, permitting time-resolved flame temperature estimates and correlations between equivalence ratio and temperature, accounting for heat transfer and wall quenching effects.

GAS SUBSTITUTION: Fric's optical techniques do not measure the methane-air mixing processes directly. The methane is replaced with NO_2-doped nitrogen, and the mixing of the NO_2 with the air is measured in cold flow. He assumes that the density and diffusion differences between methane and NO_2 will lead to small errors. However, the molecular diffusivity of methane is seventy percent greater than the molecular diffusivity of NO_2, and the density of methane is one-third that of NO_2.

The optical technique for the current experiment measures the methane concentration directly, in hot flow and with the flameholder in place. However, the spatial air-fuel distribution is measured by probe sampling, and must still be done in cold flow.

BUOYANCY EFFECTS: Fric's burner is oriented horizontally and he observes that buoyancy effects appear in the measured NO_x profiles. This introduces asymmetry into his burner, including changing the heat transfer properties along the top and the bottom surfaces of the combustor.

Although the burner for the current experiment is also subject to spatial asymmetry for some of the flames (and this is intentional in some cases), its vertical orientation prevents buoyancy effects from changing the spatial equivalence ratio distributions.

MODELING: Although Fric's technique provides statistical measures of the flow field such as the mean and variance of the equivalence ratio fluctuations, the turbulent flow field makes it difficult to model the combustion processes in the flame.

With laminar flow, more direct control over the flow field can be obtained. Regular, repeating waveforms for the equivalence ratio and temperature have been obtained, and these have been used to model the flame processes.

HEAT TRANSFER: Fric assumes that the heat transfer is similar between all of his cases, implying that the axial temperature profiles would be similar. However, he notes that the length of his flame changes as the unmixedness is changed, and this indicates probable changes in the axial (and perhaps radial) temperature profiles.

Although detailed axial temperature profiles were obtained only for certain flames in the current experiment, the temperature of the flame zone was measured for all flames. In this way, changes in combustor performance are accounted for as the flame structure changes. Note also that since the flame is flat, its length does not change as the equivalence ratio is varied. The equivalence ratio was not a consistent indicator of the flame temperature in the present experiment, and direct temperature measurements were essential.

In summary, the literature shows that confusion remains about the effects of fluctuating temperatures on rates of NO_x production in premixed flames. While analytical work shows that NO_x emissions should increase due to fluctuating temperatures, several experiments have failed to clearly show this effect. Further confusion is caused by various authors proposing different sources for the temperature fluctuations. One source could be acoustic perturbations caused the quarter-wave (or some other) mode of a combustor, another source could be the random fluctuations that occur in turbulent reacting flows, and a third source could be vortices shed from a flameholder. It is also possible for these sources to be interrelated or to occur simultaneously and independently. The community is increasingly aware that combustor acoustics can influence fuel-air mixing. In an actual gas turbine combustor, all of these sources could be present.

A serious deficiency of the research to date has been the preoccupation with spatial equivalence ratio measurements, and the inadequate development of practical techniques for temporal measurements of equivalence ratio and temperature. Progress in the development of low-NO_x combustors could depend on this change in focus and a realization that spatial nonuniformities perhaps are no more than half of the problem. The next section describes an experimental program designed to produce controlled fluctuations of equivalence ratio in a burner and to measure the NO_x emissions. Time-resolved measurements of both temperature and equivalence ratio are featured.

1.3 SUMMARY OF THE EXPERIMENT

Many factors shaped the design of the experimental apparatus, the choice of the instruments used, and the types of measurements that were made. The experiment "evolved" as trial-and-error revealed features that would work, and others that would not, and new solutions were found. The following paragraphs explain the original concept of the experiment and its goals.

The focus of the experiment is the separation of the effects of temporal and spatial variations in equivalence ratio on the NO_x emissions of premixed methane-air flames. By measuring equivalence ratio we are in effect measuring the mixedness of the fuel and the air. In the dissertation, *temporal effects* refers to a time-varying change in the equivalence ratio at a fixed point in the flame. *Spatial effects* refers to the nonuniformity of the equivalence ratio across different regions of the flame surface, when the equivalence ratio is measured in a time-mean sense. Since these properties are easier to quantify in a flat laminar flame than in a turbulent flame, a laminar flame was used in this study. Indeed, many of the expected advantages for this experiment arise from the ability to quantify and separate temporal and spatial effects unambiguously in a laminar flat flame. The key is reducing the flame to a two-dimensional surface, so that strong axial variations in temperature and mixing are eliminated. As the literature review

shows, separation of temporal and spatial effects in a turbulent three-dimensional flame is nearly impossible without very sophisticated diagnostic techniques.

A study of temporal effects demands instrumentation capable of time-resolved measurements, so that these effects can be quantified. The author was aware of an optical technique for measuring methane concentrations which would have an adequately fast time response. Thus, temporal equivalence ratio fluctuations could be measured. Spatial nonuniformities in equivalence ratio could be measured by probe sampling, since by definition temporal response is not a factor. Although time-resolved measurement of the NO_x production would have been beneficial, the techniques for such measurements were not readily available [27,28].

The optical technique works on the principle that infrared absorption is proportional to the concentration and path length of methane in another (nonabsorbing) gas. For the range of concentrations of practical interest (5 to 15 percent), the path length had to be limited to about 20 mm to avoid nonlinear absorption. This fixed the diameter of the burner and other geometrical features. For instance, there had to be optical access immediately before the flame zone; thus, a vertical quartz tube and a "floating" flameholder were essential components of the burner.

A set of baseline measurements was made to characterize this burner under well controlled conditions. Tests were made of the infrared absorption and the flammability limits in the burner with homogeneously premixed flows of methane and air. The known mixtures were used to calibrate the optical system.

Most of the effort in this experiment involved the design of a burner capable of producing well-controlled temporal equivalence ratio fluctuations with a minimum of spatial nonuniformities (preferably none) across the flame. The ideal fuel injector would introduce methane into the axial flow in uniform horizontal disks, so that there would be no spatial nonuniformities when these "pulses" reached the flame. Injected upstream of the flameholder, these thin disks would diffuse axially into the neighboring gases so that the optical system would detect a sinusoidally-varying equivalence ratio, always within the lean and rich combustion limits of the burner. The mean, amplitude, and frequency of these fluctuations would be controlled by modifying the methane injection parameters.

Naturally, these goals were difficult to achieve in practice. Several different mechanical injection systems were designed and tested, and not even the best of these could completely eliminate the spatial nonuniformities that arose from nonuniform radial and circumferential methane injection. Nevertheless, the spatial variations were minimized, measured, and characterized. Homogeneously premixed, temporally steady flames were measured as a baseline. Steady flames with only spatial nonuniformity of

equivalence ratio were measured, in the expectation that the effect of spatial nonuniformities on NO_x could be modeled. Finally, temporally unsteady ("pulsing") flames were measured, with the understanding that some spatial nonuniformities were unavoidable. The effect of the temporal fluctuations on NO_x would be inferred from the pulsing flame data. Thermocouple measurements were added to the list of experimental techniques; it was uncertain whether equivalence ratio measurements alone would give sufficient insight into the NO_x formation processes.

To summarize the experiment, three different types of premixed laminar methane-air flames were studied: steady homogeneous flames, pulsing flames, and steady flames with spatially nonuniform equivalence ratio distributions. For each flame, three properties were measured: temperature, equivalence ratio, and NO_x production. The NO_x yield was always measured with a sampling probe located well downstream of the flame zone. The equivalence ratio measurements depended on the type of flame. For the steady flames, the total methane and air flow rates were read from calibrated rotameters. For the pulsing flames, the optical system recorded the time-varying infrared absorption of methane, which was later converted into equivalence ratio. Although the spatially nonuniform flames had a steady flow, some of this flow bypassed the methane rotameter. Cold-flow measurements of the equivalence ratio distribution were obtained just downstream of the flameholder with a sampling probe and a hydrocarbon analyzer. For all three types of flames, the temperature of the flame zone itself was measured with

a thermocouple. Time-resolved thermocouple measurements could not be obtained in the flame zone itself. However, temporal temperature measurements were obtained as close to the flame as possible and the fluctuating flame temperature was estimated by extrapolation.

The end result of all of these measurements is a comparison between the three types of flames, showing the effect of the temperature variations on the NO_x yield. A model is presented which predicts the increase in NO_x for any given temperature-time history for this burner. The following chapters describe in detail the experimental apparatus and procedures, the algorithms for manipulating the data, and the experimental results.

CHAPTER 2

EXPERIMENTAL APPARATUS

The experiment is described in this chapter. The initial overview explains how the instruments were used and how the measurement systems relate to each other. It describes the types of flame that were studied, the types of measurement that were made, and the experimental procedures. The rest of the chapter covers the experimental apparatus and the analytical work supporting the optical and thermocouple measurements. Procedures and techniques were modified as the experiment evolved, and these modifications are described throughout the chapter.

2.1 OVERVIEW

Figure 2 shows a schematic of the experiment. Air and methane (CH_4) flow from gas cylinders to calibrated rotameters. The air and methane are thoroughly mixed in the premixing chambers and flow to a plenum at the bottom of the burner assembly. The premixed gases flow vertically past a fuel injector, through flow straighteners, and into a 20-mm diameter (I.D.) quartz tube. The flameholder is a horizontal disk of stainless

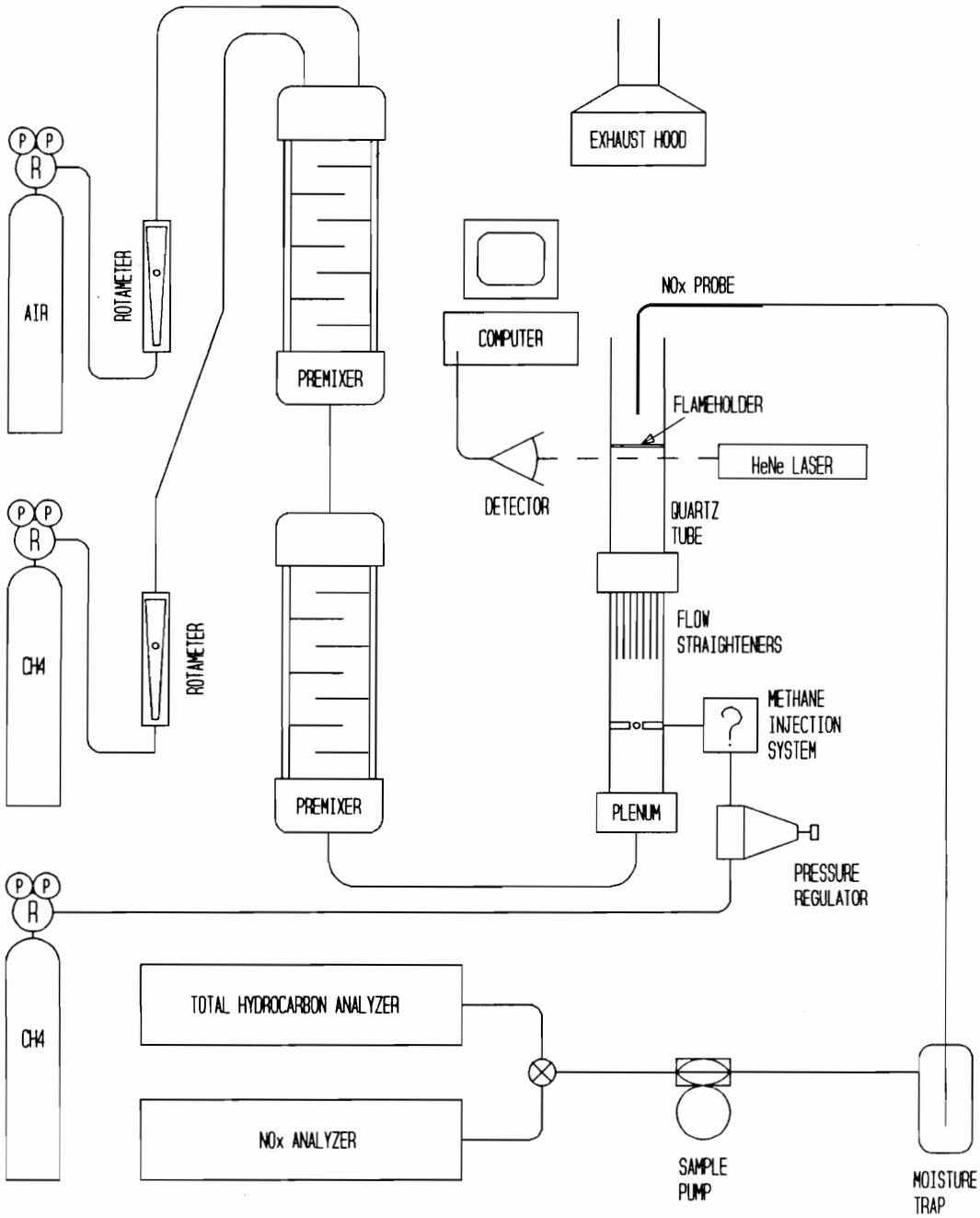

Figure 2 Schematic of Experimental Apparatus

steel screen supported from below by three thin wires. The flame is lit at the mouth of the quartz tube, propagates upstream, and is arrested at the screen. A 3-mm diameter (O.D.) quartz sampling probe is used for both NO_x and equivalence ratio measurements. For the NO_x measurements, the probe tip rests about 8 cm above the flameholder and the gases are sampled with a chemiluminescent analyzer. For scans of equivalence ratio distribution, the probe tip rests about 1 mm above the flameholder and the gases are sampled with a total hydrocarbon analyzer. The burner remains fixed and the probe is positioned with x-y translation stages. An optical system measures the instantaneous concentration of methane in the quartz tube. The beam of an infrared HeNe laser passes about 1 mm below the flameholder, so that it monitors the reactant gas composition just prior to combustion. An infrared detector measures the transmitted intensity of the laser beam. For the unsteady flames, pure methane is injected into the flow of premixed methane and air. The amount of fuel addition is controlled to achieve different mean values, amplitudes, and frequencies of equivalence ratio variations in the pulsing flames. Three different methods of methane injection were tested, and the "methane injection system" shown in Figure 2 is a general representation for three different types of pulse fuel injector.

2.2 TYPES OF FLAMES STUDIED

Three different types of laminar premixed methane-air flames were studied. All of these flames burned for at least 30 min prior to a test to allow the burner temperature to stabilize. The first type of flame studied was homogeneously premixed methane-air flames. For these flames, the methane injector was not used. These flames were studied as a baseline; NO_x emissions were measured as a function of the flame temperature and the equivalence ratio. The flame temperature was measured with a thermocouple and the NO_x emissions were measured by probe sampling in hot flow. Equivalence ratios were calculated from the rotameter readings. The dual premixing chambers assured a homogeneously premixed flow of reactants.

The second type of flame studied was temporally steady but spatially nonuniform. These flames were studied to quantify the effect of spatial equivalence ratio nonuniformity on NO_x emissions. The injector was held slightly open so that a small but continuous flow of pure methane was added to the premixed gases. Since the injection flow was continuous, there were no temporal fluctuations in the equivalence ratio. Spatial variations in the equivalence ratio arise from nonuniform radial and circumferential distribution of the injected methane. The distribution of equivalence ratio across the flameholder was measured in cold flow using probe sampling and a total

hydrocarbon analyzer. The flame temperature was measured with a thermocouple and the NO_x emissions were measured by probe sampling in hot flow.

The third type of flame studied had both temporal fluctuations and spatial nonuniformities of equivalence ratio. The spatial variations were unintended, and three different methane injectors were developed and tested in an attempt to improve the uniformity of methane injection. In each design, pure methane was pulsed into a premixed flow of methane and air. The gases are imperfectly premixed by the time they reach the flameholder: some spatial variations occur across the plane of the flameholder due to inadequate radial and circumferential diffusion, and strong temporal fluctuations occur due to the pulsed injection and incomplete axial diffusion in the flow. The temporal fluctuations in equivalence ratio were measured optically just before the flameholder in hot flow. Mean and fluctuating temperatures were measured along the axis of the burner with thermocouples, and the NO_x emissions were probe sampled well downstream.

The following sections describe the hardware for equivalence ratio, temperature, and NO_x emission measurements. The data acquisition system and the development and the design of the three methane injection systems are also described.

2.3 ROTAMETER CALIBRATIONS

Rotameters determined the composition of all of the well-premixed flows through the burner. Thus, they were used for all of the steady flames, for the calibration of the optical system, and even as the reference mixture for setting the span of the total hydrocarbon analyzer.

The air rotameter was calibrated using an American Meter Company model 802 dry gas flow meter and a stopwatch. Volume flow rates (gas displaced divided by flow time) were correlated with the float position. Figure 3 shows the calibration for the air rotameter. There is a nonzero intercept for the steel float; it was not displaced below a minimum flow of 0.5 ℓ/min at STP. The methane rotameter was calibrated with both the dry gas flow meter and a soap bubble meter. Figure 4 shows the calibration for the methane rotameter. The two calibration methods agree well, but the data for the soap bubble meter were used since the calibration method is more accurate. The repeatability of these measurements was exceptional. The soap bubble meter was impractically undersized for calibrating the air rotameter. The methane flow meter was calibrated using methane gas.

For almost all experiments, the air rotameter floats remained fixed at 100 (glass float) and 49 (steel float), for an air flow rate of 3.95 ℓ/min. The equivalence ratio of

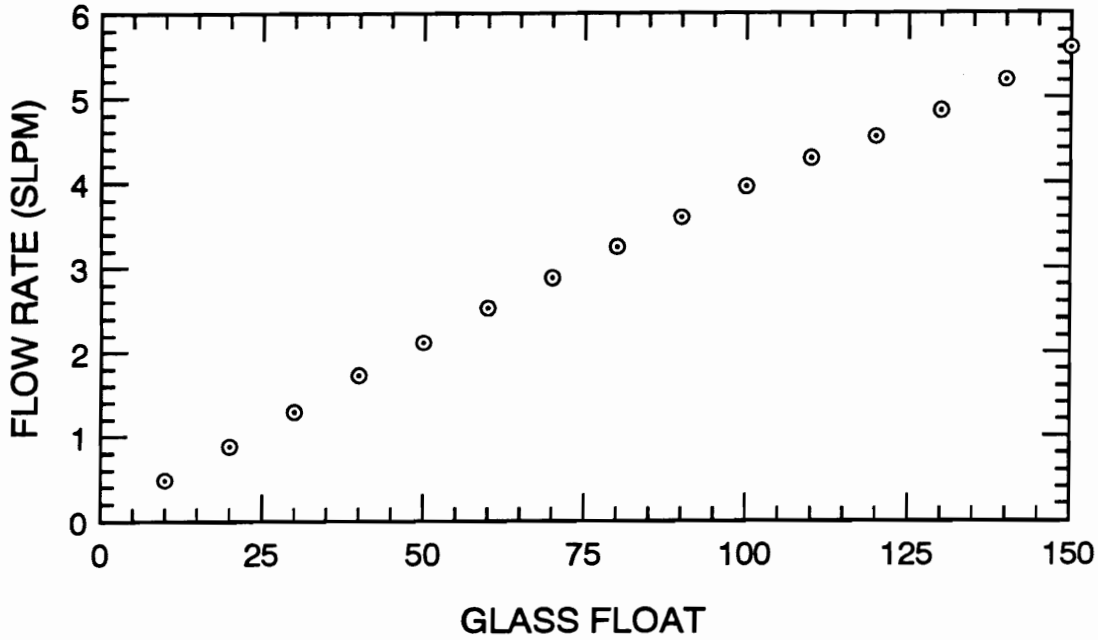

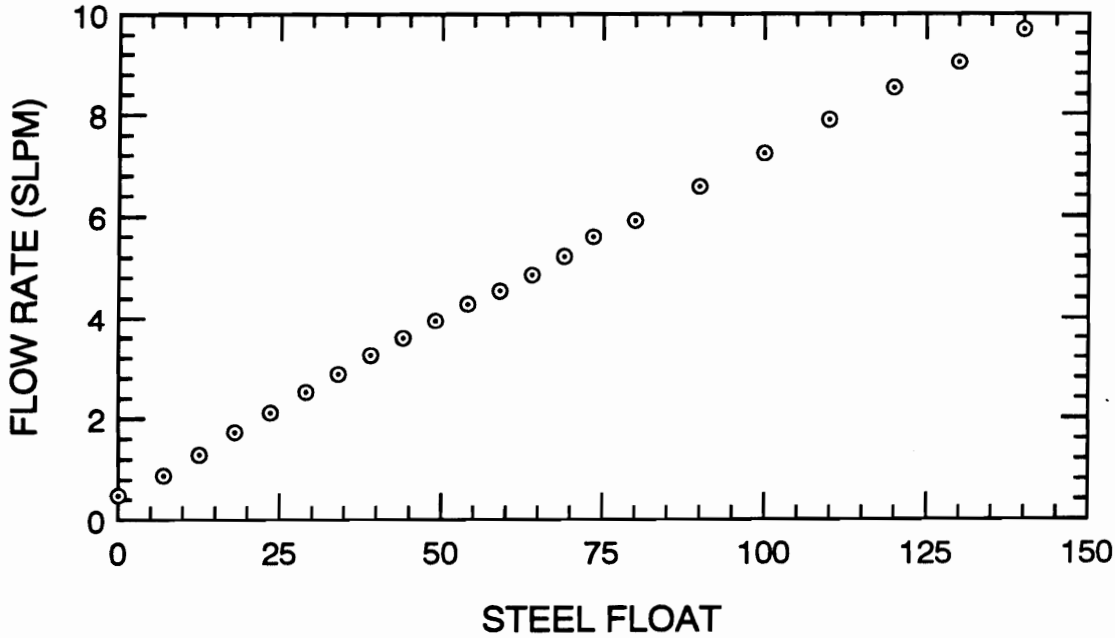

(AIR @ 20 psig)

Figure 3 Calibration for Air Rotameter (Matheson Size 6 with Type HA5 Needle Valve, Housing Model FM-1050B-HA)

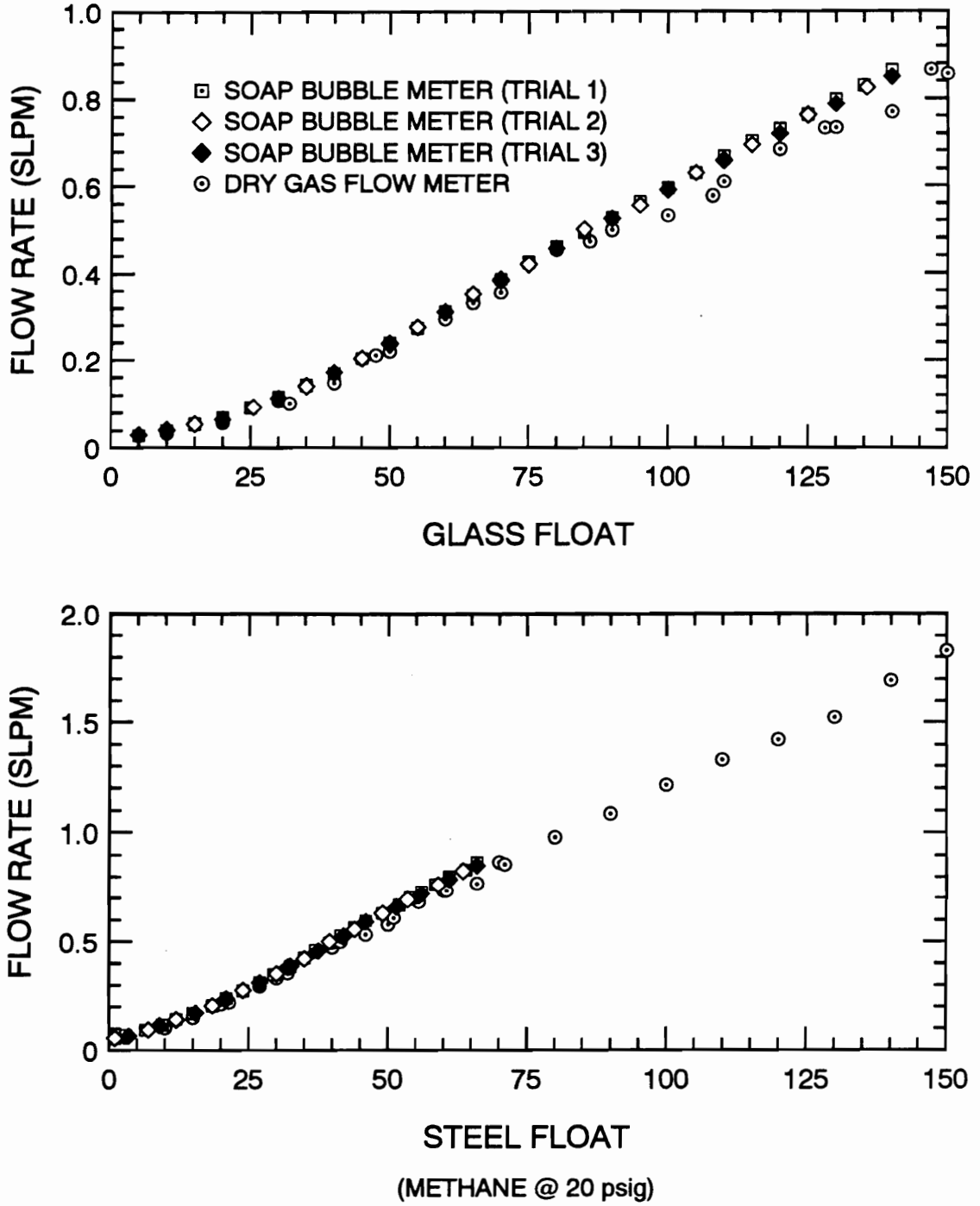

Figure 4 Calibration for Methane Rotameter (Matheson Size 602 with Type HA3 Needle Valve, Housing Model FM-1050B-HA)

the premixed gases varied with the methane flow rate. The methane rotameter floats were usually set to the same positions as in the soap bubble meter calibration. For instance, the glass float was positioned in increments of 5. The maximum methane flow was 0.6 ℓ/min, so the range of the soap bubble meter calibration was never exceeded. Linear interpolation between the calibration data was used as necessary.

2.4 GAS CYLINDERS

The experiment uses a variety of gases for different purposes. All of the gases were supplied in cylinders and the supply pressures were controlled by Matheson two-stage regulators. The combustion air was Airco "dry" grade, made from compressed air with the moisture and oil residues filtered out. Although it is more expensive than standard breathing air, the oxygen concentration remains constant. Standard breathing air is reconstituted from a mixture of liquified oxygen and liquified nitrogen, and its oxygen concentration is allowed to vary between 19 and 23 percent. Dry air was specified for the combustion air because variations in the oxygen content of breathing air cylinders were detected in previous experiments [29]. The total hydrocarbon analyzer uses air to support its internal hydrogen-air pilot flame, and the chemiluminescent NO_x analyzer uses air for its ozone generator. Breathing air cylinders were used for the gas analyzers. Since each of these instruments was recalibrated daily, changes in oxygen

content between breathing air cylinders could be readily accounted for. Air pressures were controlled with Matheson model 8-590 regulators.

The fuel for the experiment was Airco grade 2 methane, specified pure to 99 percent. This was more expensive than the standard grade, which is only 96 percent methane. It is important, however, to minimize the effects of other infrared-absorbing gases while making spectroscopic measurements. "Natural gas" can come from a variety of sources, and the remaining four percent of its content can have unknown amounts of moisture and higher molecular weight hydrocarbons, all of which are active in the infrared. Two separate methane cylinders were used, so that the regulator pressure of the methane for the premixed flow could be different than the back pressure of the methane supplied to the methane injector. Matheson model 8-350 regulators were used.

The "zero" of the analyzers was set while sampling a flow of prepurified nitrogen gas (Matheson regulator model 8-580). The span of the NO_x analyzer was set using a custom Matheson gas mixture of nitric oxide (NO) in nitrogen (Matheson regulator model 3517-660). This cylinder was analyzed by Matheson using gas chromatography and its NO concentration was specified as 52 ± 1 ppm NO. The fuel for the total hydrocarbon analyzer was a 40 percent hydrogen/60 percent nitrogen mixture (Matheson regulator model 3104C-350). For sampling high hydrocarbon concentrations, the hydrogen/nitrogen mixture gives better linearity than pure hydrogen fuel.

2.5 OPTICAL MEASUREMENTS

An optical system measured the temporal equivalence ratio fluctuations of the unsteady flames. This method is nonintrusive and has a fast time response. The method detects the infrared absorption of methane—the higher the concentration of methane in a mixture, the greater the absorption of an infrared beam passing through the mixture. The components of the system are described following a review of extinction measurements.

2.5.1 Extinction Theory

The optical system applies the general form of Beer's law,

$$dI = -I\,\alpha_\lambda\,C\,s \quad . \tag{4}$$

Equation (4) can be integrated over pathlength L to obtain

$$\frac{I}{I_o} = \exp(-\alpha_\lambda\,C\,L) \quad . \tag{5}$$

Equation (5) describes the attenuation of an incident light intensity I_o as it passes through an absorbing medium of length L. In this application, the medium is premixed methane

and air, where the methane is the only species of these two that absorbs infrared radiation. The path length L (mm) is fixed in the experiment by the diameter of the burner. The methane concentration C (volume fraction) is the property to be measured. The absorption coefficient α_λ (mm^{-1}) is a constant for this application; it corresponds to the absorption of λ = 3391 nm wavelength infrared radiation by methane molecules. This wavelength comes from the infrared line of a HeNe laser. Since this infrared source is monochromatic, the λ subscript is dropped with the understanding that all measurements are made at the laser's wavelength. The baseline intensity I_o (W) is a reference intensity of the radiation measured at a detector. The I_o reference measurement is made in the absence of any extinction effects (i.e. no methane in the burner). The transmitted intensity I (W) is the experimentally measured variable—it is the intensity of the radiation reaching the detector when absorption is present. This transmitted intensity is inversely proportional to the concentration of the methane in the burner flow. The ratio I/I_o is commonly referred to as the *extinction*, and the product αCL is called the *optical density*. The system is calibrated experimentally with mixtures of known methane concentration. An empirical relationship between the measured extinction and the optical density is used to calculate unknown methane concentrations.

Due to the fast response time of the optical system, rapid equivalence ratio fluctuations can be measured in unsteady flames. Note that as a line-of-sight type of measurement, the instantaneous *mean* concentration of the methane across the entire path

length determines the transmitted light intensity. In principle, greater spatial resolution could be gained by using optical tomography, but this technique was deemed beyond the scope of the experiment. The high curvature of the burner's quartz chimney would have led to strong beamsteering effects, and more translation stages would have been required. The additional complexity and expense did not seem to be warranted. In addition, optical tomography techniques are not ordinarily time-resolved measurements and would not be suitable for unsteady flames.

2.5.2 Optical Components

Figure 5 shows the optical system. A Particle Measuring Systems model PMS-0100-339 (S/N 3326-1891-132/1) helium-neon laser emits a 3391 nm wavelength infrared beam. The strength of this beam is 1.8 mW, with no visible radiation. A Stanford Research Systems model SR540 (S/N 600) chopper modulates the beam at a frequency of 1000 Hz. The beam passes through the quartz tube of the burner and is focused by a lens onto a lead selenide infrared detector (Oriel model 71190, S/N 86766, with model 71200 housing). The magnesium fluoride lens (Oriel model 43175) has a focal length of 200 mm and a diameter of 25 mm. The infrared detector is shielded by a laser-line filter (Oriel model 58200) to eliminate the light given off by the flame and by ambient lighting. This filter has a center wavelength of 3400 $\pm$ 30 nm and a half bandwidth of 120 $\pm$ 30 nm. The detector has a rise time of 2 μs and a square active area of 1 mm

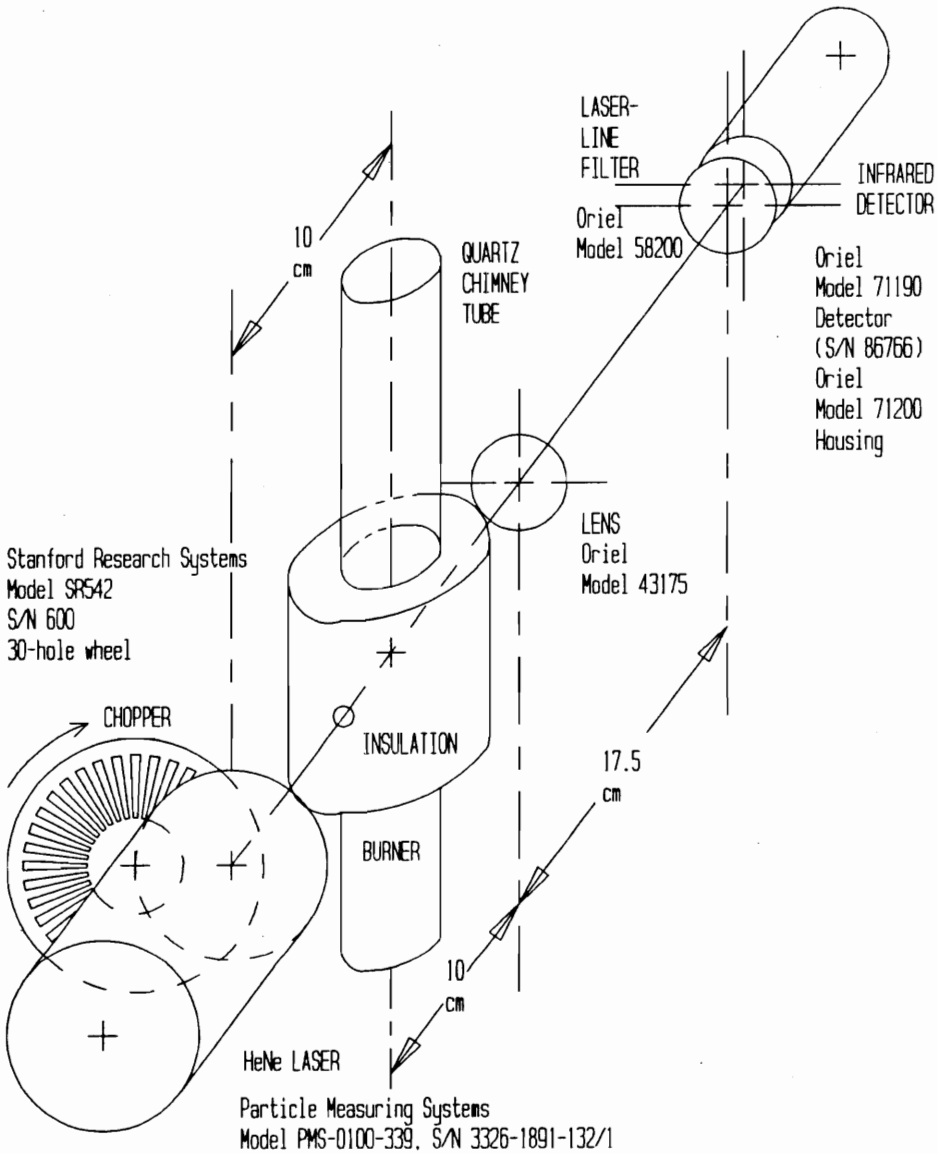

Figure 5 Optical System for Nonintrusive Equivalence Ratio Measurements

× 1 mm. This detector only responds to a transient input, hence the chopper is necessary. The detector output is sent to a Stanford Research Systems model SR510 lock-in amplifier (S/N 1745). The lock-in amplifier is tied to the chopper frequency and is operated with a time constant of 10 ms. Due to the use of both the laser-line filter and the lock-in amplifier, the effects of infrared light emission from the flame are considered to be negligible. The lock-in amplifier's output voltage is normally 0 to 10 V; this is stepped down to 0 to 5 V to be compatible with the data acquisition board.

Although any infrared light source such as an incandescent filament could be used for infrared absorption measurements, the infrared HeNe laser was certainly a convenient choice. Its emission at 3391 nm almost perfectly matches a strong absorption line for methane, making this source highly specific for just the desired molecule. Additionally, at only $1800, it is relatively inexpensive. However, this laser has two drawbacks. Because the laser is so inexpensive and emits only 1.8 mW of power, it does not have sophisticated feedback-type power controls. This lack of output power stability can result in significant signal drift during the course of an experiment. The second drawback is that the 3391 nm absorptivity of methane is almost too strong—for the range of methane concentrations of practical interest (5 to 15 percent), the path length has to be limited to 20 mm to transmit sufficient radiation. Excessive absorption causes problems in signal detection and can lead to nonlinearities in the system calibration. This limitation requires a small burner diameter, and surface reactions and nonadiabaticity of the burner have

potentially more influence on the flame. The burner diameter could be enlarged if the wavelength of the light source could be shifted to a weaker methane absorption line.

This burner and optics design were based on the author's knowledge about another experiment. K. B. Chung at Cornell University had measured extinction I/I_o in the range of 0.2 to 0.3 for methane concentrations of one to five percent across an 80 mm path length with the infrared line of a HeNe laser [30]. These data were used to estimate the absorption coefficient for methane assuming that an extinction of 0.25 would correspond to a methane concentration of three percent. The assumed absorption coefficient (0.58 mm^{-1}, with methane concentration expressed as volume percent) turned out to be reasonably close to the absorption coefficient measured in the current experiment (0.515 mm^{-1}). In the current experiment methane concentrations were expected to vary between the lean limit and stoichiometric for premixed methane/air flames, approximately five percent to ten percent methane by volume. For an assumed methane concentration of ten percent, a path length (i.e. burner chimney diameter) of 20 mm was expected to give an extinction of 0.3, which would avoid the effects of nonlinear absorption and deviation from Beer's law.

2.5.3 Calibration of The Optical System

The relationship between the extinction I/I_o and the equivalence ratio was determined experimentally. The baseline infrared light intensity I_o is measured with pure air flowing through the quartz burner tube. Since dry air has no infrared absorption, the measured intensity represents the output power of the laser, the losses through the optics, and the gain of the detector and lock-in amplifier. When methane is introduced into the flow, it attenuates the transmission of the laser beam and the measured intensity I decreases. Mixtures of known equivalence ratio flowed through the quartz burner tube and the extinction I/I_o was measured. A chemical balance for methane-air combustion shows

$$\phi\ CH_4 + 2\,(O_2 + 3.76\ N_2) \Rightarrow Products \quad .$$

This gives the methane concentration as a function of the equivalence ratio,

$$C_{CH_4} = \frac{\phi}{9.52 + \phi} \quad . \tag{7}$$

When equation (7) is substituted into equation (5), Beer's law can be rearranged, yielding

$$\phi = \frac{\dfrac{-9.52}{\alpha L} \ln\left[\dfrac{I}{I_o}\right]}{1 + \dfrac{1}{\alpha L} \ln\left[\dfrac{I}{I_o}\right]} \quad . \tag{8}$$

For $\phi < 1.2$, the second term in the denominator, $(1/\alpha L)\ \ln(I/I_o)$, is less than 0.1. Therefore, equation (8) can be adequately represented by a least-squares linear fit of the form $\phi = A\ \ln(I/I_o) + B$, particularly since the coefficient B is « 1. The experimental correlation of this form is given in Chapter 3.

Once this calibration equation is established using steady, well premixed gas mixtures, it is assumed to hold for the unsteady flame mixtures as well. The instantaneous equivalence ratio is calculated from the time history of I/I_o. The effect of the 10 ms time constant ($\approx$ response time) of the lock-in amplifier on the signal is considered negligible at the low pulse frequencies used in the experiment (below 10 Hz).

Before each experiment, the background or reference intensity (I_o) was measured. Another background measurement was made at the end of the experiment, and the results were averaged. This reduced the error due to signal drift, which could be as much as ten percent during a test. The background measurement was made with dry air flowing through the burner.

2.6 GAS ANALYZERS AND SAMPLING

This section describes the gas sampling system, the analyzers used for NO_x and equivalence ratio measurements, and the procedure for spatial equivalence ratio distribution measurements.

2.6.1 Sampling System

Figure 6 shows the gas sampling system. This system sampled the NO_x emissions in the post-flame gases for all of the flames. It also sampled the cold flow distribution of equivalence ratio across the flameholder screen for the spatially nonuniform flames. The sample was aspirated through a 3-mm O.D. uncooled quartz probe. A 30-cm stainless steel tube held the quartz probe. The transfer lines were 6.4-mm O.D. teflon tubing. The moisture trap was a 250-ml Erlenmeyer flask suspended in an ice bath. This moisture trap was important for sampling NO_x but was unnecessary for measuring equivalence ratio. Since the amount of water removed from the sampled gases was unknown, all of the NO_x measurements in this work are presented on a dry basis. The water was removed from the trap between each series of experiments (usually several times a day). The trap seemed to be effective; some moisture condensed out in the lines upstream of the flask, but no moisture was observed in the teflon lines downstream of the trap. The sample pump was a Thomas Industries Model 107CAB18 single-stage

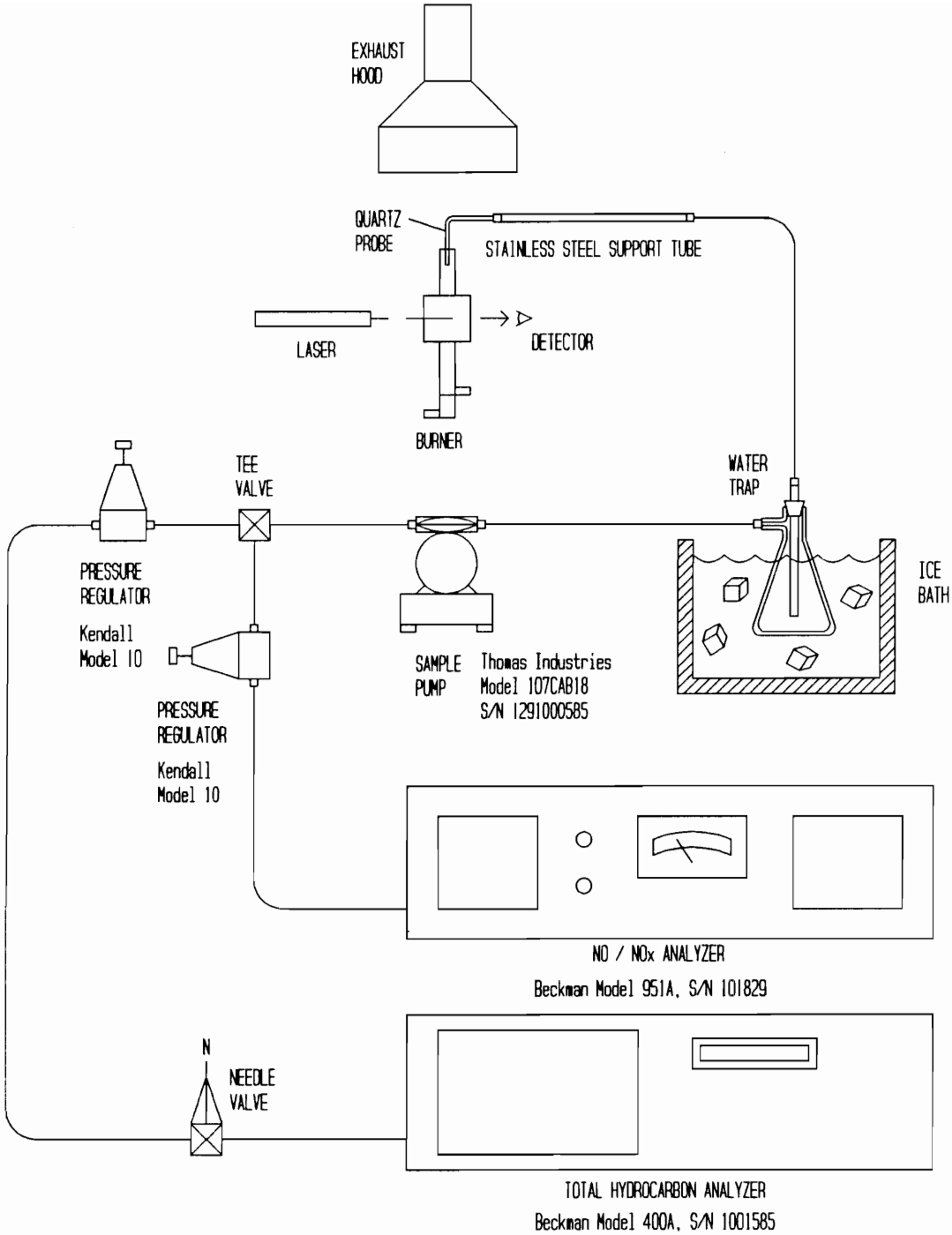

Figure 6 Gas Sampling System

diaphragm pump (S/N 1291000585), with a maximum output pressure of 35 psig. Since this pressure was too high for either of the gas analyzers, a single-stage Kendall model 10 pressure regulator (output range: 0-10 psig) was required in each line. A needle valve was required before the total hydrocarbon analyzer to restrict the sample flow rate further.

2.6.2 The NO_x Analyzer

NO and NO_x measurements were made using a Beckman model 951A chemiluminescent analyzer (S/N 101829). The ozone generator of the analyzer consumed breathing-grade air. The zero of the analyzer was set while sampling prepurified dry nitrogen gas. The zero calibration was stable and required checking only once a week. The span of the analyzer was set while sampling a calibration standard of 52 ppm nitric oxide (NO) in nitrogen. This calibration standard was analyzed by Matheson with a stated accuracy of $\pm$ 2 percent of the reading ($\pm$ 1 ppm). The analyzer span was set to 52 ppm for both the NO and NO_x modes during calibration. Although both NO and NO_x were measured, only NO_x is reported since NO to NO_2 conversion within the sampling system was not necessarily well controlled. NO measurements were usually within 10 percent of the NO_x emissions, although larger deviations were occasionally observed. The span calibration was not as stable as the zero calibration, so the span was recalibrated daily.

The tip of the probe was located about 8 cm above the flameholder screen for NO_x measurements. This placed the probe well within the quartz chimney yet sufficiently far downstream of the flame that NO_x levels had stabilized. The sample flow varied from as much as 2.2 ℓ/min to as little as 1.6 ℓ/min, depending on the temperature of the sampled gases. The high flow rate (roughly half of the total flow through the burner) assured a representative sample of the mean NO_x emissions. Changing the radial location of the sampling probe in the quartz tube did not affect the data, and vertical (streamwise) displacements of $\pm$ 1 cm did not change the readings by more than 1 ppm. The smoke plume from a cigarette held close to the quartz chimney visually indicated that the probe was not ingesting room air from outside of the burner.

2.6.3 The THC Analyzer

Methane concentrations for the spatially nonuniform flames were measured using a Rosemount Analytical model 400A total hydrocarbon (THC) analyzer (S/N 1001585). This instrument uses a flame ionization type of detector. The zero of this analyzer was set while sampling the burner air (industrial grade 2.0). The span was set while sampling a known and homogeneously premixed methane-air mixture. The mixture composition was determined by the flow through calibrated rotameters. While this makes the accuracy of the THC analyzer dependent on the rotameter calibrations, it ensures that the equivalence ratio measurements are consistent between the spatially nonuniform

flames and the steady flames. Both the zero and the span of the analyzer were reset daily. Calibration drift was 0.5 percent or less over the course of each experiment.

The analyzer required modifications to reduce its sensitivity and the sample flow rate. Although its fullscale sensitivity could be set at ten percent methane, the instrument would over-range at much lower concentrations. Additionally, the analyzer was designed for sample flow rates on the order of the total flow rate through the burner (0.3 to 3 ℓ/min). At flow rates this high spatially-resolved probe measurements would be impossible. Therefore, two of the analyzer's operating parameters were modified. The sample bypass pressure was set to its lowest recommended limit, 1.5 psig. A needle valve was required to restrict the flow further. The sample bypass flow remained steady at about 70 cc/min, or about two percent of the total flow through the burner. Thus, spatial resolution was possible with the probe measurements. The second modification involves the internal burner of the analyzer. This burner is fueled by a cylinder of breathing air and a cylinder of a fuel mixture (40 percent hydrogen / 60 percent nitrogen). The instruction manual specifies a minimum supply pressure of 25 psig from both cylinders, but the sensitivity of the instrument was too high at these settings. The fuel supply pressure was reduced to 10 psig and the air supply pressure was reduced to 15 psig. This change was recommended by a service engineer of the manufacturer [31]. This resulted in a stable and linear response with a sufficiently reduced sensitivity. Equivalence ratios up to 1.6 could be measured without over-ranging the analyzer.

2.6.4 Spatial Equivalence Ratio Measurements

The spatial equivalence ratio distribution was measured for all of the spatially nonuniform flames and for one of the pulsing flames. The sampling of spatial distribution occurred in cold flow, with the tip of the quartz probe positioned 1 mm above the flameholder. Figure 7 shows the sampling pattern for the equivalence ratio measurements. Isokinetic sampling was used, so the sample area should correspond to the 3-mm diameter of the probe (solid circles). Readings were taken at the axis of the quartz tube and at 4-mm and 8-mm radii, at 45-deg intervals. The mean and the standard deviation of the equivalence ratio were calculated from these seventeen samples. The dashed lines in Figure 7 define the presumed zones of coverage for each sample location. The nine interior zones (π mm^2) are each one-half the area of the eight outer zones (2π mm^2). Individual equivalence ratio measurements are weighted by the relative area of each zone. The equivalence ratio of each sample area is assumed to represent the mean equivalence ratio of each zone. This assumption is better for the nine interior zones than for the eight exterior zones, where the sample area is only about half of the zone area. The magnitude of the standard deviation is an estimate of the nonuniformity of the distribution. This is nondimensionalized as a mixedness parameter s, defined by

$$s = \frac{\sigma}{\bar{\phi}} \quad . \tag{9}$$

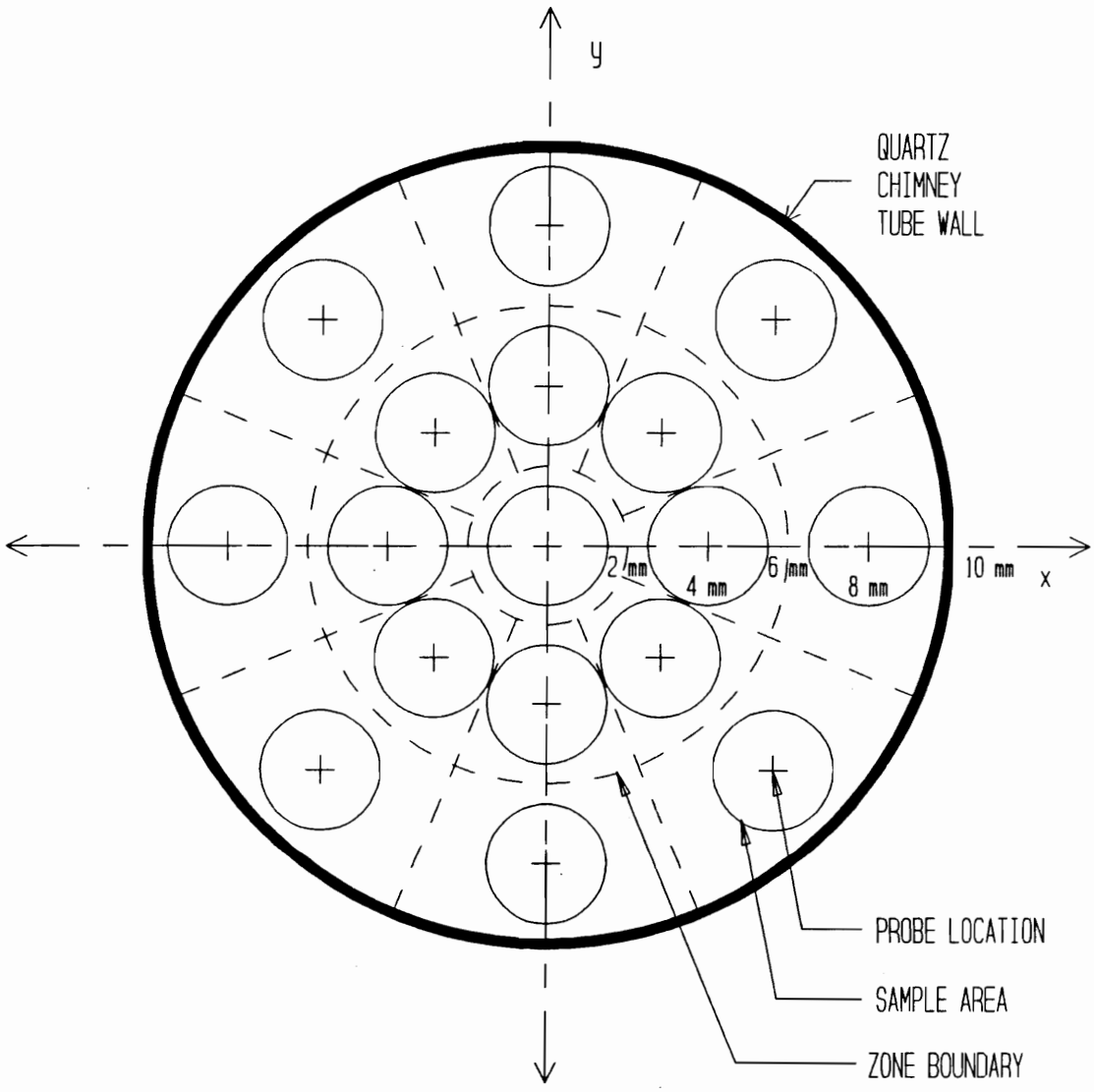

Figure 7 Sampling Pattern Over Flameholder Screen for Equivalence Ratio Distribution Measurements

2.7 THERMOCOUPLES

This section describes the procedures and apparatus used for temperature measurements in the burner. Although thermocouple measurements were not a part of the originally proposed experiment, they became essential to the completion of the research. The characterization, modeling, and correction of the thermocouple measurements were major efforts. These efforts are detailed in this section, and due to the importance of the thermocouple measurements, further analysis is presented in Chapter 4.

2.7.1 Temperature Measurement System

Thermocouples were used to measure the mean and fluctuating temperatures in the burner. Mean temperatures were measured using a type R (Pt/Pt-13%Rh) thermocouple probe with a 0.9-mm junction diameter. This thermocouple had a ceramic coating of yttrium oxide to minimize catalytic reactions on the junction. The fluctuating temperature probe ("fine" thermocouple hereafter) had a junction diameter of about 0.165 mm. This thermocouple was left uncoated to preserve its fast time response. An ice bath served as the reference junction. Since the full-scale output of type R thermocouples is only on the order of 20 mV, an amplifier boosted the signal prior to

digitization and storage on a computer. This amplifier (Omega model Omni II A, S/N 3014) had a gain of 52.

For the steady flames and the spatially nonuniform flames, only the mean flame temperature was measured. The large thermocouple probe was aligned with the axis of the burner and the probe was rapidly lowered to the flame zone. The presence of the ceramic probe changes the radiative heat transfer in the burner, leading to a significant temperature rise and increased NO_x emissions over time. For this reason, the probe was withdrawn to its rest position about 10 cm above the flameholder as soon as the temperature reading was completed.

Both thermocouple probes were used for the unsteady flames. The larger thermocouple measured mean temperatures along the axis of the burner at several positions above the flameholder and in the flame zone itself. Due to the fragility of the fine wire thermocouple, it could not be used in the flame zone. The fine thermocouple probe measured fluctuating temperatures starting at least 5.5 cm above the flame zone, and the probe was moved closer to the flame until a maximum temperature of 2000 K was reached. Experience had shown that the fine thermocouple would fail at higher temperatures.

2.7.2 Thermocouple Probes

Figure 8 shows the large thermocouple probe. The fine thermocouple probe is essentially identical except for the tip region (see inset). The large thermocouple measured the mean temperatures in the burner and the "fine" thermocouple measured the fluctuating temperatures. Both probes use type R (Pt/Pt-13%Rh) thermocouple wire and 150-mm long × 3-mm diameter alumina protective sheaths. The large thermocouple was made with 10-mil (0.25-mm) diameter wire throughout. The fine thermocouple junction was made with 1-mil (0.025-mm) wire, with 10-mil support wires. It was very difficult to weld the 1-mil thermocouple leads to the 10-mil support wires, so a mechanical connection was made. The ends of the 10-mil support leads were bent into loops, and the 1-mil thermocouple wires were threaded through the loops. All four wires (two of 1-mil diameter and two of 10-mil diameter) were threaded through the alumina sheath and attached to the connector jack. Care was taken to keep the pure platinum and the Pt-13%Rh wires paired properly to avoid spurious thermocouple junctions. The junction leads are maintained parallel to the flame surface for both probes to minimize conduction losses.

Each thermocouple used Pt/Pt-13%Rh wires from the junction back through the alumina tube to the connection terminals in a high-temperature plastic jack. Extension wire is used from the plug back to the amplifier. The plastic connectors have a

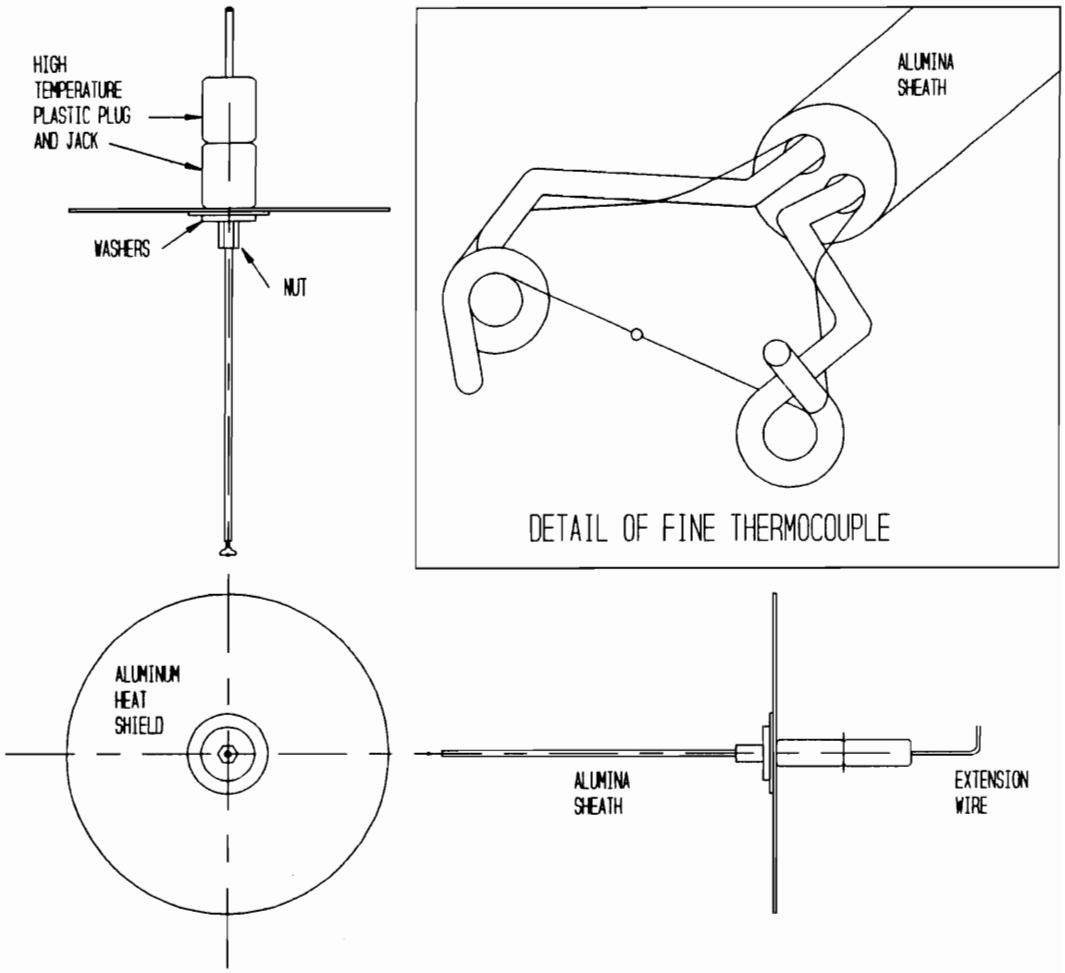

Figure 8 Construction of Thermocouple Probes

temperature limit of 260 °C and the extension wire has a temperature limit of 200 °C, so an aluminum shield plate was added to the thermocouple probes. This plate deflects the flow of hot combustion products away from the axis of the thermocouple probes and acts as a fin, protecting the connectors and extension wire.

2.7.3 Thermocouple Modeling

The thermocouples were characterized by a series of experiments and computer models. First, a cool-down test experimentally verified that the assumed junction diameter and emissivity were appropriate for the thermocouples. The response of the thermocouples to a step change in temperature was measured, and a computer model recreated the temperature history of the thermocouple. The assumed junction diameter and emissivity could be varied in the model, and the solution which most closely matched the experiment was used for the thermocouple properties. A second computer program calculated the conduction and radiation losses from the thermocouple. This program calculated the difference between the thermocouple temperature and the true gas temperature. This correction term was added to the experimental thermocouple readings. Finally, a third computer program predicted the frequency response of the fine thermocouple to sinusoidally-varying gas temperatures. The following sections present the basis for the computer models and the results of the three programs.

2.7.4 The Model

Figure 9 shows the model for the thermocouple. The junction is represented as a sphere of diameter D_1 with two cylindrical leads of diameter D_2. The leads are treated as cylindrical fins exposed to the gas temperature T_g. The junction temperature is T_c and the temperature of the end of the leads is T_{fin}. The thermocouple model can be broken down into two submodels. Submodel one represents the junction itself, and submodel two represents the leads at a large distance from the junction.

Submodel one allows three modes of heat transfer: radiation between the junction and the surroundings at T_w, convection between the junction and the gases, and conduction losses through the leads (fins). The governing equation for submodel one is

$$\rho c_p V \frac{dT_c}{dt} = h_1 A_s [T_g - T_c] + \epsilon \sigma A_s [T_w^4 - T_c^4] + \sqrt{h_2 P k A_c}\, [T_{fin} - T_c] \quad . \qquad \textbf{(10)}$$

In equation (10), the heat transfer coefficients h_1 and h_2 are estimated using Nusselt number correlations for flow over a sphere and a cylinder, respectively [32]. The leads are modeled as infinitely long fins.

Submodel two relates the lead temperature T_{fin} to the gas temperature T_g. In this submodel, convection and radiation heat transfer are balanced. Far from the junction,

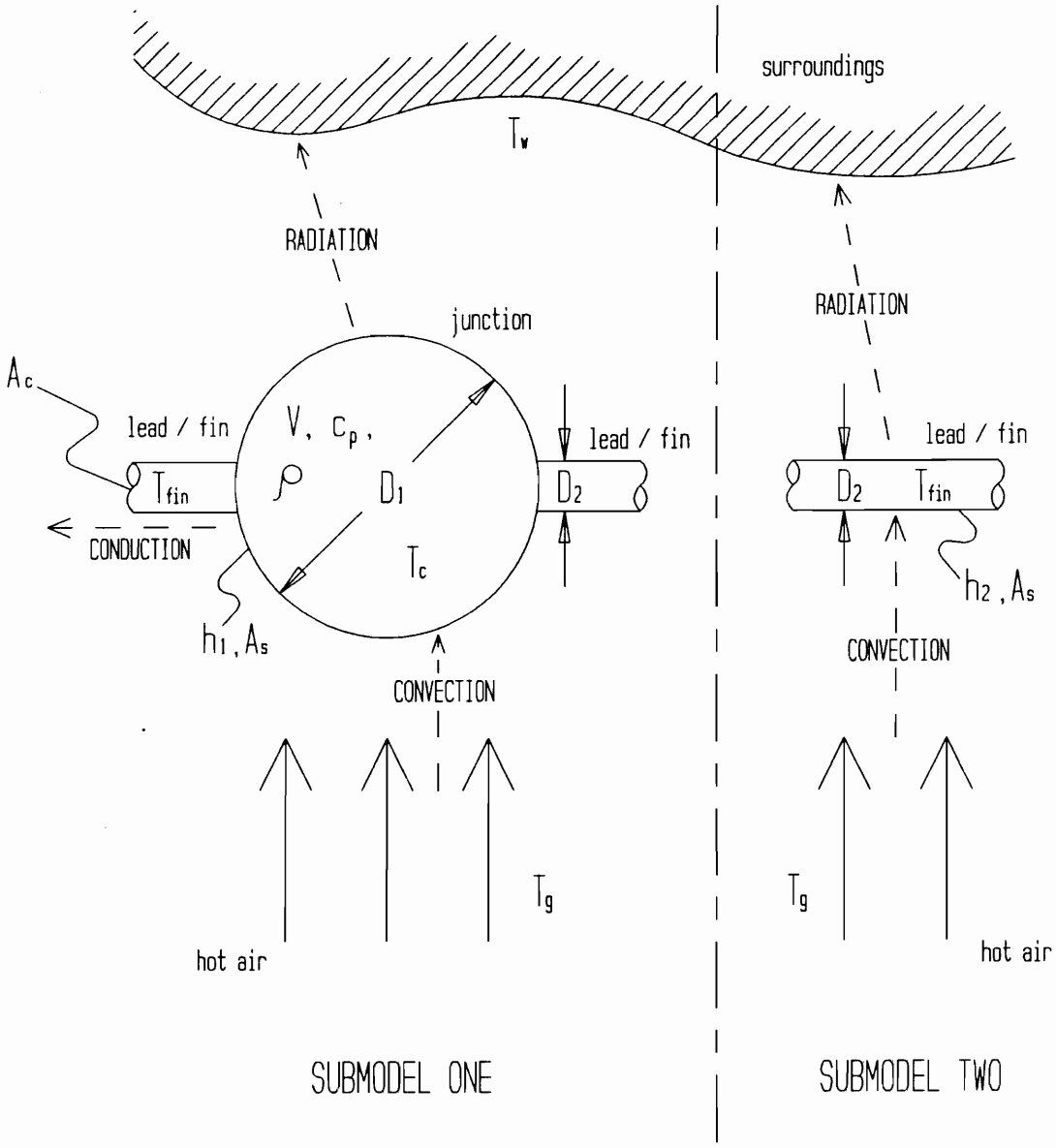

Figure 9 Thermocouple Model

the temperature gradients are assumed to be small so that the conduction in the leads is negligible with respect to radiation or convection. Radiation heat transfer is assumed to be with the surroundings at 300 K. The governing equation for submodel two is

$$\rho c_p V \frac{dT_{fin}}{dt} = 0 = h_2 A_s [T_g - T_{fin}] + \epsilon \sigma A_s [T_w^4 - T_{fin}^4] \quad . \tag{11}$$

For the model, the gas properties were estimated using tabulated properties for air at temperatures up to 2200 K [32]. The thermocouple itself was assumed to be pure platinum. Curve fits were made to tabulated data and the resulting equations are used to represent the material and gas properties over a wide range of temperatures.

2.7.5 Thermocouple Cool-Down Tests

The diameters of the thermocouple junctions were originally estimated by comparing the junction diameter to the known lead diameter under a microscope. However, this visual estimate was insufficiently accurate. The junction diameter has a large effect on the accuracy of the temperature correction term, and for the large thermocouple the junction diameter had to be correct to the nearest mil (0.025 mm). An effective junction diameter D_1 and emissivity ϵ were determined by experiment. The thermocouple junction was heated by a hand-held butane lighter, and the flame was suddenly pulled away. As the thermocouple cooled down through free convection, a

digital oscilloscope recorded the thermocouple voltage. A computer program recreated the experimentally measured temperature history. The Nusselt number correlations assumed free convective flow, and the gas temperature T_g, the fin temperature T_{fin}, and the ambient temperature T_w were all assumed to be 300 K. The variables were the junction diameter D_1 and the emissivity of the thermocouple junction ϵ. The junction diameter was varied with a fixed emissivity until the computer results were sufficiently close to the experimental curve. Then the emissivity was varied until the best agreement was obtained in a least-square sense. This program is listed in Appendix A.

Figure 10 shows the cool-down tests. The solid line is the experimental data, and the dashed lines are the predictions of the computer program. Three thermocouple cool-down tests were conducted: one for the large thermocouple, a second for the fine thermocouple, and a third for a replacement fine thermocouple (after the first one failed during an experiment). The effective diameters of these thermocouples were estimated to be 36 mils (0.90 mm), 6.3 mils (0.16 mm), and 6.9 mils (0.17 mm), respectively. The term "effective diameter" is especially appropriate for the large thermocouple, since its junction was not spherical. The junction was football-shaped, with a width of about 30 mils (0.75 mm) and a length of about 50 mils (1.25 mm). The assumption of a 36-mil spherical junction is validated by the agreement between the model and the experiment. The emissivity had a much smaller effect on the agreement between the experiment and the model. The relatively low thermocouple temperatures during this test

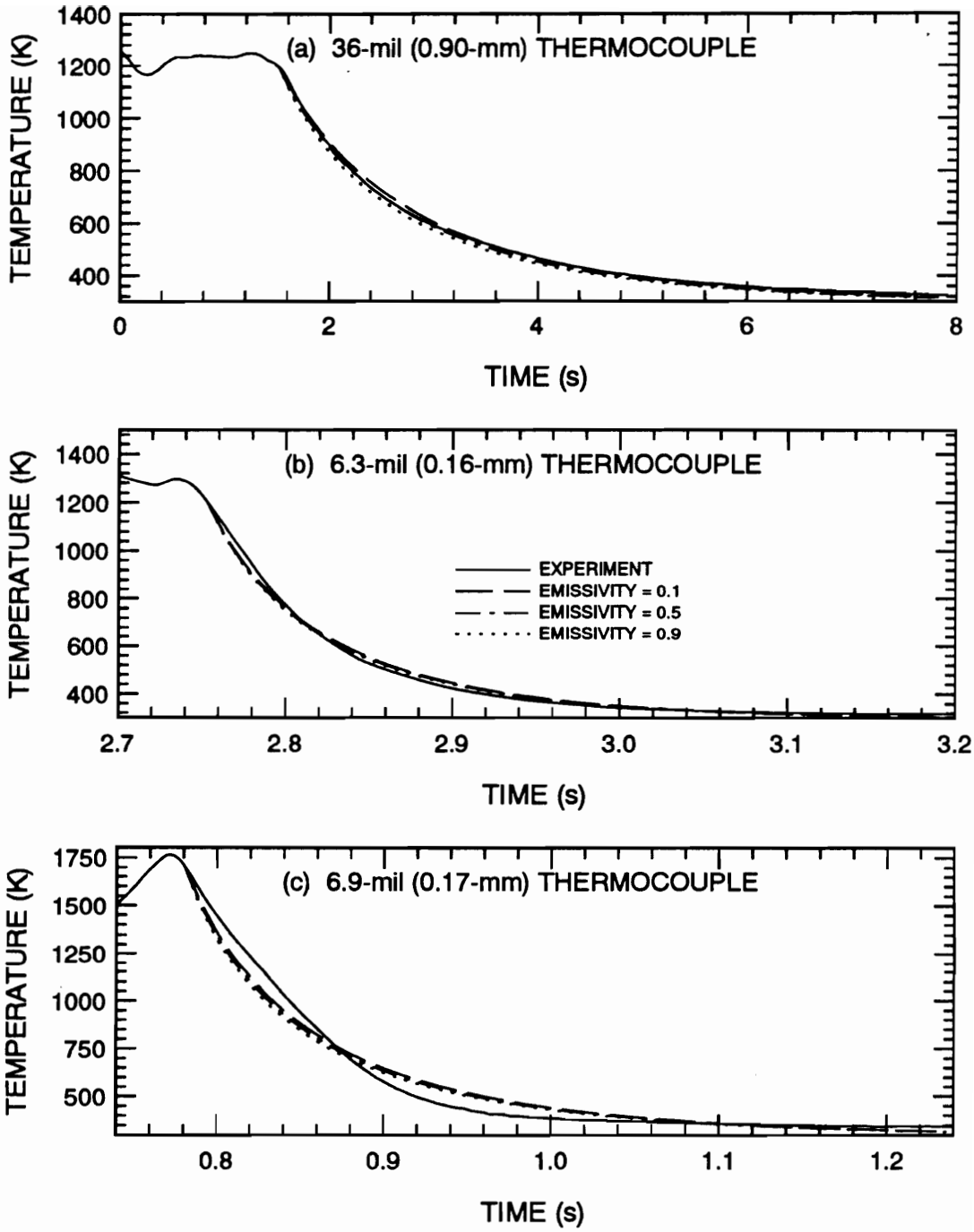

Figure 10 Thermocouple Cool-Down Tests.

would suppress the importance of the radiation term, while the junction diameter still influences the convection and heat storage terms. An effective emissivity of 0.3 was assumed for all three thermocouples. The predicted junction diameters were still consistent with the estimates obtained using the microscope, and the predicted emissivity falls in the range of published values. The good agreement suggests that the thermocouples have been modeled correctly.

2.7.6 Thermocouple Temperature Corrections

The measurement errors of the thermocouples were estimated using the effective diameters and emissivities of the thermocouple junctions. Due to radiative losses from the junction to the surroundings and conductive losses through the leads, the thermocouple temperature is lower than the true gas temperature. This deficit was predicted with a second computer program using the same thermocouple model. Two significant differences from the previous program are noted. The Nusselt number correlations assume forced convection, and the fin temperature is allowed to vary from the gas temperature. For an assumed thermocouple temperature T_c, the program predicts the true gas temperature T_g. The solution is iterative. A fin temperature is guessed, and equation (11) predicts the gas temperature required to balance radiation and convection heat transfer in the fin. Equation (10) is checked to see whether radiation, convection, and conduction are balanced in the junction. The guess for T_{fin} is modified until the

solution converges. The FORTRAN code for this program is listed in Appendix B. The correction terms for the three thermocouples are:

$$\text{TCORR (36 mil)} = 18.3 - 1.22\times10^{-1}\,T_c + 1.77\times10^{-4}\,T_c^2$$

$$\text{TCORR (6.3 mil)} = 14.9 - 5.15\times10^{-2}\,T_c + 5.08\times10^{-5}\,T_c^2$$

$$\text{TCORR (6.9 mil)} = 15.7 - 5.43\times10^{-2}\,T_c + 5.35\times10^{-5}\,T_c^2$$

TCORR is the temperature correction term added to the thermocouple junction temperature in degrees K.

The predictions of the program are not entirely consistent with practical experience. Based on the observed luminosity of the thermocouples, the junction was certainly always hotter than the end of the leads. However, the only stable solution to the program usually converged with the fin temperature slightly greater than the junction temperature. In all cases, the magnitude of the conduction term is less than 25 percent of the radiation or convection terms (it was usually about ten percent). Despite the disagreement with observations, the conduction term was left in the program because it was so essential in predicting the transient response of the thermocouple in the cool-down

tests. The junction leads are oriented parallel to the flat flame, so that conduction effects are minimized in the thermocouples.

An error is introduced as the thermocouple measurements are made closer to the flame zone. The radiation component of the model assumes surroundings at 300 K, but when the thermocouple is right against the flameholder half of its environment will be at the flame temperature. At this measurement location, radiative losses from the thermocouple should be lower, and the temperature correction suggested by the model is a bit high. Figure 11 shows the correction terms for the thermocouples. Figure 11 (a) shows the correction terms for the large thermocouple as a solid line, and a second correction curve as a dashed line. For this dashed curve, the radiation term of the model was halved to reflect the reduced radiation losses when the thermocouple is in the flame zone. The difference is 90 K at a thermocouple temperature of 2000 K. This type of correction is unnecessary for the fine thermocouples since they are never used in the flame zone. All of the measured flame temperatures (with the correction term applied) were below their theoretical adiabatic flame temperatures. This indicates that the magnitude of the temperature correction terms is within reason.

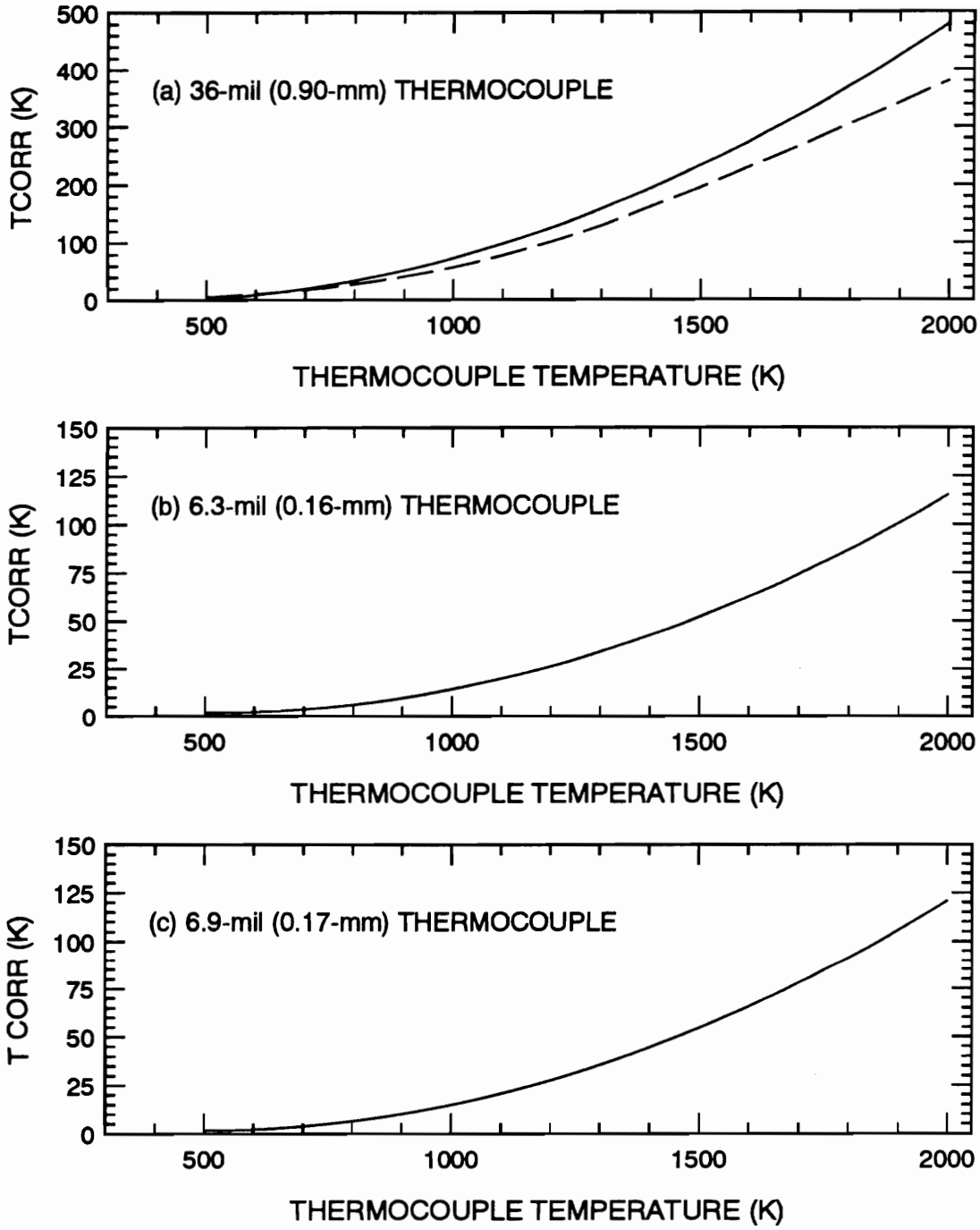

Figure 11 Radiation/Conduction Correction Curves for Large and Fine Thermocouples

2.7.7 Thermocouple Frequency Response

A third computer program predicts the response of the fine thermocouples to fluctuating temperatures. The gas is given a sinusoidal temperature variation and the thermocouple temperature is calculated. The normalized amplitude and phase lag of the thermocouple are predicted as a function of the frequency of the gas temperature fluctuation. The frequency response function A(f) is defined as the amplitude of the thermocouple temperature fluctuation over the amplitude of the gas temperature fluctuation, that is

$$A(f) = \left[\frac{T_{c,\max} - T_{c,\min}}{T_{g,\max} - T_{g,\min}} \right]_f . \tag{12}$$

For a steady state case (i.e. zero frequency, where the amplitude is defined to be zero), the frequency response function has a different interpretation. In this case, the nondimensionalized amplitude A(f=0) is defined as the steady thermocouple temperature divided by the steady gas temperature. Since a deficit always exists in the thermocouple temperature due to losses, the ratio of amplitudes is always less than one. Figure 12 shows the frequency response function and phase lag for the 6.9-mil thermocouple. The cutoff frequency of the thermocouple is near 2 Hz. The response of the thermocouple varies slightly with the mean gas temperature, but it is relatively insensitive to the

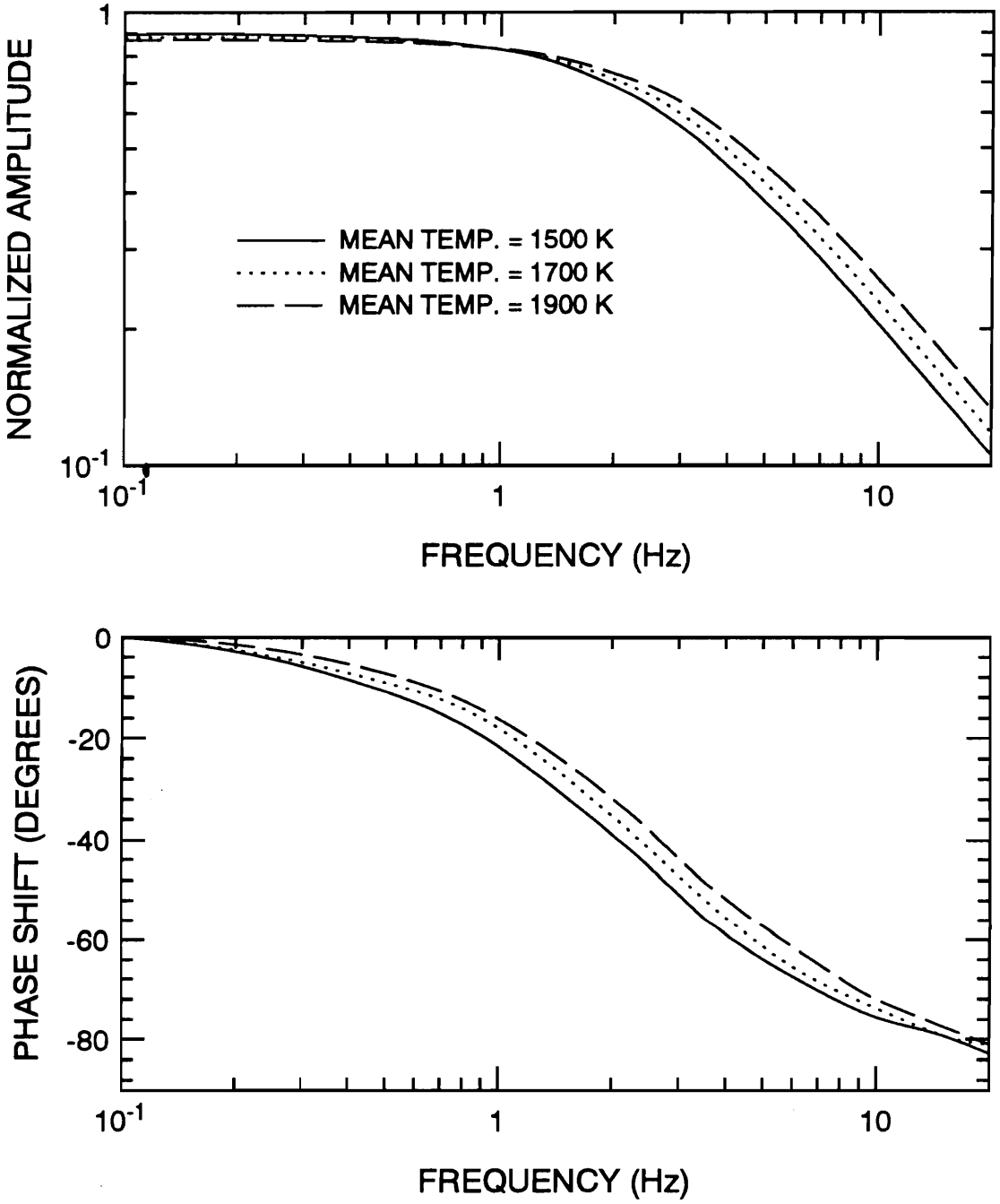

Figure 12 Response of 6.9-mil Fine Thermocouple to Sinusoidally Varying Gas Temperature

amplitude of the gas temperature fluctuation. The frequency response function is used to correct for the attenuated response of the fine thermocouples to high frequency components of the gas temperature fluctuation. The procedure for these corrections is described in Chapter 4.

2.8 PULSE BURNERS

Three different burners were designed, built, and tested. The major difference between the burners was the method of producing an oscillating methane injection. The goal of this development work was to find an injector with uniform spatial injection of methane, so that temporal and spatial effects on NO_x emissions could be separated. Although spatial variations in equivalence ratio were never completely eliminated, they were reduced to an acceptable level. The following section describes the operation of the burner in general, and the details of the three methane injection systems follow.

2.8.1 Design and Development

Several features of the burner remained fixed throughout this development period. The premixed flow of methane and air travels vertically through flow straighteners, past a fuel injector, and into a quartz tube. Quartz was chosen for its ability to withstand the

flame temperatures and for its infrared transmission. The diameter of the tube was fixed by the demands of the optical system, as explained in Section 2.5.2.

The flameholder screen was designed to act as a flashback arrestor. The flame is stabilized against the screen because the laminar flame speed is higher than the velocity of the unburned mixture [21]. The flame cannot traverse the flameholder as long as the size of the holes in the screen is smaller than the quenching distance for the flame. This quenching distance was estimated to be 1.5 mm, but a much finer screen was actually used [22]. The flameholder is a stainless steel screen made of 0.25-mm diameter wires with 0.4-mm square openings. The blockage of this screen is 64 percent. It is supported with three stainless steel wires of 0.4-mm diameter. In the original design, the flameholder was suspended from above. However, the hot flame products corroded and bent the wires, which then interfered with the probe measurements. In the final design the wires support the flameholder from below without blocking the optical path.

The 20-mm diameter quartz chimney tube was used in each burner. This put restrictions on the flammability limits achieved in the burner. Due to heat losses and radical recombination along the walls of the tube, the theoretical lean flammability limit of $\phi = 0.53$ could not be sustained. When this limit is approached from richer equivalence ratios, the stored heat from the previous (hotter) flames supports the reaction at the lean limit for about 15 min. Then the flame lifts off the flameholder and

extinguishes. The sustainable lean flammability limit for this burner is a mean equivalence ratio of 0.66 for a mean cold-flow inlet velocity of 21 cm/s at 0 °C and 1 atm (STP). The losses in the burner have reduced the laminar flame speed from that expected in an adiabatic flame at the same equivalence ratio.

Leaner flames could be maintained at lower flow velocities, but then it became more difficult to optically resolve individual pulses of methane in the unsteady flames. The flameholder's ability to anchor a flat, well-behaved laminar flame depends on a flow velocity slower than the laminar flame speed. For the pulsing flames, there is a tradeoff between the mean flow velocity and the axial spacing of the individual pulses of methane. Suppose that methane is injected at 10 Hz, and the mean flow velocity is 40 cm/s. Then the spacing between successive peaks would be 4 cm. However, if the mean flow velocity is only 20 cm/s, the pulses are only 2 cm apart. It should be noted that a lower flow velocity not only decreases the physical separation of adjacent pulses in the flow, but it also lengthens the time allowed for diffusion between pulses. Clearly, the pulses then have a greater potential to interdiffuse during the time between injection and when the pulses reach the flame zone. The minimum practical flow velocity was set to 21 cm/s at STP, and at this speed the methane injection frequency limit was 10 Hz. At 10 Hz the optical signal looked like noise, and the amplitude of the equivalence ratio fluctuations was much less than that achieved at lower frequencies. The amplitude of the

signal indicated that the pulses had not blended into a uniform mixture, however. These considerations place a definite upper limit on the pulse frequency for a laminar flame.

A mass diffusion model has been used to establish the relationship between the bulk flow velocity of the reactant gases and the methane injection frequency limit. The results of the model are shown in Figure 13. Pure air flows with a mean velocity V, and pure methane is injected with a frequency f. The physical spacing between adjacent pulses L equals V/f. The injected methane is assumed to form infinitely thin planar sheets. The concentration of methane as a function of distance x and time t is

$$\frac{C(x,t)}{C_o} = 1 - erf\left[\frac{x}{2\sqrt{D_{AB}\,t}}\right] \quad . \tag{13}$$

The quantity C_o is the methane concentration at x = 0, assumed to remain at 100 percent. Methane diffuses from the injection plane at x = 0 to the midplane between the pulses at x = L/2, for a time equal to τ, where τ is the time delay between methane injection and combustion. The quantity τ is the distance between the methane injector and the flameholder, X, divided by the flow velocity V. The concentration of methane at the midplane x = L/2 at the time delay τ is

$$C\left[\frac{L}{2},\tau\right] / C_o = 1 - erf\left[\frac{V^{3/2}}{4f\sqrt{D_{AB}X}}\right] \quad . \tag{14}$$

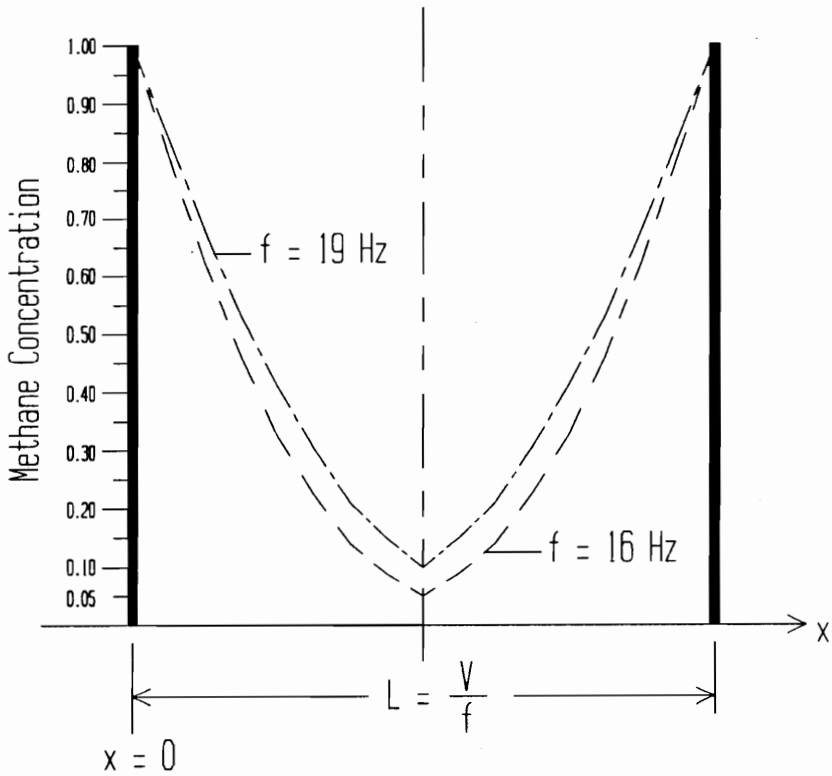

Figure 13 Methane Diffusion Between Adjacent Pulses

The concentration at the midplane reaches five percent methane if the injection frequency is 16 Hz, and the concentration at the midplane reaches ten percent if the injection frequency is 19 Hz. These methane concentrations are approximately the lean limit and stoichiometric equivalence ratios, respectively. The calculation assumes a velocity under laboratory conditions of 0.245 m/s, a separation between methane injector and flameholder of 0.064 m, and a bimolecular diffusivity D_{AB} between methane and air of 2.9×10^{-5} m^2/s. This shows that the practical limit for the methane injection frequency is on the order of 19 Hz. In reality, the methane concentration at $x = 0$ would not remain at 100 percent, diminishing the gradient forcing the diffusion. This is counteracted by the nonzero duty cycle, which leads to finite pulse thicknesses of methane and so decreases the effective pulse separation L. The experimental injection frequency limit of 10 Hz is consistent with the calculations. Equation (14) shows that the injection frequency limit can be increased only if the spacing X between the injector and the flameholder decreases or the velocity of the reactant gases is increased. The velocity is limited by the performance of the flameholder, however.

Theoretically, the flow velocity can be increased as long as the equivalence ratio is richer than 0.66, since the higher flame speed would balance the increased flow velocity. However, the heat transfer within the burner also plays a role. Figure 14 (a) shows the correlation between the NO_x emissions and the equivalence ratio for a series of steady flames, and Figure 14 (b) shows the correlation between NO_x emissions and

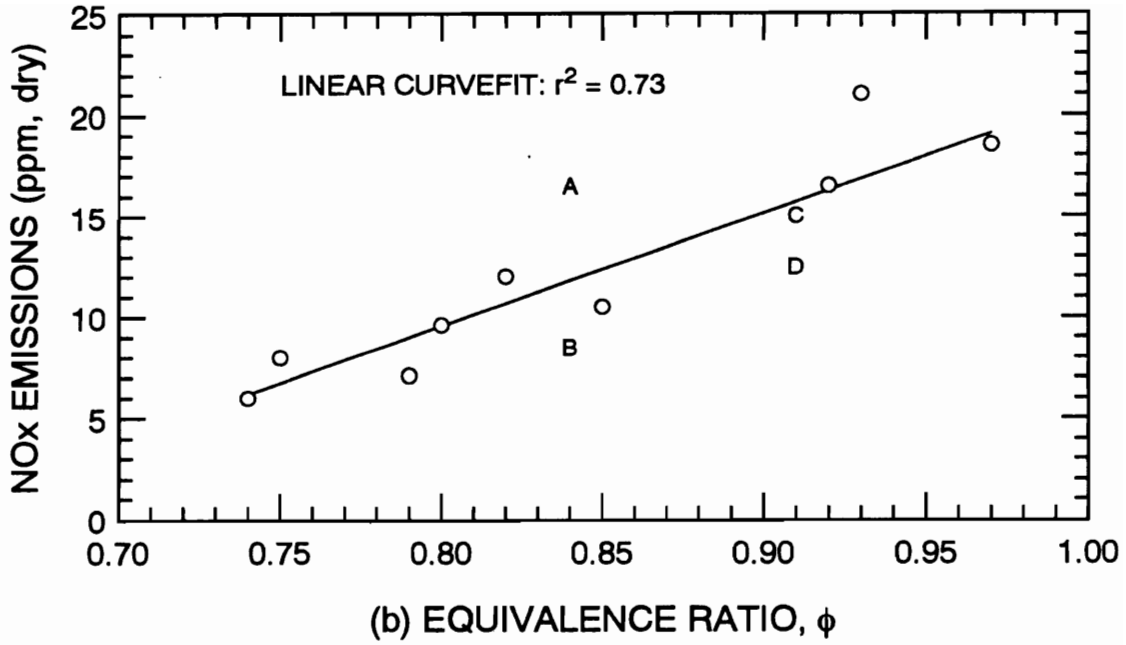

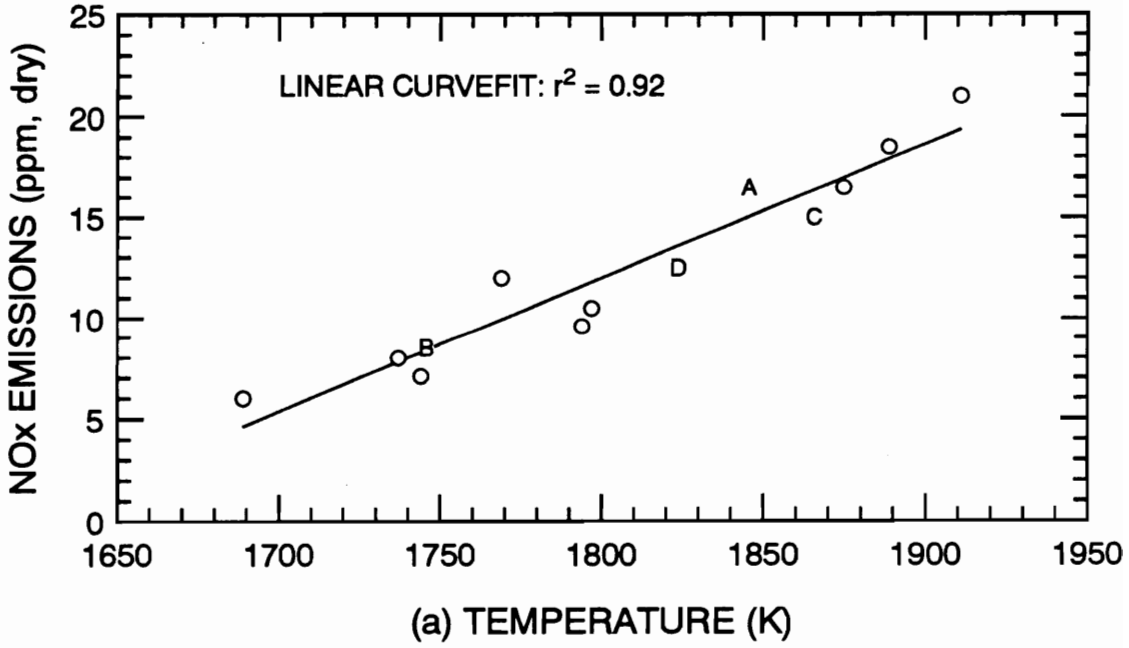

Figure 14 Correlations Between NO_x Emissions and Equivalence Ratio or Temperature for Steady Flames

flame temperatures. While a straight line would not be expected to fit the data over a larger temperature range, for this limited data set it does to a good approximation. The correlation coefficient r^2 is a measure of the goodness-of-fit between the data and the line [33]. The correlation between temperature and NO_x emissions is much better than the correlation between equivalence ratio and NO_x emissions. Two flame pairs in particular illustrate the role of heat transfer in the burner. The symbols A and B represent two steady flames at the same equivalence ratio, but the flow velocities were different for each experiment. The higher NO_x emissions occurred for the higher flow rate. The symbols C and D are analogous. Figure 14 (a) shows that the NO_x emissions were different between the cases, whereas Figure 14 (b) shows that the NO_x emissions are still consistent with the temperature measurements.

The results of this test caused several aspects of the experiment to be modified. First, since the heat transfer and thus temperatures are related to the flow rate, the flow rate had to remain fixed to permit comparisons between flames. The air flow rate was fixed at 3.95 ℓ/min at STP for all of the flames. Variations in the methane flow rate for flames at different equivalence ratios would alter the mean flow velocity by less than 5 percent, and this was considered to have a negligible effect. The total methane flow rate was between 0.2 and 0.4 ℓ/min at STP for the leanest to the stoichiometric mixtures, respectively. However, in order to reduce the effects of the heat transfer even further, insulation was placed around the burner in the vicinity of the flame zone. This also

lowered the burner's sustainable lean flammability limit, which had been greater than $\phi = 0.66$ beforehand, probably due to higher heat transfer rates and increased quenching at the quartz chimney walls. Leonard and Correa observed a lean flammability limit of $\phi = 0.7$ in a 51-mm diameter uninsulated burner at 10 atm [34]. Wall quenching effects should be greater in the burner for this experiment due to the smaller diameter and the greater mean free path of the gas molecules at atmospheric pressure. The improvement in the lean flammability limit over Leonard and Correa's burner is therefore probably due to the insulation. Finally, the results of this test cast doubt on the usefulness of equivalence ratio measurements to characterize the combustion conditions. After this test the fine thermocouple probe was designed and the emphasis of the experiment was shifted towards the thermocouple measurements.

2.8.2 Version One: Solenoid Valve Burner

Figure 15 shows the original burner designed, built, and tested for this experiment. The methane injector uses a solenoid-powered valve and a toroidal injection manifold. When the valve is open, methane can flow into the injection manifold. The methane is split by a tee, enters the manifold through the two legs which support the manifold ring, and flows out through holes in the perimeter of the ring. There are four holes on the inner diameter of the ring and fourteen holes on the outer diameter. This ratio was chosen because the cross-sectional area within the ring is 2/7 the area of the

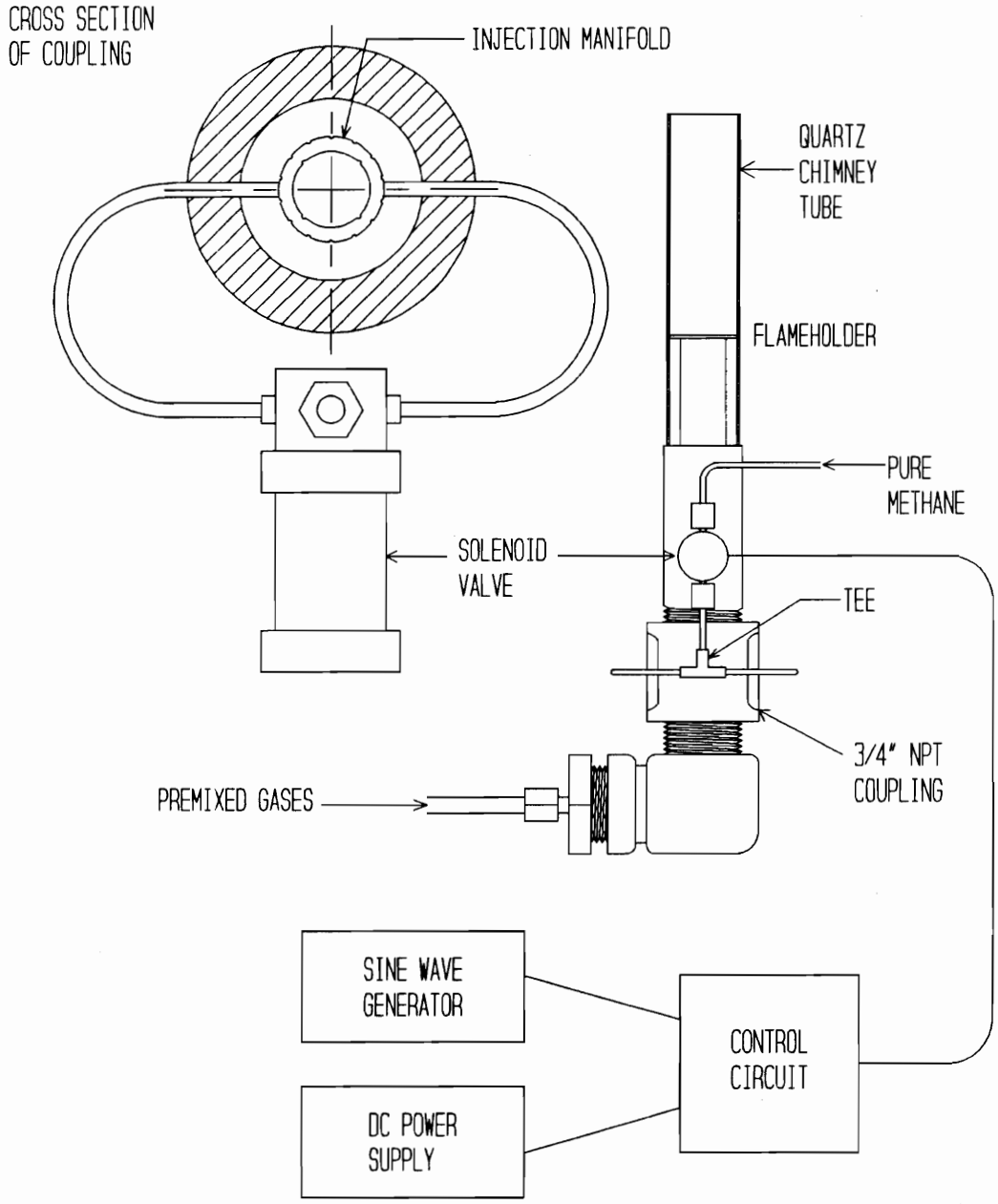

Figure 15 Solenoid Valve Burner

annular cross section outside the ring. Assuming equal mass flow rates through the holes, the methane would be distributed as evenly as possible spatially. Due to the discrete number of jets, some radial and circumferential diffusion of the methane would be needed to achieve a uniform spatial distribution of methane in a plane normal to the burner axis.

The solenoid valve was a Clippard model EIO3-15.5 intrinsically-safe valve. The low voltage of the solenoid ensured that any combustible mixture in the valve could not be ignited accidentally. The valve would operate at up to 70 Hz, although in practice it was not used above about 10 Hz. The solenoid was opened and closed with a 16-V square wave whose frequency and duty cycle could be changed. The duty cycle is defined as the portion of time that the valve is open in each cycle. For example, if the valve stays open for one-quarter of the cycle and closed for three-quarters, the duty cycle is 25 percent (regardless of the frequency of the valve).

Figure 16 shows a schematic of the electrical circuit that controls the valve. A 5-V sine wave from a function generator opens and closes a transistor gate, allowing a 16-V D.C. power supply to periodically energize the solenoid. The duty cycle is controlled by the resistor-capacitor time constant τ=RC of the circuit. A fixed-size capacitor C is used with a variable resistor R. The valve was unable to respond if the time constant was set below 7 ms (corresponding to the 70 Hz limit of the valve).

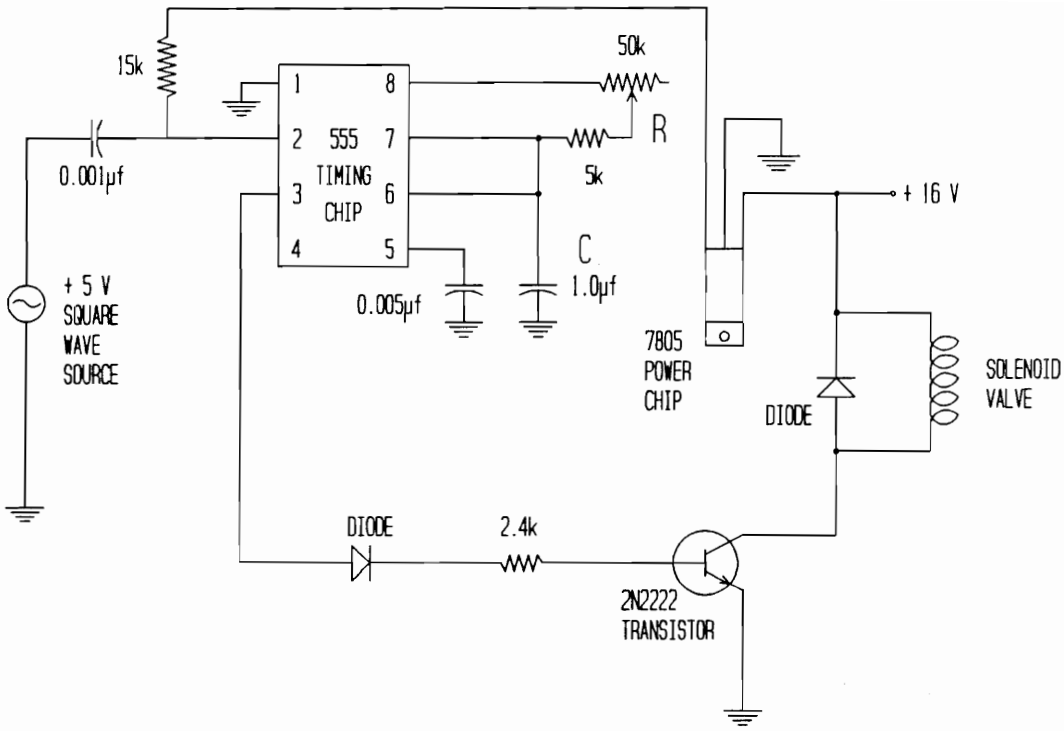

Figure 16 Control Circuit for Solenoid Valve

Shortening the duty cycle of the valve reduces the amount of methane injected with each pulse. Lowering the pressure of the methane supplied to the valve has the same effect.

The ability of this fuel injector to meet its performance goals was primarily limited by the construction of the injection manifold. The holes were drilled before the manifold was bent into its circular shape; the bending made the I.D. holes slightly smaller and the O.D. holes slightly larger. The mechanical connections (reconnecting the ends of the ring and attaching the two legs) were made with silver solder, and some of this material inevitably entered the tubing at each weld. The amount of blockage at each weld could not be determined, but tests indicated that the flow through the manifold was not symmetrical.

The injection manifold created another concern due to its internal volume. There is a time delay as the pulse valve opens, the manifold is filled with methane, the gas in the manifold is compressed, and the methane flows out through the holes. This time delay is related to the acoustic impedance of the injection holes and the internal volume of the manifold; acoustically, the injector has some unknown natural frequency. It was feared that the 10-Hz limitation observed in optically resolving individual methane pulses was due to the manifold's frequency response. Another fuel injector was designed to minimize any possible acoustic effects and to improve the spatial distribution of the injected methane.

2.8.3 Version Two: Coaxial Twist Burner

The second methane injection system is called the coaxial twist model. Functionally, this injector is designed to put all of the pressure drop at the site of the fuel injection, thereby simplifying the acoustic circuit. Figure 17 shows its construction. Its key feature is two coaxial tubes. The inner tube contains methane and rotates at a constant speed within a fixed outer tube. At the lower end of the assembly, an O-ring seal prevents methane leakage to the surroundings. Two roller bearings support the rotation of the inner tube. A series of small holes located between the two roller bearings allows methane to reach the interior of the inner tube. A solid molybdenum-filled nylon sleeve fixed to the top of the inner tube is self-lubricating and slides against the inside surface of the outer tube. Six holes were drilled radially through the outer tube, the sleeve, and into the inner tube. As the inner tube rotates, all six holes line up every 1/6 of a revolution and the methane escapes as jets into the premixed flow. As the tube continues to turn the flow is blocked off until the next alignment of the holes occurs. The frequency of the injection pulses and the rotational speed of the inner tube were controlled by a variable-speed motor.

Unfortunately, the nylon sleeve could not adequately seal off methane leakage while the holes were not in alignment. The leakage alone was sufficient to maintain a flame even when the steady flow was pure air, and an excessive amount methane was

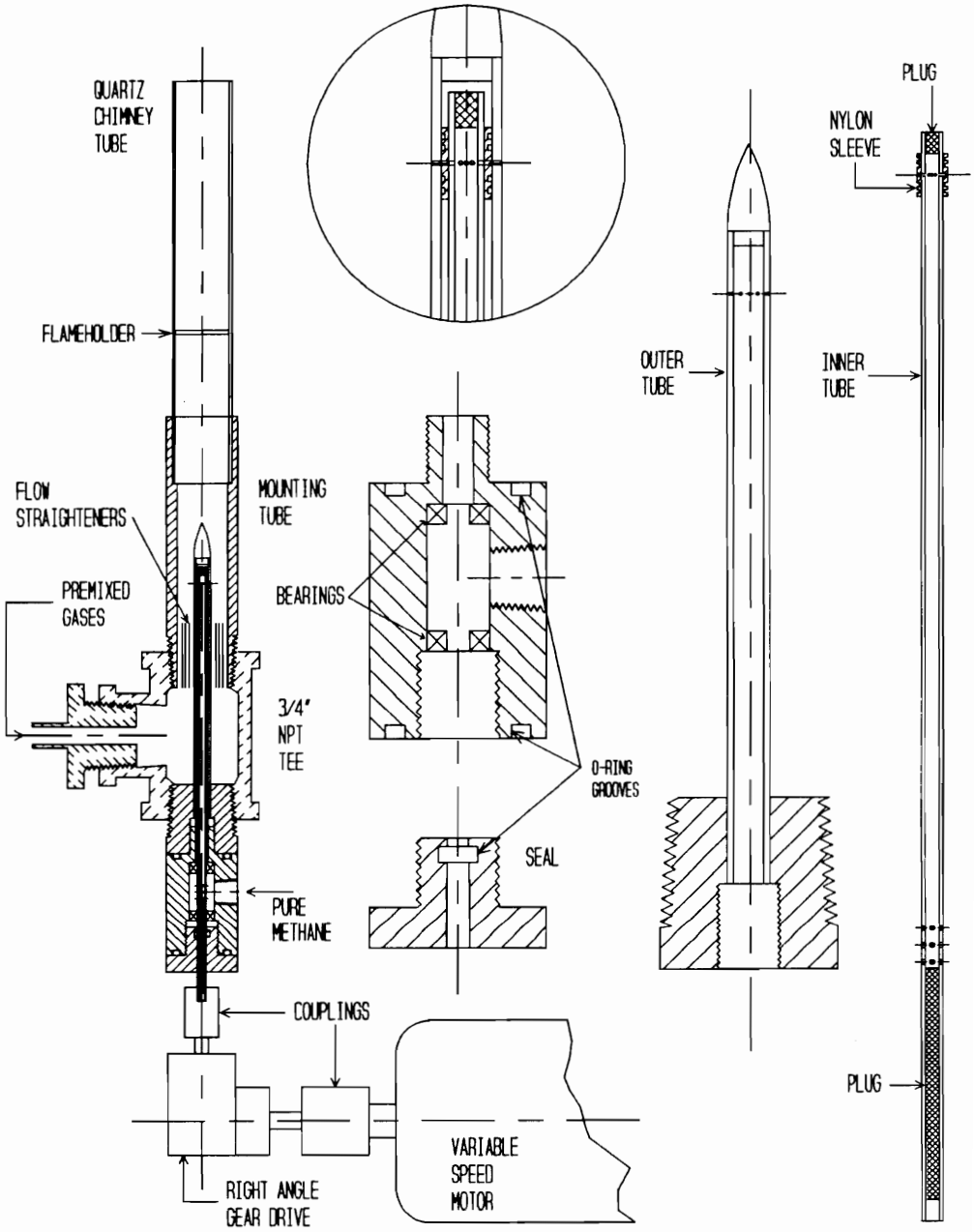

Figure 17 Coaxial Twist Burner

injected whenever the holes were aligned. During operation the flame jumped off the flameholder screen and anchored at the top of the quartz tube. A tighter fit for the sleeve might have helped, but this would have caused more friction and possible seizing after continuous use. Other operational problems made this an impractical fuel injector. The vertical alignment of the holes was difficult to maintain. Adequate alignment was difficult to obtain between the burner, the right angle gear drive, and the variable-speed motor. Inaccurate alignment caused the burner itself to move, and the motion of the quartz tube affected the optical measurements. Additionally, wear products from the nylon sleeve tended to block the injection holes. A few tests were run with this injector before concluding that it was not an improvement over the solenoid valve design.

2.8.4 Version Three: Cam-Driven Burner

Figure 18 shows the third injector design. It consists of three major parts: the quartz chimney tube, an aluminum mounting tube, and a plug assembly of brass. The quartz tube surrounds the flameholder screen. The quartz fits into a socket in the mounting tube with an O-ring seal. A ceramic fiber insulator surrounds the lowest 9 cm of the quartz tube, centered about the flameholder. A 6-mm diameter hole allows passage of the infrared laser beam through the insulation. The insulation reduces the heat transfer from the quartz tube, allowing leaner flames to be stabilized on the flameholder screen. Premixed methane and air enters through a fitting in the side of the mounting

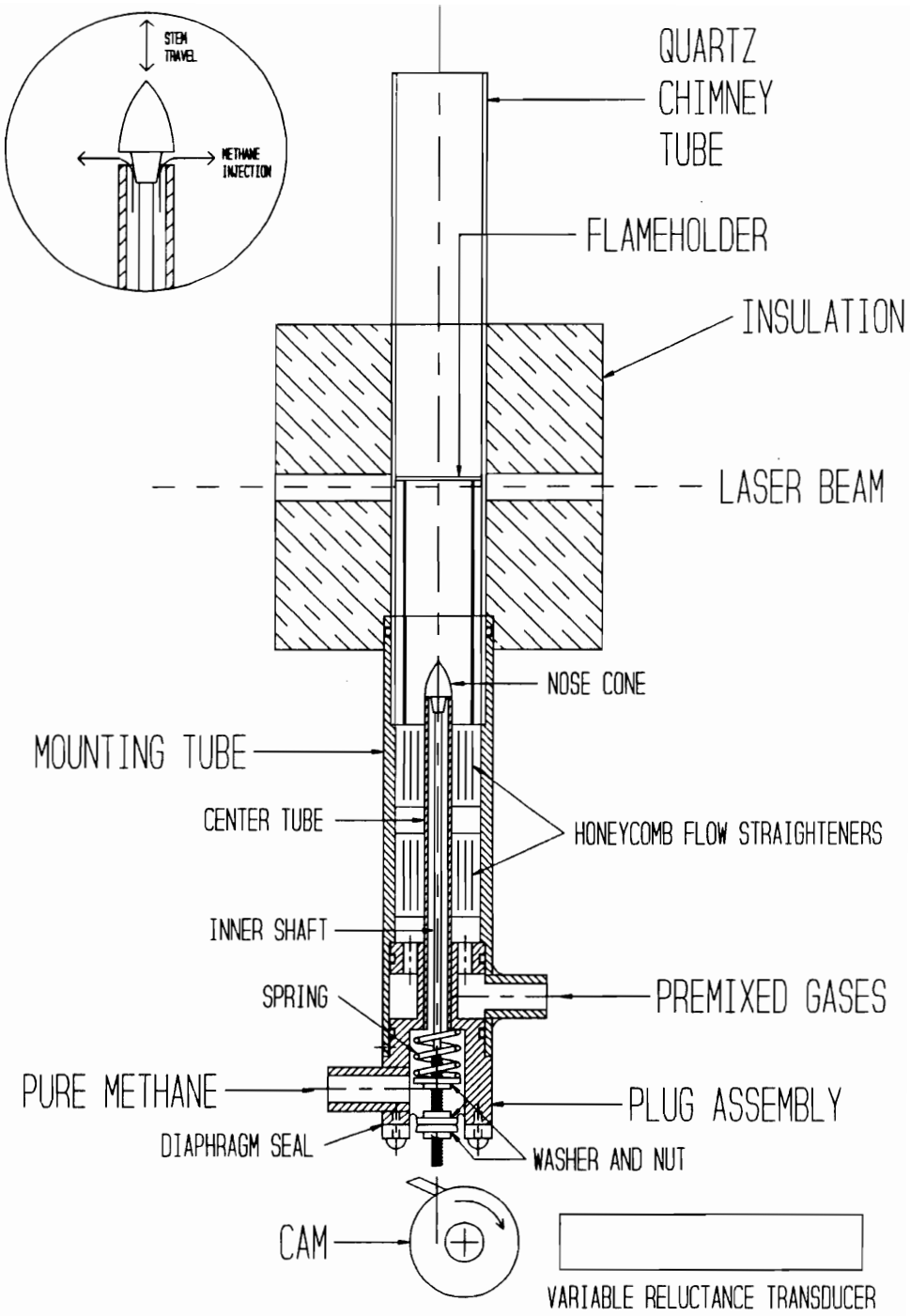

Figure 18 Cam-Driven Burner

tube. The gases enter an annular space and are distributed by a series of 3.175-mm diameter holes. The premixed gases flow vertically through two flow straighteners made of aluminum honeycomb (1-mm cell size). The mounting tube is oriented by a bracket on a vertical translator.

The most complicated part of the assembly is the lower plug, which contains the methane injection mechanism. Pure methane enters through a fitting at the bottom of the burner. The injector is held closed by a spring, and it opens when a cam pushes against the lowest part of the inner shaft. From the lowest to the highest point, the inner shaft consists of nylon all-thread, aluminum tubing, and a nylon nose cone. This inner shaft fits coaxially inside the center tube, and methane fills the annular space. Whereas the nose cone was fixed in the previous burner, in this model it lifts to permit methane flow. Methane leakage is prevented by two O-ring seals and a diaphragm seal in the plug assembly. The low mass of the inner shaft and the stiffness of the spring give the valve a natural frequency above 100 Hz.

The drive cam is mounted directly on the shaft of a variable-speed motor (Electro-Craft model 550-0, with model E-652-0 speed controller). The rotational speed of the motor can vary between 3 and 3000 RPM; it usually operated in the 120 to 600 RPM range to pulse the methane injector at 2 to 10 Hz. Figure 19 shows the design of the cam. The original cam shape was a circle with an eccentric axis, so that the outer

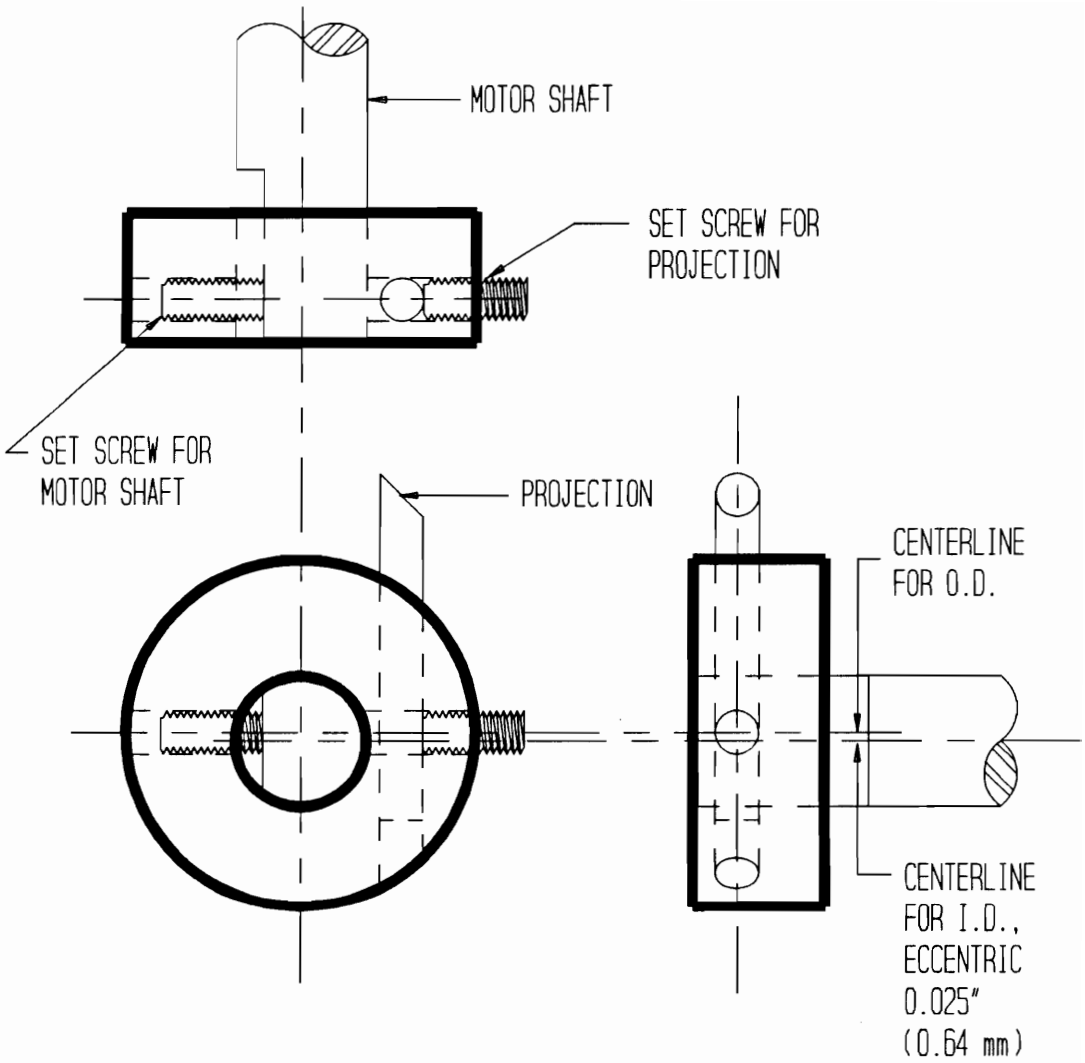

Figure 19 Cam for Cam-Driven Burner

surface would raise and lower the inner shaft without abrupt contact. However, the duty cycle of this cam was too long, and the travel of the inner shaft could not be varied independently from the duty cycle. The duty cycle has to be brief to avoid injecting excessive amounts of methane. The cam was modified so that the duty cycle would remain very brief but the travel of the inner shaft could be changed. A finger-like projection strikes the inner shaft with each cam revolution. The bevel on the end of the projection maintains a flat contact between the cam and the inner shaft. A variable-reluctance transducer measured the rotational speed of the cam. The motor and cam are bolted securely to the optical bench, and the burner is mounted over the cam on a vertical translator. The travel of the inner shaft is controlled by changing the vertical position of the entire burner with the vertical translator and by the placement of the cam/motor.

2.9 DATA ACQUISITION

Most of the data acquisition was computer controlled through a Data Translation model 2811-PGH A/D board and a personal computer. The 8-bit A/D board would accept an input range of zero to five volts, and four channels were used. Each channel collected 200 samples at a frequency of 50 Hz. The four channels read:

- lock-in amplifier voltage (i.e. optical intensity I or I_o)
- NO_x analyzer voltage
- variable reluctance transducer signal (pulse frequency)
- thermocouple voltage (amplified × 52)

Data are stored under a specified file name, along with a trailer which notes:

- time and date of the test
- laboratory temperature and pressure the day of the test
- air and methane flow rates through the rotameters
- back pressure of injection methane
- approximate pulse frequency
- vertical position of the burner
- number of samples collected (200)
- sampling frequency (50 Hz)
- number of channels (4)
- settings for the lock-in amplifier

CHAPTER 3

RESULTS

This chapter presents the experimental results. It covers the calibration of the optical system and the temperature, equivalence ratio, and NO_x measurements from the three types of flames. The results from the steady flames are presented first, followed by the results from the spatially nonuniform flames and then from pulsing flames. While some of the implications of these results are mentioned here, the analysis and modeling of the flames are presented in Chapter 4.

3.1 CALIBRATION OF OPTICAL SYSTEM

The optical system was calibrated by flowing mixtures of known equivalence ratio through the burner and measuring the extinction I/I_o. Figure 20 shows the experimental data and a least-squares linear curvefit. The dashed lines are error bars representing the 95 percent confidence intervals for the calibration. They represent $\pm$ 2 standard deviations of the spread of the data about the line. This means that for any given measurement of $-\ln(I/I_o)$, there is a 95-percent probability that the true equivalence ratio

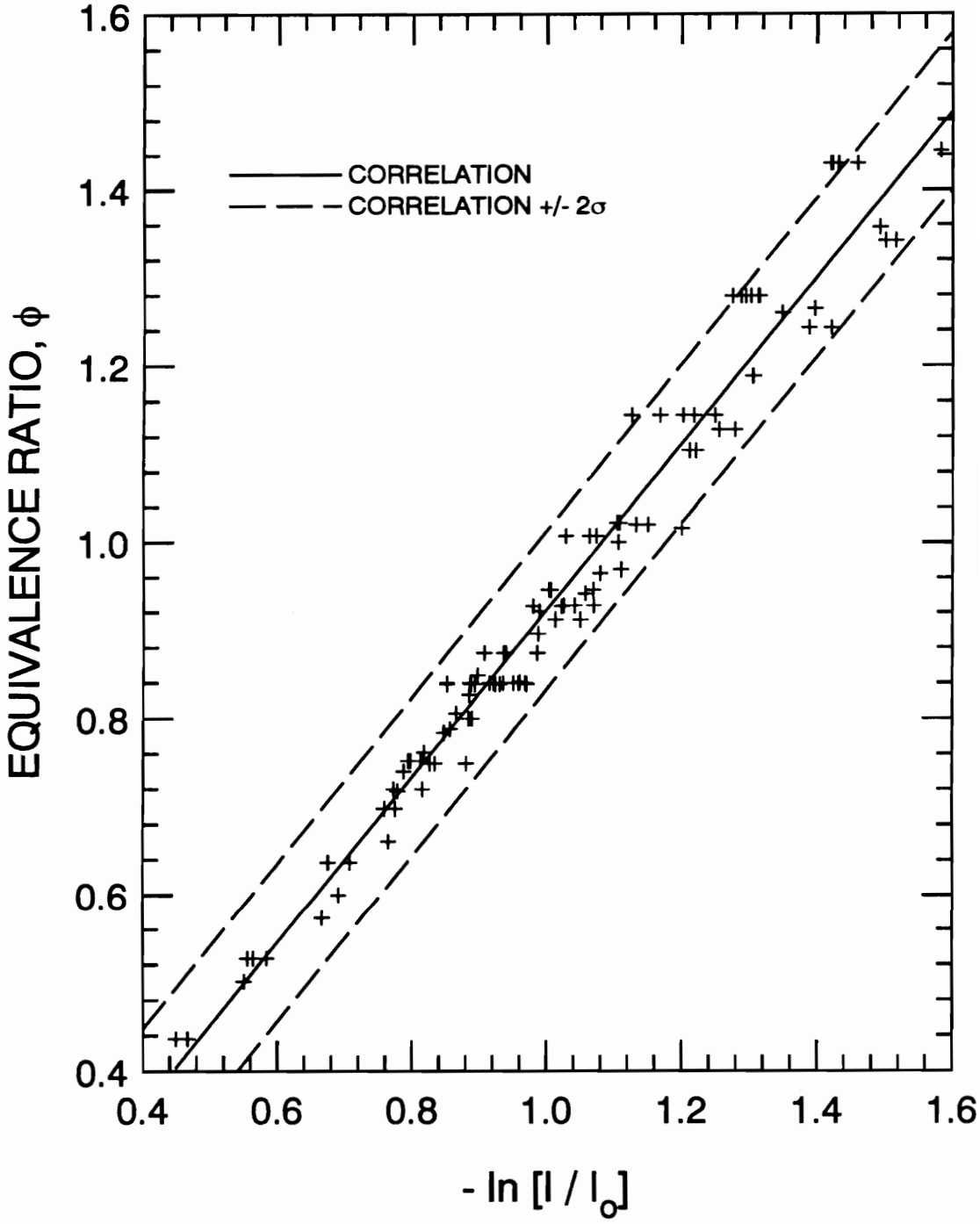

Figure 20 Calibration of Optical Equivalence Ratio Measurement System

is within plus or minus 0.09 (2σ) of the calculated equivalence ratio [33]. The correlation equation for the optical system is

$$\phi = -0.944 \ln \left[\frac{I}{I_o} \right] - 0.0203 \quad . \tag{15}$$

Note that the spread of the data is greatest when the equivalence ratio is greater than 1.0, and that the focus of this experiment has been lean flames. This means that the confidence limits are very conservative for most of the measurements, and the actual confidence limits should be more like $\pm$ 9 percent of the mean equivalence ratio.

The degree of spread in these data is most probably due to the output power instability of the laser. It is difficult to test this hypothesis, since it is not obvious how to eliminate possible effects within the infrared detector at the same time. However, the laser seems to be the most likely source of the problem. Over a period of a few minutes the reference intensity I_o could change by up to 10 percent. To minimize its effect, the reference intensity was measured before and after each experiment and the results were averaged.

3.2 STEADY, HOMOGENEOUSLY PREMIXED FLAMES

Table 2 lists the experimental conditions for the steady flame tests. The mean flame temperatures were measured with the large thermocouple, the NO_x measurements were from probe sampling, and the equivalence ratio was determined from rotameter readings. The equivalence ratio varies from $\phi = 0.66$, the lean flammability limit of the burner, to $\phi = 1.5$, the rich flammability limit of the burner.

Figure 21 shows the experimental measurements for the steady flames. The results from the steady flames are used to model the spatially nonuniform and the pulsing flames, and empirical correlations between the measured parameters (NO_x, ϕ, and T) are obtained from these data. Figure 21 (a) shows NO_x emissions as a function of equivalence ratio. The data show that the lean flammability limit of the burner is about $\phi = 0.66$. According to thermal NO_x theory, NO_x is expected to peak near $\phi = 1$ and then diminish in the rich region as the flame temperature drops. In this experiment a slight plateau is observed for $1.0 < \phi < 1.2$, and then the NO_x continues to increase until $\phi = 1.4$. As the rich flammability limit is approached the NO_x emissions decrease. One reason for this behavior could be prompt NO_x [36-38]. Prompt NO_x is formed primarily in the flame zone, rather than in the post-flame gases like thermal NO_x. Furthermore, prompt NO_x rates are governed more by radical concentrations than the flame temperature. In particular, prompt NO_x depends on superequilibrium oxygen

Table 2 Steady Homogeneously Premixed Flames

Experiment Number	Flame Temperature (K)	NO_x (ppm, dry)	Equivalence Ratio
68	1746	11	0.75
69	1930	32	0.93
71	1806	18	0.84
72	1555	5.2	0.66
73	1814	17	0.79
74	1662	8.4	0.71
75	1843	22	0.88
81	1948	29	0.93
82	1733	12	0.75
85a	2011	48	1.0
85b	2050	42	0.97
85c	2084	52	1.0
85d	2081	52	1.1
86a	2120	53	1.1
86b	2081	52	1.2
86c	1941	71	1.4
86d	1885	73	1.4
86e	1787	47	1.5
86f	2016	64	1.3
86g	2007	54	1.0

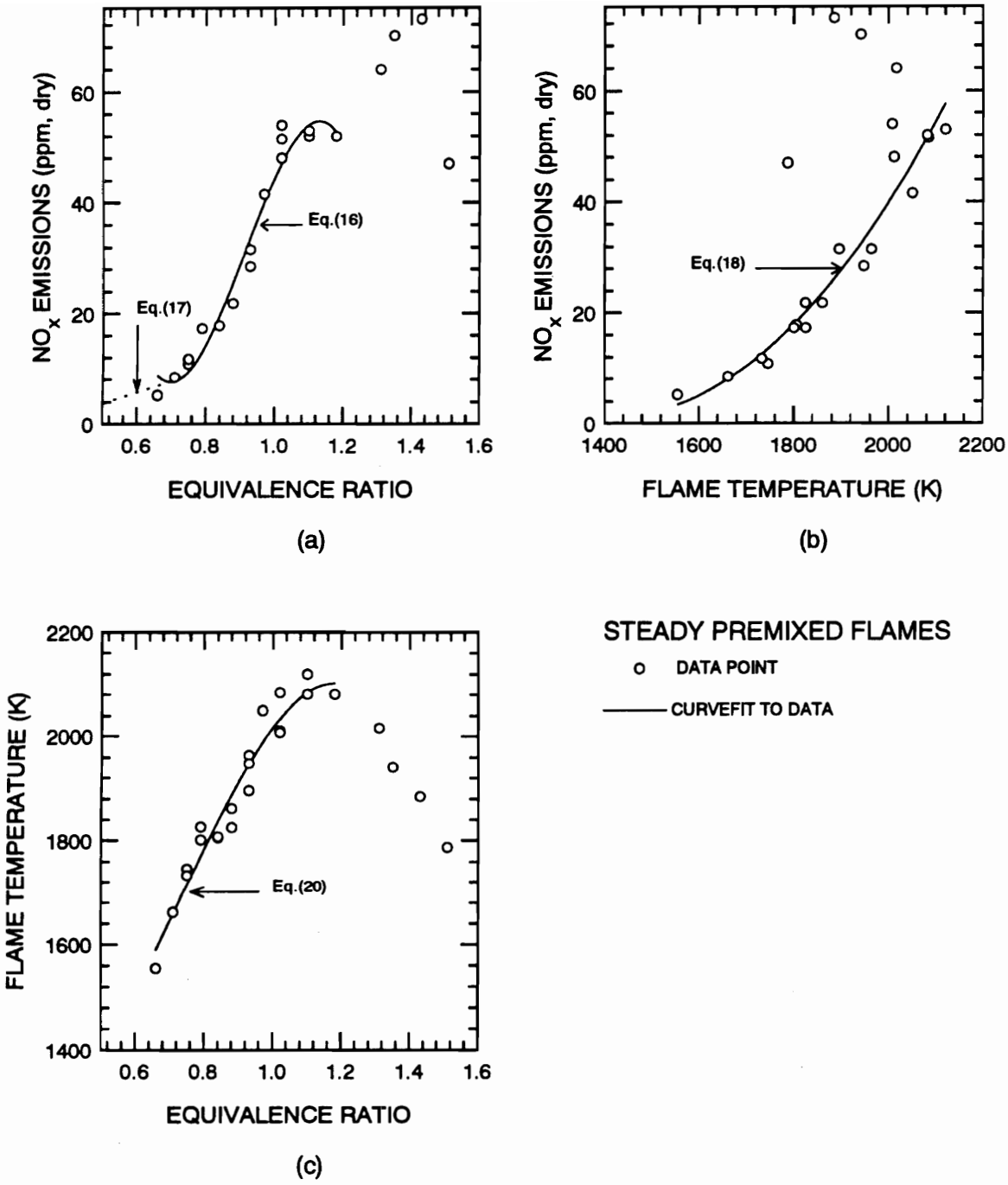

Figure 21 Experimental Measurements for the Steady Flames

radical concentrations and the presence of radical hydrocarbon species which are only found in rich flames [39]. Fenimore reports that intercept NO_x for his methane-air flames peaked when $1.3 < \phi < 1.5$, and his intercept NO_x levels are on the order of 10 to 40 ppm [40]. However, it is uncommon to see *final* NO_x levels continuing to increase into the rich regime. Two notable exceptions may be cited. Iverach et al. obtained very similar results using acetylene, ethylene, and propane as fuels [41]. Maximum NO_x emissions occurred for equivalence ratios between 1.3 and 1.4. Duterque et al. measured peak NO_x emissions in the $\phi = 1.1$ to $\phi = 1.2$ range, but most other researchers have found a much smaller "rich shift" in NO_x emissions or none at all [42].

The prompt NO_x mechanism is only one explanation for the data—it explains how true flame NO_x could be formed and measured despite a decreasing flame temperature. Two other explanations involve sampling errors. One source of error could be NO_x formed in the probe and the sampling system, which is entirely unrelated to NO_x from the flame itself. Another source of error could be the presence of a chemical species that the analyzer cannot distinguish from NO_x. The first source of error seems unlikely. The literature shows that the most common errors in probe sampling are the conversion of NO to NO_2 in the probe and the *destruction* of NO_x in the sampling system before the analyzer [39,43-47]. Conversion of NO to NO_2 would not explain the data from this experiment, since NO_x (NO plus NO_2) was measured. Rich mixtures can reduce the $NO_2 \rightarrow NO$ converter efficiency of the analyzer under some conditions, but this would only

decrease the measured NO_x. The destruction of NO_x through conversion of NO_x back to N_2 and O_2 or absorption of NO_x in the moisture trap would not explain an increase in measured NO_x either.

The other possible sampling error was originally observed by Jaasma and Borman [48]. While using an uncooled quartz probe and a chemiluminescent NO_x analyzer, they noticed a detector response to pyrolysis products of n-heptane formed within the hot probe. The response for methane was significantly less, only 1-2 ppm, since methane forms fewer high molecular weight pyrolysis products. However, their results are dependent on the heating of the probe, and in their tests they were not sampling rich-flame combustion products. Response of the analyzer to pyrolysis products and rich-flame products could account for an unknown proportion of the measured "NO_x" for the rich flames in the current experiment.

Figure 21 (a) shows a solid curve as a fit to the experimental data. This variation of NO_x as a function of the burner equivalence ratio $NO_x(\phi)$ is used later in an empirical model of the flame. The curve is based on the data between the lean flammability limit and $\phi = 1.2$. This omits the data at $\phi > 1.2$, but none of the spatially nonuniform or pulsing flames was richer than $\phi = 1.2$. Note that the inflection point of the curve near $\phi = 0.7$ will cause large errors at leaner equivalence ratios, so a two-part curvefit is used:

$$NO_x(\phi) = 774.7 - 2767\,\phi + 3205\,\phi^2 - 1168\,\phi^3, \quad \phi > 0.7 \tag{16}$$

and

$$NO_x(\phi) = -5.7 + 19\,\phi, \quad \phi \leq 0.7 \quad . \tag{17}$$

The second part of this curvefit relation, equation (17), is shown by the dotted line in Figure 21 (a). The extension of the curvefit below the lean flammability limit of the burner is necessary to model the pulsing flames, which had equivalence ratio fluctuations below $\phi = 0.66$. These fluctuations are possible since $\bar{\phi} = 0.66$ is the *sustainable* lean flammability limit; brief excursions to leaner equivalence ratios are possible as long as the burner is hot enough to maintain the reaction. Although the data in this region would not be truly linear, the error in using a linear function is negligible since the NO_x emissions are so low. Equation (17) assumes that the NO_x emissions fall to zero at an equivalence ratio of 0.3.

Figure 21 (b) shows NO_x emissions as a function of flame temperature. Despite the spread of the data at high temperatures, this figure clearly illustrates the nonlinear dependence of NO_x on temperature. The slope of the curve increases as the temperature increases, and this suggests that fluctuating temperatures should increase NO_x emissions. A temperature increase of a given magnitude produces much more NO_x than an equal

decrease in temperature reduces the NO_x. The integrated effect of these fluctuations about the mean temperature is an increase in NO_x. The solid curvefit is used later in an empirical flame model. The curve has the form

$$NO_x(T) = 237.2 - 0.3311\,T + 1.162\times10^{-4}\,T^2 \quad . \tag{18}$$

Figure 21 (c) shows the flame temperature as a function of the equivalence ratio. The temperature peaks at $\phi = 1.1$ instead of near $\phi = 1.0$. Calculations of adiabatic flames at equilibrium predict that flame temperatures should actually peak slightly richer than stoichiometric, at $\phi = 1.03$ [49]. However, these unsteady flames are neither adiabatic nor at thermodynamic equilibrium. It is possible that the peak temperatures occur in the rich region due to the presence of the quartz tube. A full chemical kinetic model of the burner for the current experiment supports this. Nasser Darabiha at *Ecole Centrale Paris* has modeled premixed flat-flame methane-air combustion in a 20-mm diameter tube. He uses the complete reaction mechanism proposed by Miller and Bowman [50], and accounts for wall effects by emphasizing the importance of catalytic reactions such as

$$CH_4 + WALL \Rightarrow CH_3 + H + WALL \quad . \tag{19}$$

When wall effects are taken into account, the maximum temperature occurs for equivalence ratios in the $\phi = 1.06$ to 1.08 range [51]. Darabiha is also modeling possible catalytic effects of the hot stainless steel flameholder on rich flames, and initial

results show some promise in explaining the data in Figure 21 (a). However, these results are too preliminary to include here. The interested reader should be able to find a publication of this work (authors Darabiha, Wirth, Mahan, and Candel) in the near future. The vertical spread of the temperatures in Figure 21 (c) can be attributed to experimental error. The thermocouple was positioned manually, and the location of the flame zone was estimated by maximizing the thermocouple voltage on an oscilloscope. Small changes in the thermocouple voltage can translate into relatively large changes in temperature, thus the spread in the data. As the equivalence ratio varies, the distance between the flame and the flameholder changes, and the presence of a large thermocouple junction can affect the temperature to a varying degree. This is expected to be more of a problem near stoichiometric equivalence ratios, where the flame approaches the flameholder more closely and the flameholder screen glows red (indicating a screen temperature on the order of 1000 K). Yuuki and Matsui claim that the flame temperature itself is not affected by the proximity of the flame to the flameholder screen [52]. They state "It has been found that T_f is determined solely by G regardless of T_o and wire mesh dimensions." In their nomenclature, T_f is the flame temperature, G is the total flow rate, and T_o is the temperature of the reactant gases. Once again, the solid curve is used later in an empirical model. The curvefit between equivalence ratio and flame temperature is

$$T(\phi) = 1546 - 2225\,\phi + 4978\,\phi^2 - 2282\,\phi^3 \quad . \tag{20}$$

3.3 STEADY, SPATIALLY NONUNIFORM FLAMES

Table 3 lists the experimental conditions for the steady, spatially nonuniform flames. These experiments were performed using the cam-driven burner. The cam position was fixed to hold the inner shaft slightly open, so that a small but steady flow of pure methane was added to the premixed gases. The flow rate of the injected pure methane was not measured directly. The equivalence ratio of the premixed gases ranged between 0.66 and 0.93. The mean flame temperatures were measured with the large thermocouple and the NO_x measurements were from probe sampling. The equivalence ratio parameters are derived from the probe measurements with the total hydrocarbon analyzer. The mean equivalence ratio is the weighted average of the 17 measurements over the flameholder, and the last column reports the unmixedness parameter $s = \sigma/\bar{\phi}$. The probe measurements were made in cold flow, before the flame was ignited. Mean equivalence ratios range from 0.71 to 1.0, and unmixedness ranges from 6 to 21 percent.

3.3.1 Spatial Equivalence Ratio Distributions

The tabulated spatial equivalence ratio distributions are listed in Appendix C. Figure 22 shows the spatial equivalence ratio distribution for Experiment 81. The solid circle represents the inside diameter of the quartz chimney tube. The mean of the distribution is $\bar{\phi} = 1.0$ and its unmixedness s is 8 percent. While this flame did not have

Table 3 Steady, Spatially Nonuniform Flames

Experiment Number	Mean Flame Temperature (K)	NO_x (ppm, dry)	$\bar{\phi}$	$\sigma/\bar{\phi}$ (percent)
81	1864	25	1.00	8
82	1951	50	0.79	6
83	1970	63	0.86	21
84	1738	17	0.71	6
87a	1878	32	0.78	13
87b	1944	40	0.74	10

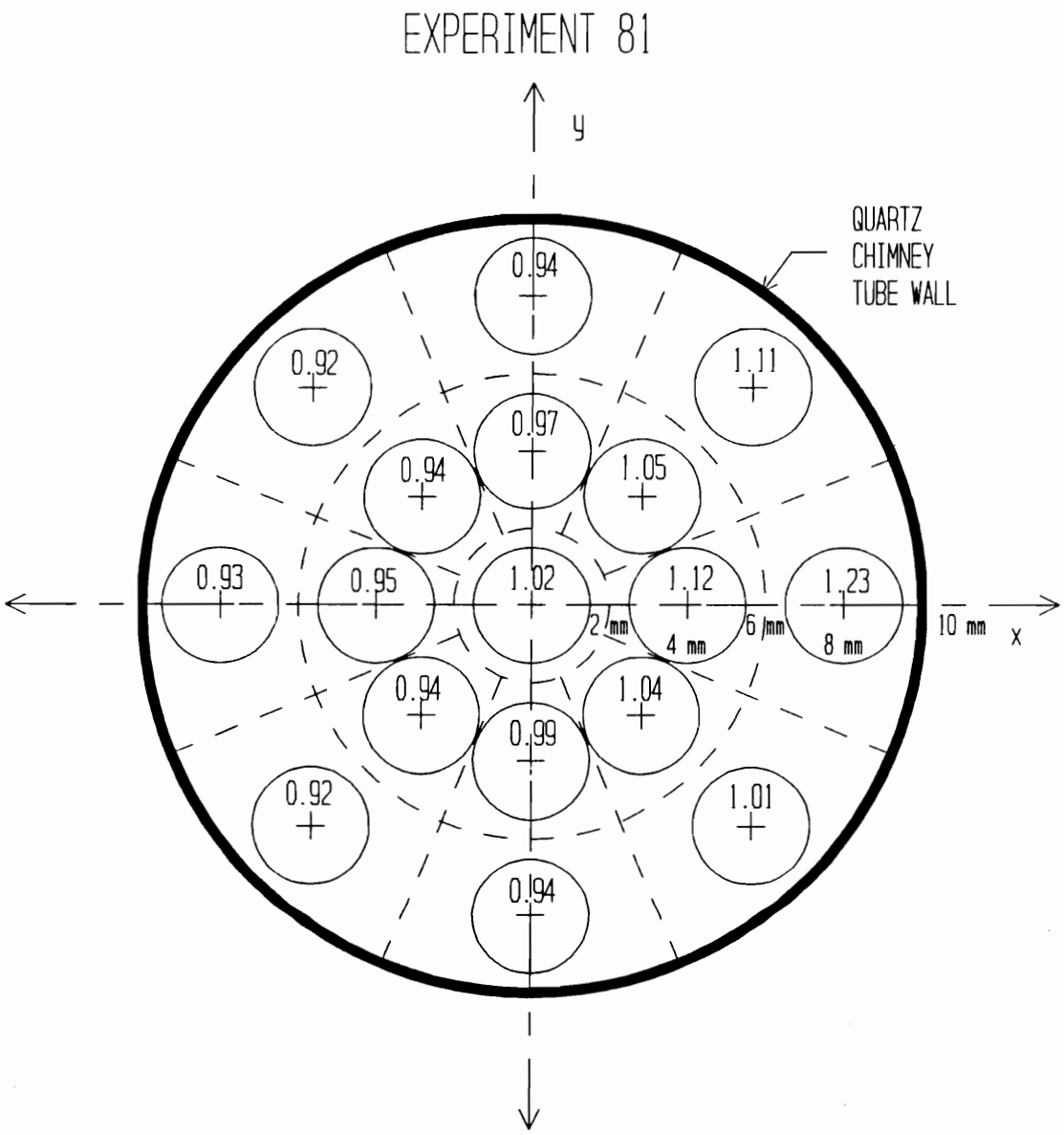

Figure 22 Spatial Equivalence Ratio Distribution for Experiment 81
$\bar{\phi} = 1.0, s = 0.08$

either the best or the worst uniformity, it is the flame with the largest surface area of rich mixtures. The leaner region on the left and the richer region on the right is observed for all of the spatially nonuniform flames, and it denotes a preference in the directivity of methane injection. The high equivalence ratio at the 3 o'clock position indicates that the jet sheet penetrates to the wall, although this cannot be known for certain since the probe measurements do not actually extend all the way to the wall. Figure 23 shows the equivalence ratio distribution for Experiment 82. The mean of the distribution is $\bar{\phi}$ = 0.79 and the unmixedness is 6 percent. This is one of the most uniform flames, yet it had very high NO_x emissions. Figure 24 shows the spatial equivalence ratio distribution for Experiment 83. The mean of the distribution is $\bar{\phi}$ = 0.86 and its unmixedness is 21 percent. This is the most nonuniform of the flames, and it had the highest NO_x emissions. Note also that although the mean equivalence ratio is lean, a significant region burns at stoichiometric and richer equivalence ratios. This is the only flame where the equivalence ratio at the origin is significantly different from the mean equivalence ratio (0.80, whereas $\bar{\phi}$ = 0.86). The difference between the mean equivalence ratio and the equivalence ratio at the origin is no greater than 0.02 for the other experiments. Figure 25 shows the spatial equivalence ratio distribution for Experiment 84. The mean of the distribution is $\bar{\phi}$ = 0.71 and its unmixedness is 6 percent. This flame had the lowest mean equivalence ratio and the most uniform distribution among these spatially nonuniform flames. It also had the lowest NO_x emissions, yet still more NO_x than steady, homogeneously premixed flames at the same

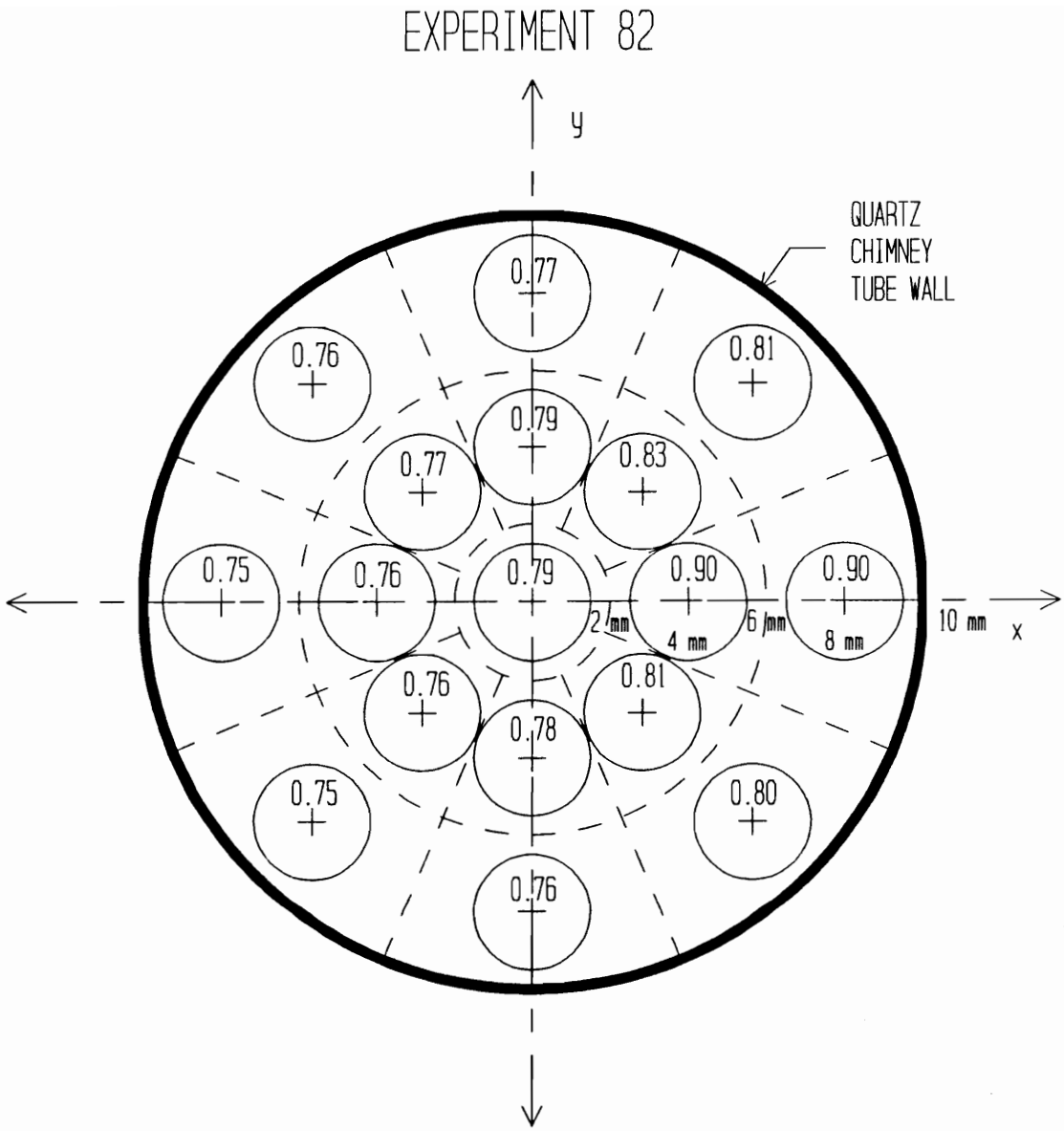

Figure 23 Spatial Equivalence Ratio Distribution for Experiment 82
$\phi = 0.79, \ s = 0.06$

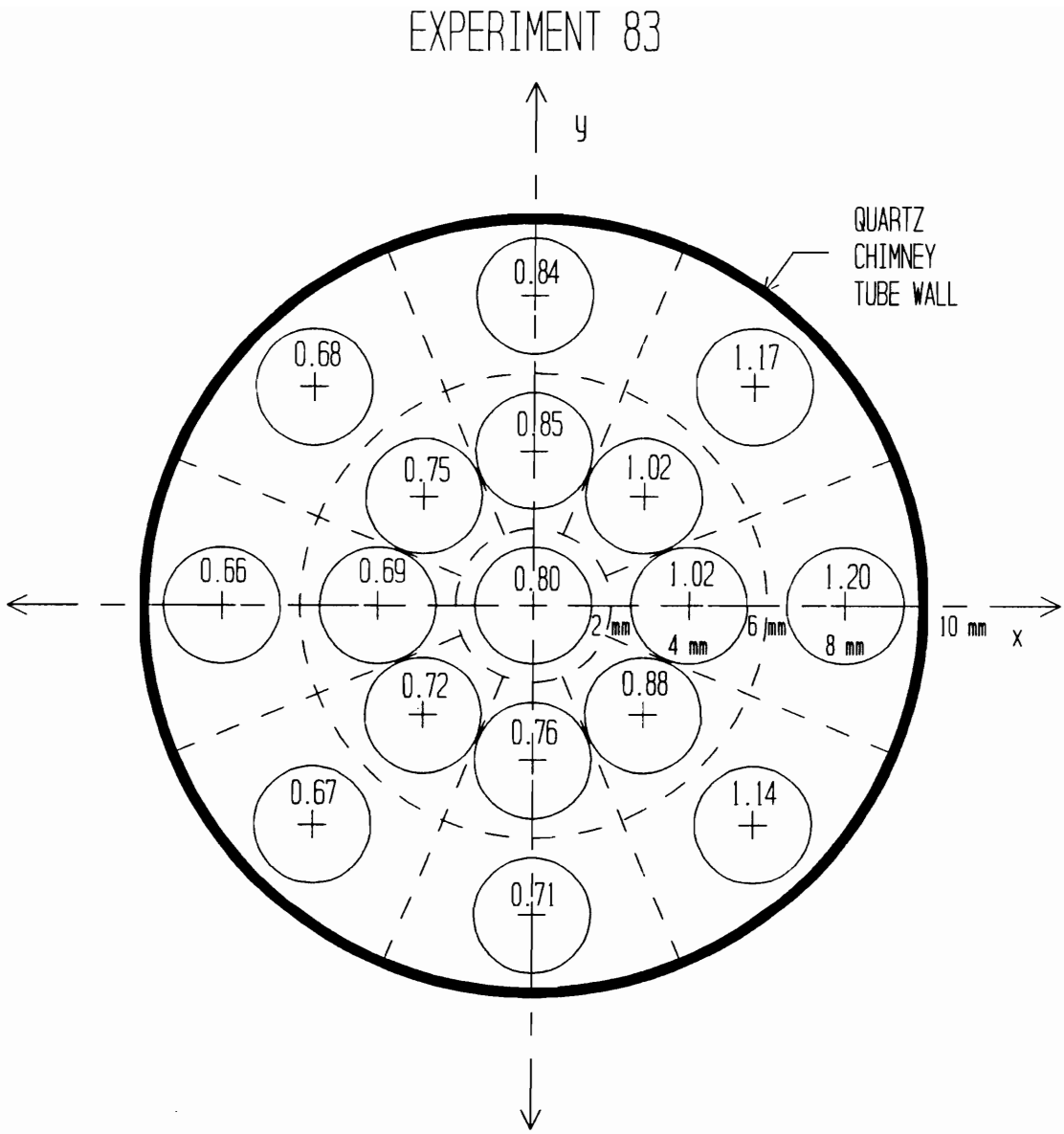

Figure 24 Spatial Equivalence Ratio Distribution for Experiment 83
$\phi = 0.86, \ s = 0.21$

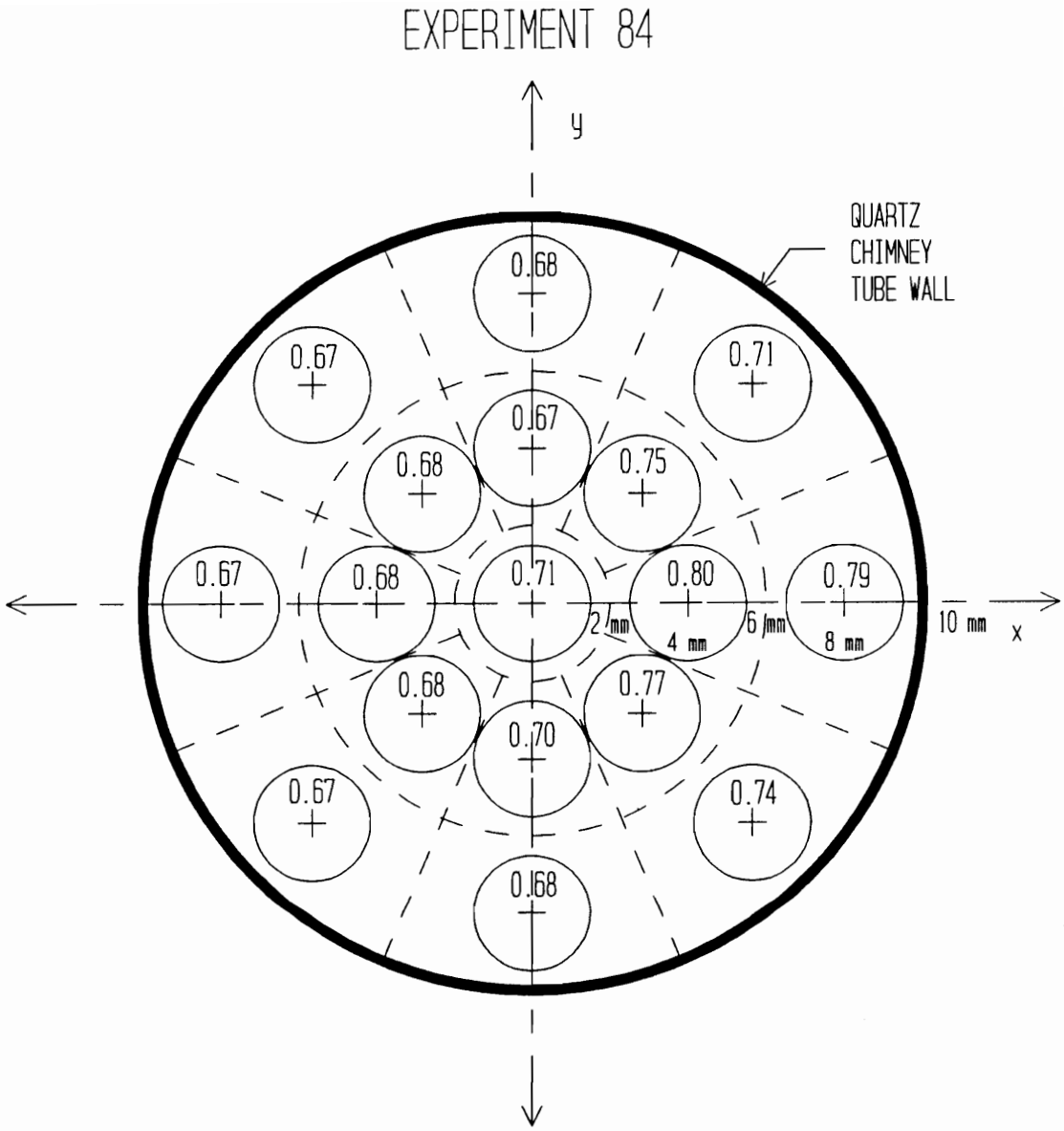

Figure 25 Spatial Equivalence Ratio Distribution for Experiment 84
$\bar{\phi} = 0.71, \; s = 0.06$

equivalence ratio or flame temperature. The richest zone indicates that preferential methane injection was still to the right, but the radial penetration of the jet was not high. Figure 26 shows the spatial equivalence ratio distribution for Experiment 87a. The mean of the distribution is $\bar{\phi} = 0.78$ and its unmixedness is 13 percent. While the mean equivalence ratio for this flame is very close to that of Experiment 82, this flame had lower NO_x emissions despite having twice the unmixedness. Compared to Experiment 82, it has leaner equivalence ratios which cover a larger proportion of the total flame area. Figure 27 shows the spatial equivalence ratio distribution for Experiment 87b. The mean of the distribution is 0.74 and its unmixedness is 10 percent. Both the mean and the unmixedness for this flame fall between those of Experiment 82 and Experiment 87a, but it produced more NO_x than either.

3.3.2 Comparison to Homogeneously Premixed Flames

Figure 28 compares the experimental measurements from the spatially nonuniform flames with the uniformly premixed steady flames. The dashed lines are curvefits through the spatially nonuniform flame data. These lines are used only to show trends; they are not used for modelling of the spatially-nonuniform data. Figure 28 (a) shows that the spatially nonuniform flames can have substantially higher or, in the case of Experiment 81, lower NO_x emissions than the steady flames at the same mean equivalence ratio. When the mean equivalence ratio is stoichiometric, the NO_x emissions

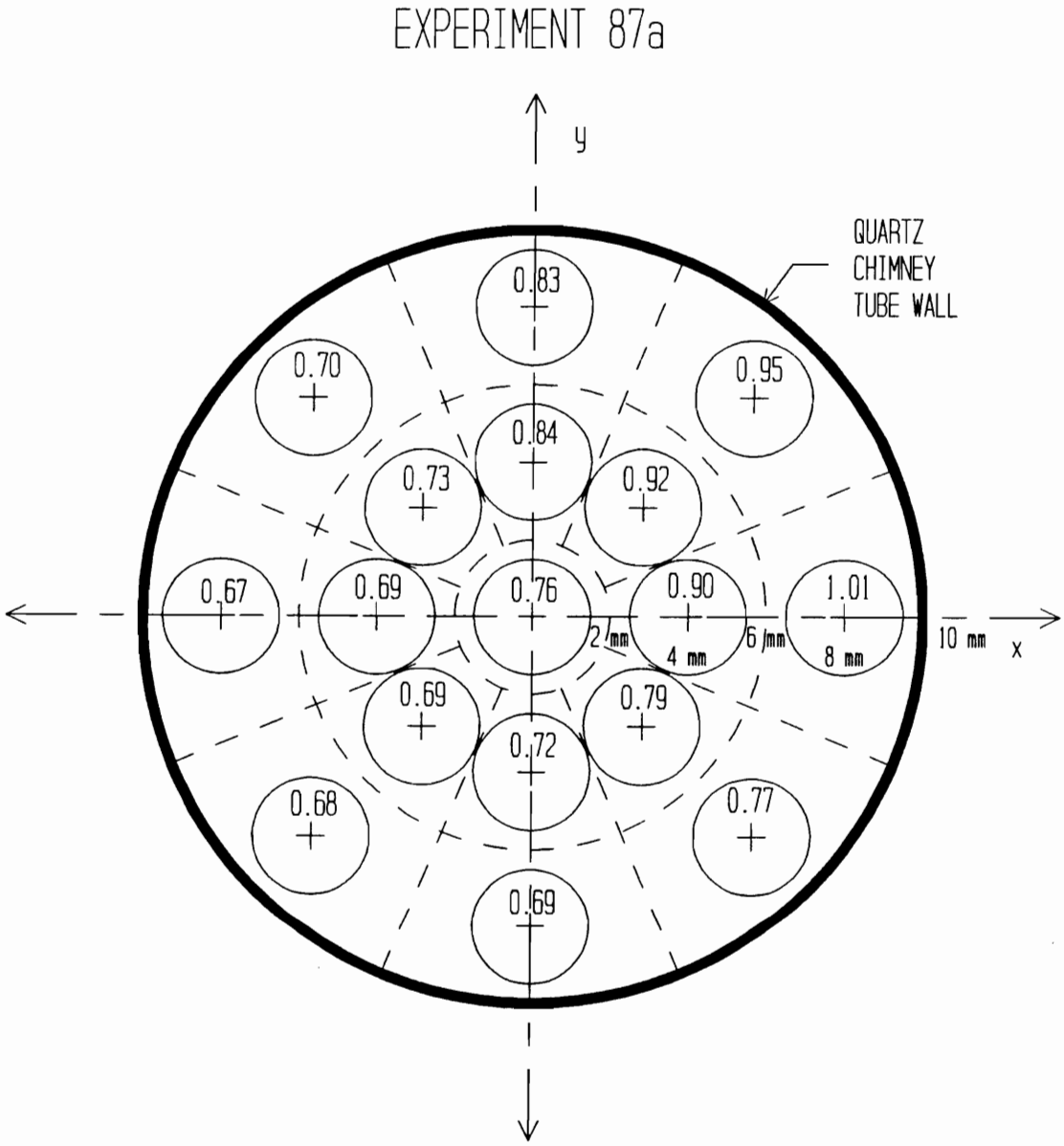

Figure 26 Spatial Equivalence Ratio Distribution for Experiment 87a
$\phi = 0.78, \ s = 0.13$

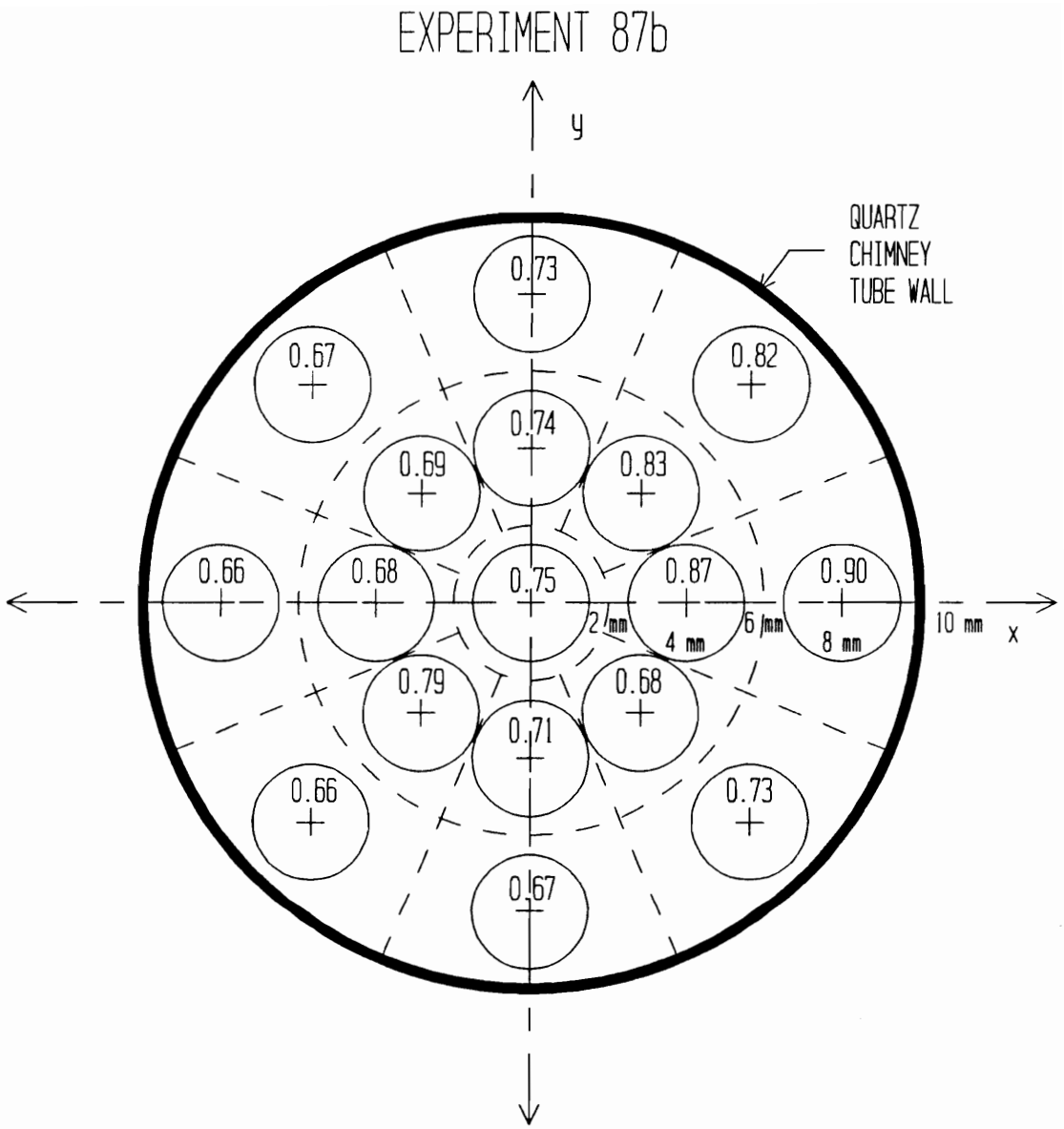

Figure 27 Spatial Equivalence Ratio Distribution for Experiment 87b
$\bar{\phi} = 0.74, \ s = 0.10$

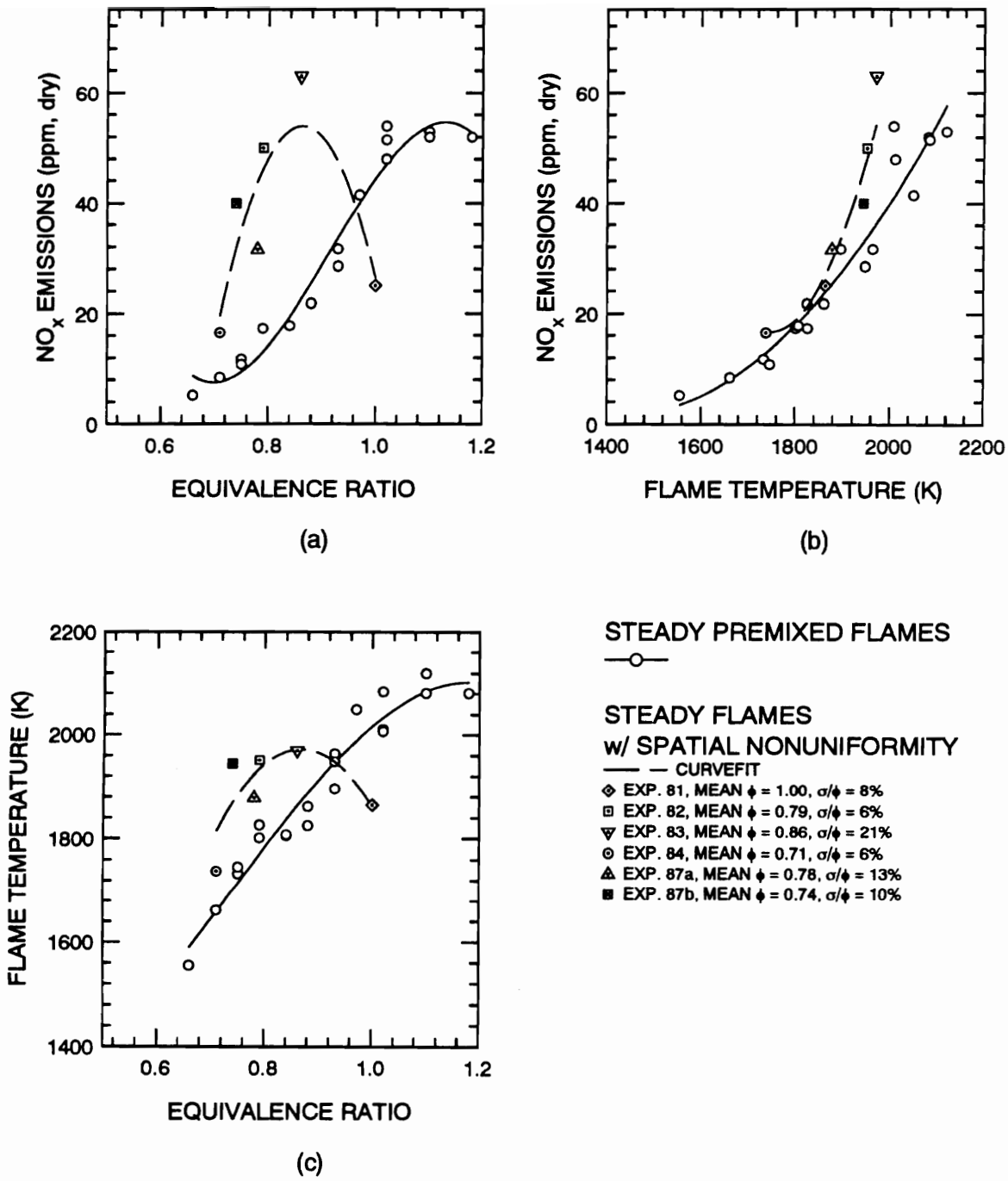

Figure 28 Comparison of Spatially Nonuniform Flame Measurements to Steady Flames

are lower for the spatially nonuniform flames. This agrees with the model proposed by Appleton and Heywood [12]. They surmised that deviations to either lean or rich equivalence ratios would both result in lower NO_x emissions, since the temperatures are lower as the flame deviates from stoichiometric. Whereas their model suggests that spatial nonuniformities should have more of an effect as the mean equivalence ratio goes leaner, this is not supported by the data in Figure 28. For instance, Appleton and Heywood's model predicts that the NO_x emissions for Experiment 82 should be closer to the steady flame emissions than the NO_x emissions of Experiment 84. Both cases have the same unmixedness (six percent), but the leaner flame is expected to deviate more strongly from the steady flame emissions. While the presence of some spatial nonuniformity increases NO_x emissions and the case with the greatest unmixedness has the highest NO_x emissions, the NO_x emissions do not correlate well with the unmixedness overall.

Figure 29 shows the variation of nondimensionalized NO_x with the unmixedness parameter s. The nondimensionalized NO_x is defined by

$$\frac{NO_{X\ nonuniform} - NO_{X\ uniform}}{NO_{X\ uniform}} ,$$

where $NO_{X\ uniform}$ comes from the steady flame data at the same mean temperature using equation (18). The spread of the data illustrates the difficulty in correlating NO_x

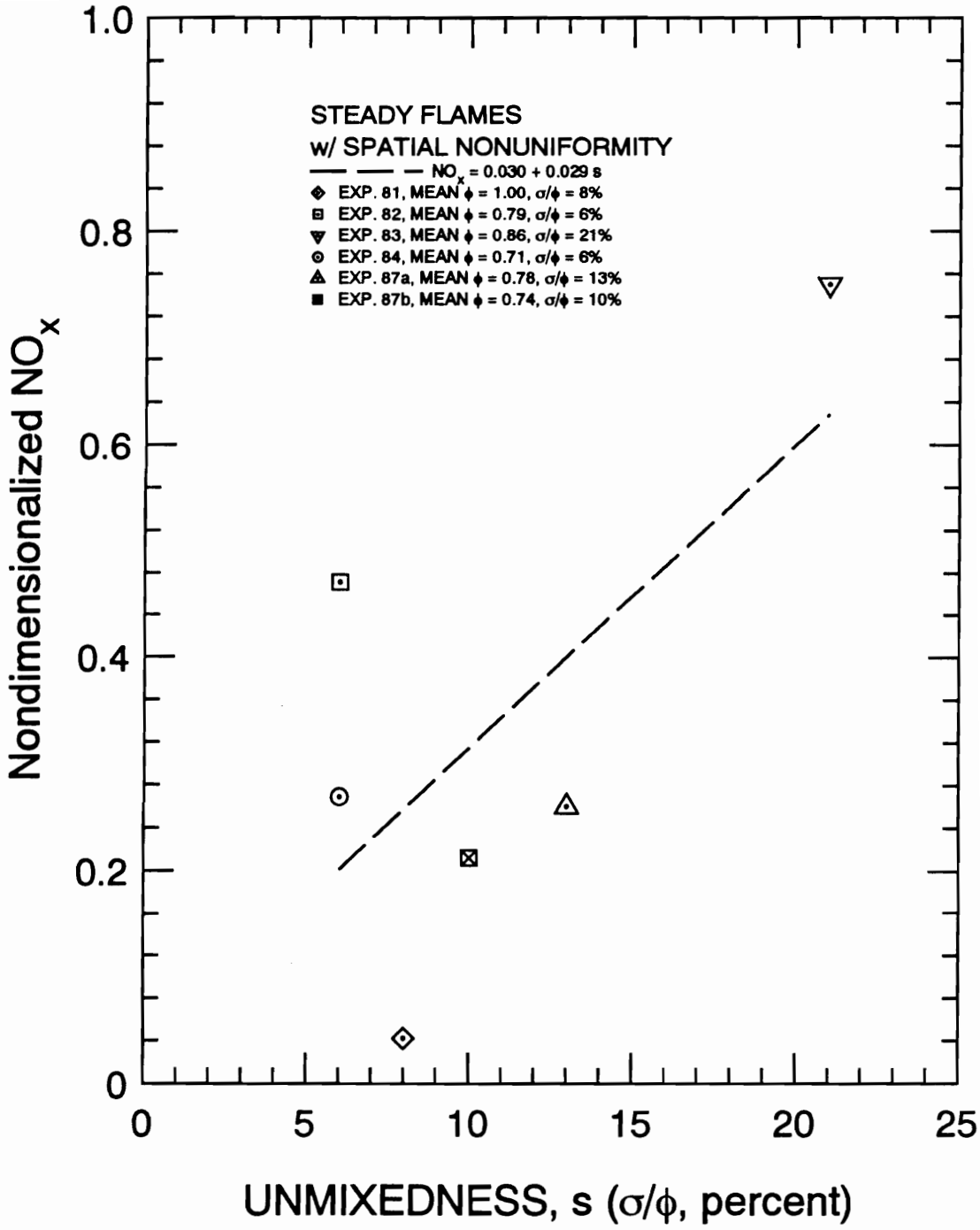

Figure 29 Variation of Nondimensionalized NO_x Emissions with Spatial Unmixedness

emissions to the unmixedness parameter alone. For instance, Experiment 82 had only half the unmixedness of Experiment 87a, yet it produced twice the increase in NO_x emissions with respect to the steady flames.

Figure 28 (b) shows that the NO_x emissions increase as the mean flame temperature increases. However, in some experiments the NO_x emissions are higher for the nonuniform flames than for the uniformly premixed flames. This is especially true as the mean flame temperature increases. The increased effect of the nonuniformities could be due to the higher slope and curvature of equation (18) in this region.

Figure 28 (c) shows that the temperature-versus-equivalence ratio relationship is different for the spatially nonuniform flames. For most of the experiments, the flame temperature is higher in the spatially nonuniform flames for the same equivalence ratio. The exception is Experiment 81, at a stoichiometric mean equivalence ratio. At first glance, these data would seem to explain Figure 28 (a) perfectly; the increase in NO_x for the spatially nonuniform flames is due to the higher mean flame temperatures. While this is partly true, the effect of the spatial nonuniformity is also significant. For example, the emissions for Experiment 83 are the highest for all flames, yet this flame did not have the highest temperature. Figure 28 (b) indicates that both Experiments 82 and 83 have significantly higher NO_x emissions than their mean flame temperatures would suggest. Why is the temperature-versus-equivalence ratio behavior of the spatially

nonuniform flames different than the steady flames? One explanation is that the spatial distribution of the flame temperature is expected to vary along with the equivalence ratio distribution, and the different gradients of temperature at the walls of the quartz tube will change the heat transfer to the burner. The insulation should minimize this effect, however. Another source of difference could be an error in the temperature measurement procedure. Spatial resolution of the flame temperatures was not obtained, and the thermocouple probe was placed at the center of the flame for a single measurement. While the equivalence ratio measured at the center of the flameholder usually differed only negligibly from the mean equivalence ratio, the temperature measurement might not have been an accurate estimate of the mean flame temperature. Due to the spatial nonuniformity, heat and radical species could diffuse radially across the flame and change the temperature at the axis. A final possible source of error could be biasing error due to the location of the sampling points or the weighting of the data. However, no reasonable weighting factor distribution is sufficient to shift the estimated mean equivalence ratios into agreement with the steady flame data. Both temperature measurement errors and probe biasing errors are considered further in Section 4.1. The analysis shows that biasing error can account for the unusual behavior of the spatially nonuniform flames, with certain assumptions.

3.4 PULSING FLAMES

Table 4 lists the experimental conditions for the unsteady flames. The mean flame temperatures were measured with the large thermocouple and the NO_x measurements were obtained from probe sampling. The mean equivalence ratio is calculated from the optical measurements. The quantity ϕ_{min} is the average minimum equivalence ratio fluctuation and ϕ_{max} is the average maximum equivalence ratio fluctuation. The difference between ϕ_{max} and ϕ_{min} is an estimate of the amplitude of the fluctuations. Figure 32 in section 4.2.1 shows typical equivalence ratio fluctuations. The frequency reported in the last column of Table 4 is the *fundamental* frequency of the equivalence ratio fluctuations. Since the waveforms are not sinusoidal, other frequency components are present. However, the fundamental frequency is the strongest component and it most closely represents the period of the methane injection. The set of pulsing flames covers a range of mean equivalence ratios between 0.65 and 0.93. Although the amplitude of the equivalence ratio fluctuations appears to be relatively constant at about 0.40, this results in a wide range of amplitudes of temperature fluctuation due to the nonlinear dependence of the flame temperature on the equivalence ratio. Each of these tests required a full day's experimentation, and the set represents a sufficient sampling of pulsing flame conditions.

Table 4 Unsteady (Pulsing) Flames

Experiment Number	Mean Flame Temperature (K)	NO_x (ppm, dry)	$\bar{\phi}$	ϕ_{min} ϕ_{max}	$\phi_{max} - \phi_{min}$	Pulse Freq. (Hz)
70	1710	20	0.66	0.49 0.88	0.39	2.25
76	1841	32	0.93	0.77 1.1	0.33	3.75
77	1781	25	0.86	0.58 1.0	0.42	3.75
78	1667	20	0.65	0.44 1.0	0.56	2.75
80	-	-	0.76	0.67 0.81	0.14	3.75

Experiment 80 was different from the other flames. In this experiment, the spatial distribution of equivalence ratio was measured with the probe and the total hydrocarbon analyzer, but the temperatures and NO_x emissions were not measured. The mean equivalence ratio was calculated from the seventeen probe measurements. The values of ϕ_{min} and ϕ_{max} represent the minimum and the maximum of the probe measurements. The unmixedness s for this case is six percent. Figure 30 shows the spatial equivalence ratio distribution for Experiment 80. The uniformity of methane distribution for this pulsing flame was as good as or better than the uniformity of the spatially nonuniform flames. Note that the tendency for preferential methane injection to the right is significantly less in this case than in the steady flow, spatially nonuniform cases. The equivalence ratio of the homogeneously premixed gases was only 0.28, so the injected pure methane has penetrated in all directions. (Note the minimum equivalence ratio of 0.67; the increase of $\Delta\phi = 0.39$ is due to mixing with the injected pure methane.) As the injector is agitated the position of the nose cone can change randomly, for there is clearance in the fit. Also, the injector is allowed to open fully, so that unidirectional methane injection is less likely than for the spatially nonuniform flame tests. It seems reasonable to assume that the spatial uniformity would be similar for the other pulsing flames.

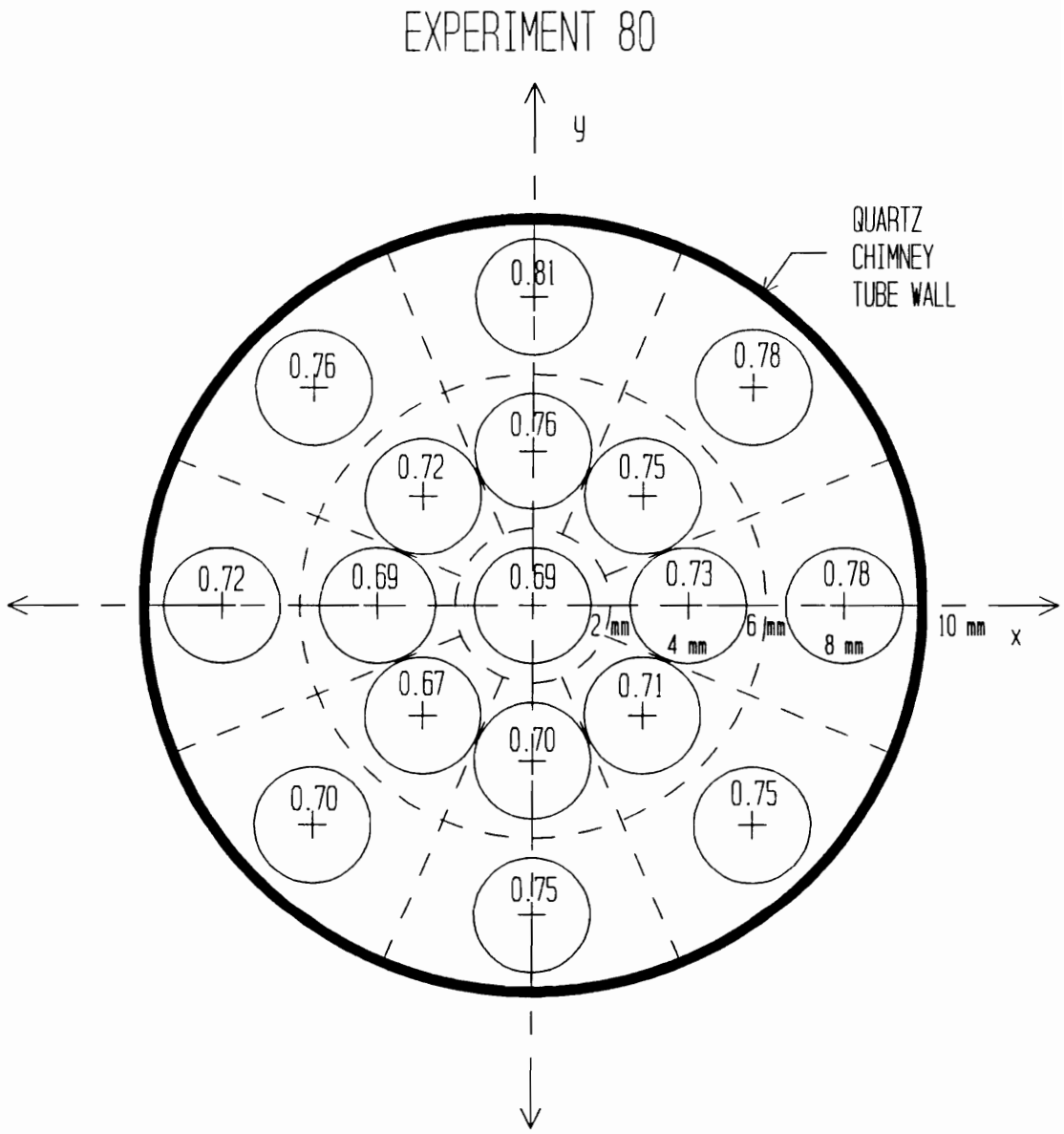

Figure 30 Spatial Equivalence Ratio Distribution for Experiment 80
$\bar{\phi} = 0.76, \; s = 0.06$

3.4.1 Temperature Trends

Figure 31 shows axial temperature profiles from unsteady flame temperature measurements. The ×'s show the mean temperature measurements using the large thermocouple, corrected for losses. The solid line is a linear fit to these data. The filled circles show the mean temperatures measured with the fine thermocouple. Note that the measurements do not go all the way to the flame zone itself due to the fragility of the thermocouple. The triangles represent the temperature extremes, the maximum and minimum temperatures measured with the fine thermocouple. The dashed lines are linear curvefits to the maximum and the minimum temperatures. Note that a difference exists between the mean temperatures measured with the large and the fine thermocouples. Although errors in the temperature correction terms could be responsible, the mean temperature difference is generally larger than the magnitude of the fine thermocouple correction terms. Catalytic heating of the fine thermocouple is the most credible explanation, particularly since the maximum measured temperatures for Experiments 70 and 78 are higher than the adiabatic flame temperatures for those flames.

Figure 31 (d) indicates a poor correlation between the minimum temperatures and the dotted line used to represent them. As the flameholder is approached, the minimum temperature plummets. Experiment 78 has the leanest fluctuations in equivalence ratio among the unsteady flames, and it is likely that this particular flame was not stable on

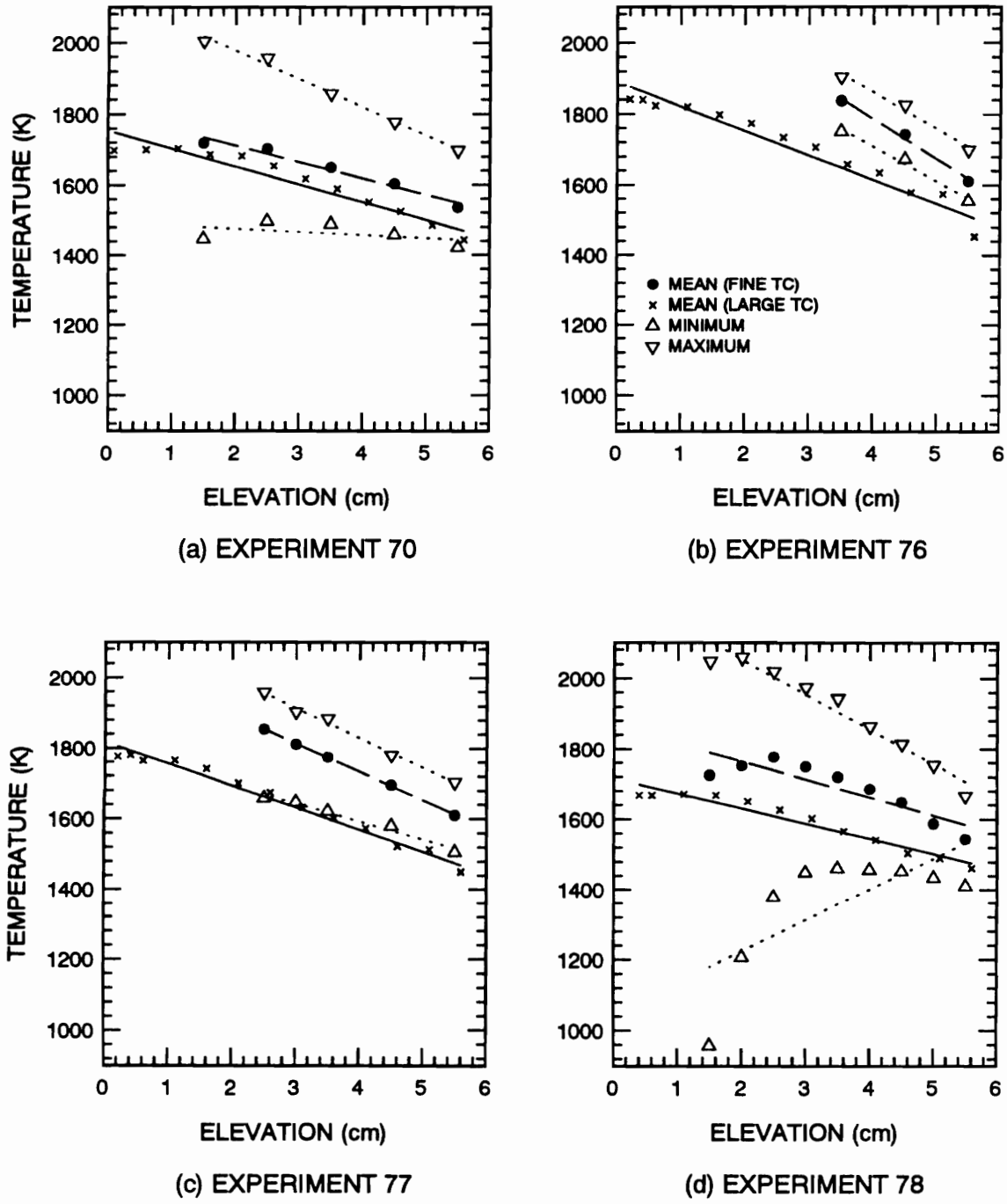

Figure 31 Axial Temperature Profiles in the Pulsing Flames

the flameholder. The flame could have been lifting off of the flameholder with each lean extreme, and the flame could have passed back and forth over the thermocouple. Since there are doubts about this flame's stability, further analysis of temperature records and modeling of the pulsing flames in Chapter 4 is limited to the data from Experiments 70, 76, and 77. However, Experiment 78 data are still used for comparisons between mean equivalence ratio, mean temperature, and NO_x emissions.

For these unsteady flames, the mean temperatures are known down to the flame itself, and the fluctuating temperatures are known down to some point within 0.5 to 3.5 cm of the flame zone. The fluctuating temperature of the flame itself is estimated using these data, following a procedure described in Chapter 4.

3.4.2 Equivalence Ratio Fluctuations

Figure 32 shows the fluctuations in equivalence ratio for the unsteady flames. These measurements were obtained with the optical system, and the equivalence ratio was calculated using equation (15). The dot-dash lines show the average minimum and the average maximum equivalence ratio fluctuations. Figure 32 (a) shows that although Experiment 70 had the lowest methane injection frequency, the signal appears noisier than the other cases and appears to contain higher frequency components. Figure 32 (b) shows that although Experiment 76 has a lean mean equivalence ratio, the excursions to

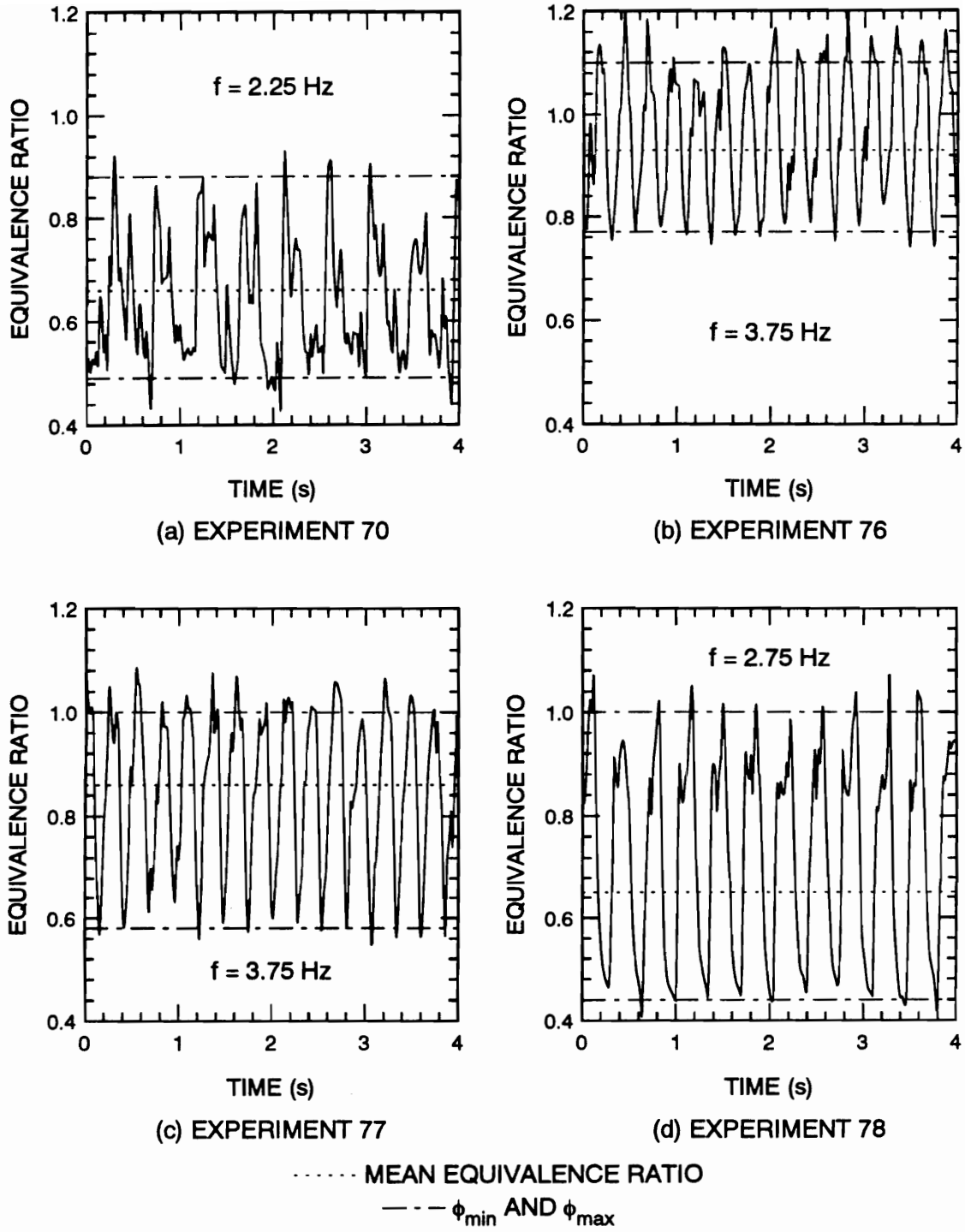

Figure 32 Equivalence Ratio Fluctuations for the Pulsing Flames

the rich regime are strong and frequent. Figure 32 (d) shows the very low excursions in equivalence ratio that led to the flame instability in Experiment 78. While the excursions for Experiment 70 are also very low, these events are more brief and less frequent than in Experiment 78. All of the records show very strong equivalence ratio fluctuations, extending across an equivalence ratio range of $\pm$ 0.20. Note also that the amplitude of the fluctuations about the mean are not always symmetric, with Experiment 77 showing stronger lean fluctuations and Experiment 78 showing stronger rich fluctuations.

3.4.3 Comparison to Other Flames

Figure 33 compares the data from all three flame types. The pulsing flame data are represented by the solid symbols and the dotted curve. While the NO_x emissions and flame temperatures were measured using the same techniques for all three flame types, the equivalence ratio measurement techniques varied. For the steady flames, the equivalence ratio comes from the rotameter readings. For the spatially nonuniform flames, the mean is the weighted average of all of the spatial probe measurements. For the pulsing flames, the mean comes from the optical measurements. The optical technique arguably has the greatest potential error of the three equivalence ratio measurements.

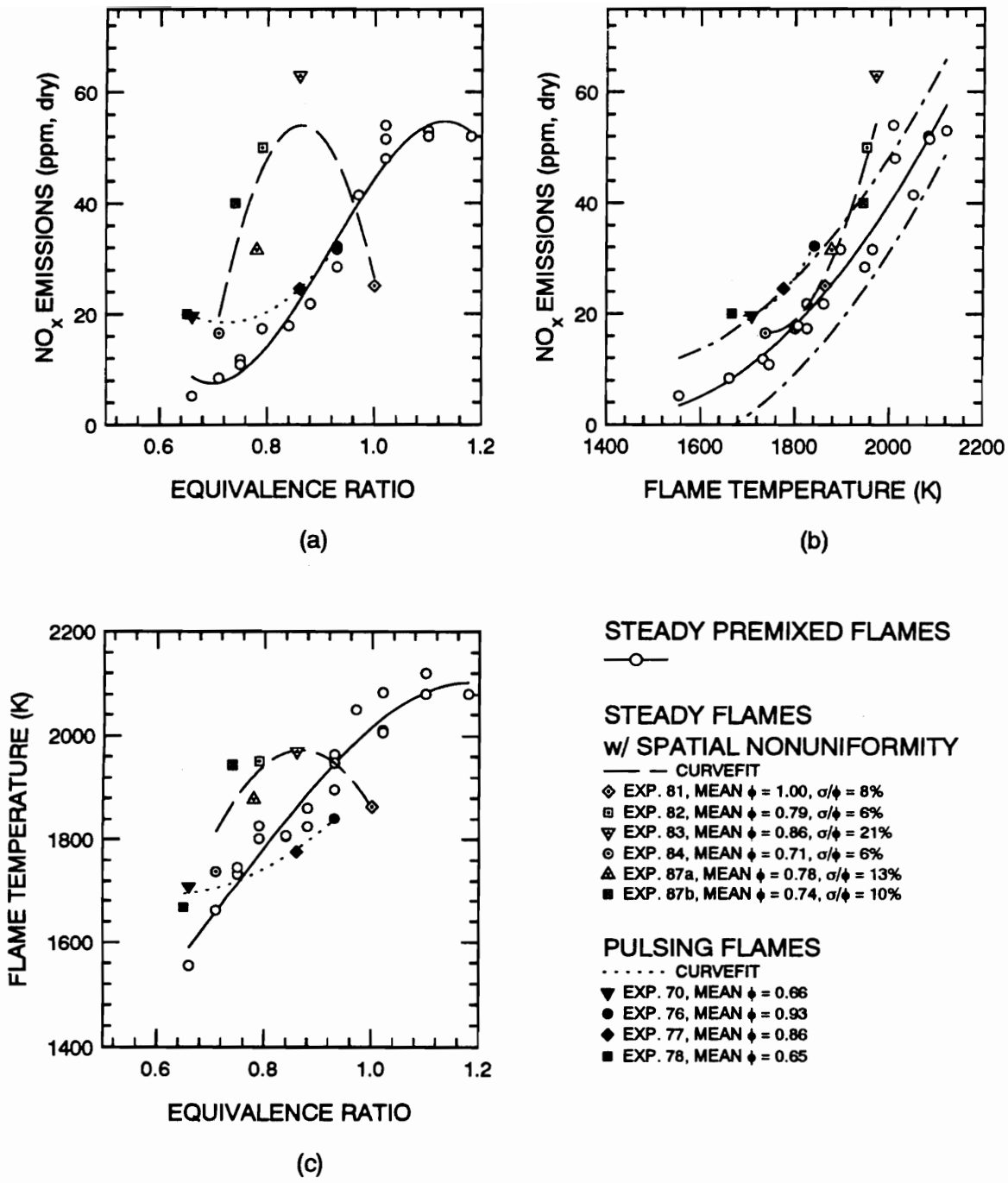

Figure 33 Comparison of Experimental Measurements from Pulsing, Spatially Nonuniform, and Steady Flames

Figure 33 (a) compares the variation in NO_x emissions with mean equivalence ratio for the different types of the flame. The figure shows that the lean limit of $\bar{\phi}$ = 0.66 applies to all three types of flame. Figure 33 (a) shows that the pulsing flames produce as much (Experiments 76 and 77) or much more NO_x (Experiments 70 and 78) than the steady flames at the same mean equivalence ratio. Near the lean flammability limit, the pulsing flames produce more NO_x than the spatially nonuniform flames. For these two leanest pulsing flames, the NO_x emissions are higher than one would expect based on their mean equivalence ratio, but they are also hotter flames than expected as well. Experiments 76 and 77 are unusual in that even though they have lower mean flame temperatures, they still produce as much NO_x as the steady flames. However, the spatially nonuniform flames also produce significantly more NO_x in this equivalence ratio range.

Figure 33 (b) compares the two most relevant measurements, temperature and NO_x emissions. Since the results shown by this figure are particularly important, Figure 33 (b) has been enlarged as Figure 34. For this figure, the 95 percent confidence intervals for the steady flame curvefit have been plotted as dot-dashed lines. Although the intervals appear to be wider at low equivalence ratios, this is an optical illusion. The vertical displacement of the curves is a constant 2σ. If anything, the confidence intervals should be narrower at low equivalence ratios since the spread of the data is less there. All of the flames show that the NO_x yield of the flame increases with the temperature.

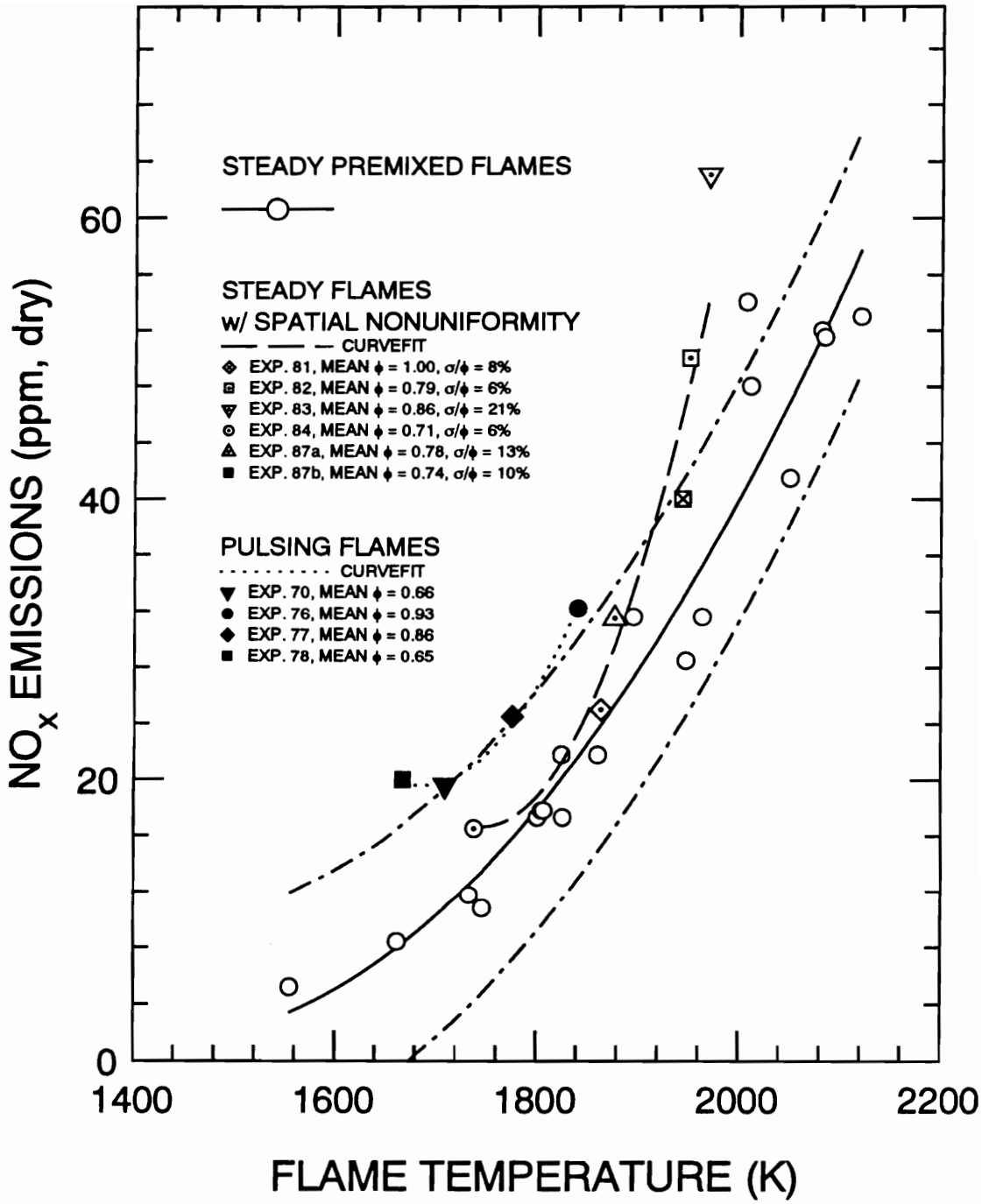

Figure 34 Comparison of Experimental Measurements from Pulsing, Spatially Nonuniform, and Steady Flames. Detail of NO_x Emissions as a Function of Flame Temperature

All of the pulsing flames produce more NO_x than a steady flame at the same mean flame temperature, and all of the spatially nonuniform flames produce as much or more NO_x than a steady uniform flame at the same flame temperature. The spatially nonuniform flame data indicate that the effect of the nonuniformity increases as the mean flame temperature increases. The NO_x emissions for Experiments 82 and 83 fall outside the upper 95 percent confidence limits for the steady flames, showing that their NO_x emissions are different at the five percent significance level. The effect of spatial equivalence ratio nonuniformities appears to be less than the effect of the temporal fluctuations in the pulsing flames. All of the pulsing flame NO_x emissions fall outside the upper 95 percent confidence interval for the steady flames. The higher NO_x emissions for the pulsing flames than for the spatially nonuniform flames and the steady flames at the same mean flame temperature shows that temporal effects can be significant contributors to NO_x in premixed flames.

Figure 33 (c) shows that the flame temperature as a function of the mean equivalence ratio is different for the three types of flames. The deviations from the steady flame behavior are smaller for the pulsing flames than for the spatially nonuniform flames. For Experiments 76 and 77, it is tempting to explain the lower flame temperatures for their equivalence ratio by citing research on pulse combustors. Commercial pulse combustors have intentional acoustic instabilities and velocity fluctuations in the post-flame gases [53]. The velocity fluctuations enhance convective

heat transfer to the burner, lowering the temperature of the post-flame gases and therefore reducing NO_x emissions as well. However, the differences between the burner in this experiment and a commercial pulse combustor are significant. The current burner is not driven by acoustic instabilities, and the fundamental frequency of its fluctuations is much lower. Whereas the pulse injection frequencies are less than 10 Hz, the frequency of the first longitudinal mode for this burner is about 4000 Hz. Additionally, the exhaust gases of commercial pulse combustors frequently premix with the fresh reactants, and this also inhibits NO_x production (similar to the exhaust gas recirculation technique employed in automobile engines). Mixing of the fresh and post-flame gases does not seem possible in this burner. Although increased heat transfer due to fluctuations is possible in both types of burner, it is unlikely to have as significant an effect on the well-insulated flame zone of the burner used in this experiment. Furthermore, this would not explain why Figure 33 (b) shows higher NO_x emissions for the pulsing flames at the same flame temperature as a steady flame.

As for Experiments 70 and 78, the higher flame temperatures near the lean flammability limit are inconsistent with the pulse combustor analogy. Near the lean flammability limit, equivalence ratio fluctuations could have a stabilizing or a destabilizing effect on the flame. While the lean fluctuations are destabilizing, the rich fluctuations would be stabilizing. The steady flames at the lean flammability limit have no such equivalence ratio fluctuations. The rich excursions of the pulsing flame may

possibly increase the mean temperature of the flame, especially if the fluctuations of equivalence ratio are not symmetric about the mean. Figure 32 shows that this is the case for the pulsing flames. Figure 33 (c) points out that the burner properties could be affecting the three types of flames differently; changes in the heat transfer, wall effects, or flame stabilization could lead to the observed differences in flame temperature for a given equivalence ratio. Since NO_x emissions are primarily driven by temperature rather than equivalence ratio in the lean regime, the results shown by Figure 33 (b) are the relevant ones for this experiment.

CHAPTER 4

DISCUSSION AND INTERPRETATION OF RESULTS

Although Figure 33 (b) illustrates the difference between steady flames, spatially nonuniform flames, and pulsing flames, it does little to explain why these differences exist. The pulsing flames have both temporal fluctuations and some spatial nonuniformities, and the experimental approach makes it difficult to unambiguously separate the two. Empirical modeling of the flames reported in this chapter attempts to explain the relative influence of the spatial and temporal effects in the pulsing flames. One model describes the effect of spatial equivalence ratio nonuniformity on NO_x emissions. A second model describes the effect of temporal equivalence ratio fluctuations on NO_x emissions. These models are empirical in that they use the data from the uniform steady flame experiments to predict the behavior of the spatially nonuniform and the pulsing flames. Thus, for the temporal fluctuations, it is assumed that at some instantaneous temperature the instantaneous NO_x production is the same as for a steady flame at that temperature. For the spatial nonuniformities, the model assumes that each area of flame surface produces NO_x in accordance with its local

equivalence ratio. The effects are integrated, spatially or temporally, to predict the overall NO_x emissions. The predicted NO_x is then compared to the measured NO_x.

4.1 EMPIRICAL MODEL USING EQUIVALENCE RATIO DISTRIBUTIONS

The first model uses the data from the spatially nonuniform flames to predict the effect of the spatial equivalence ratio distribution on NO_x emissions. The equivalence ratio was probe sampled at seventeen sites over the flameholder, and the NO_x emissions expected from each local area are estimated using the $NO_x(\phi)$ correlation (equation (16)) for the steady flames. The weighted average of these seventeen local NO_x estimates gives the estimated overall NO_x emissions,

$$\overline{NO_x} = \frac{1}{A} \sum_{i=1}^{17} NO_x(\phi_i)\, A_i \quad .$$

Another approach is possible. The local temperature of each zone can be estimated with the $T(\phi)$ correlation (equation (20)), and then the local NO_x production can be estimated with the $NO_x(T)$ correlation (equation (18)). However, the differences between this approach and the $NO_x(\phi)$ approach are negligible. The NO_x production of

each zone differs by less than 4 ppm, and the averaged NO_x production differs by less than 2 ppm.

Figure 7 shows that the sampling pattern can be divided into nine interior zones of π mm^2 and eight exterior zones of 2π mm^2 each. This implies that each of the eight exterior measurements should be weighted twice as much as each of the interior measurements. Other possibilities exist, however. Due to heat transfer at the walls, the outer zones are cooled and might produce less NO_x per unit area than the interior zones. Also, the flameholder is located about four tube diameters downstream of the premixed gas injection point, so that the flow is in transition between plug flow and fully developed flow. This suggests that perhaps the zones should be weighted by mass flow rate. However, neither of these concepts were adopted and the weighting factors are based simply on the surface area of each zone.

Figure 35 shows the original data and the results of the model. Figure 35 (a) shows that the NO_x predicted for the spatially nonuniform flames (dotted line) does not vary significantly from the experimental data for the uniform steady flames (solid line). The dot-dashed curve shows the estimated NO_x production from the richest zone of each flame; that is, it shows the expected NO_x emissions if the measurements were made directly over the highest-yielding part of the flame. This NO_x estimate agrees better with the experimental results for spatially nonuniform flames (dashed line), but it is certainly

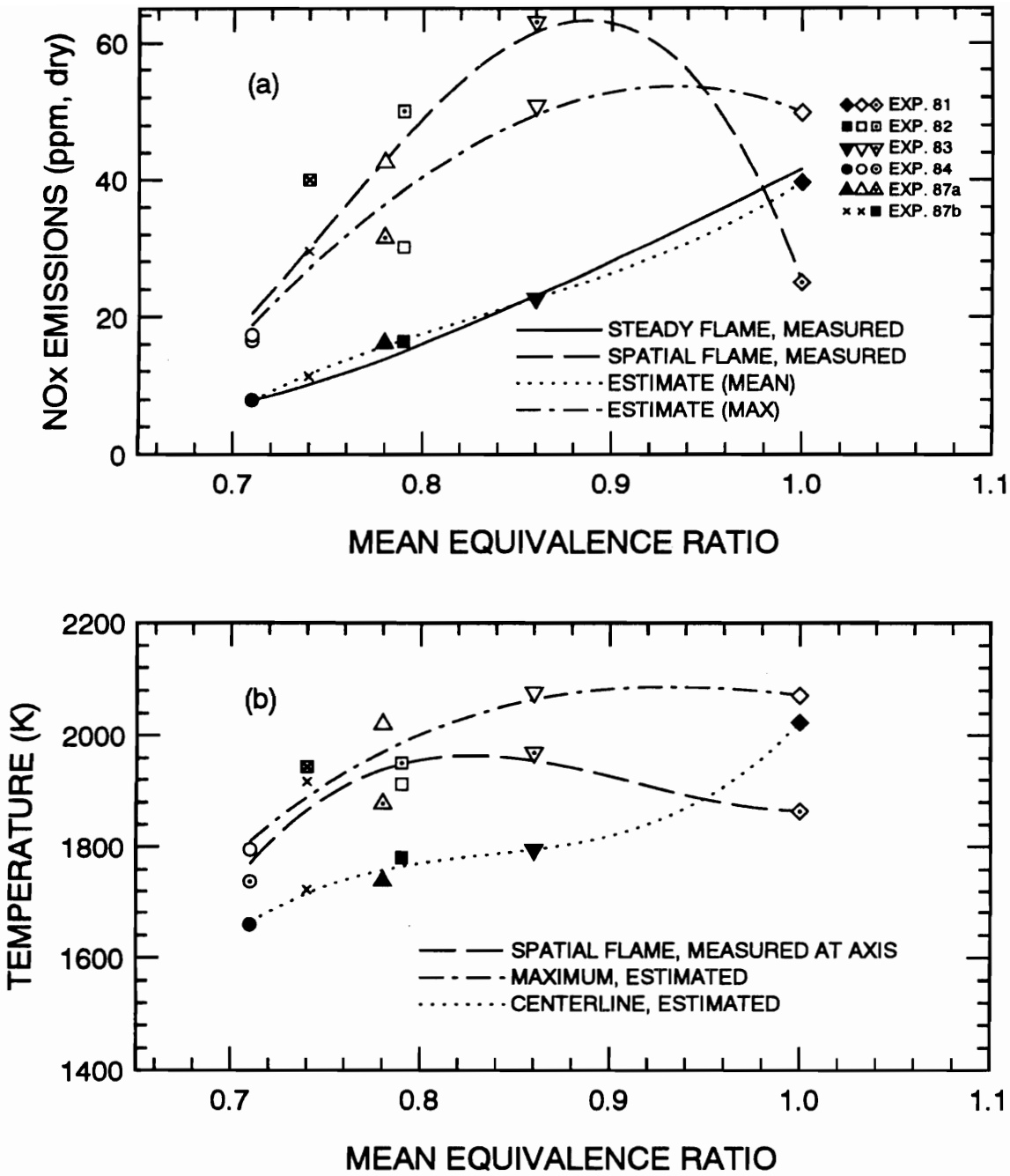

Figure 35 Results of Model for Spatial Nonuniformity of Equivalence Ratio

less intuitively pleasing than the weighted-average model. Note that in several cases the measured NO_x is still greater than either of the NO_x estimates. The sample flow rates for the NO_x measurements were sufficiently high that spatially resolved measurements were not possible, and the NO_x emissions from hotter and cooler regions were mixed.

This model is based on the assumption that spatial *temperature* variations are the cause of higher NO_x emissions, and that the temperature variations correlate with the measured local equivalence ratios. However, Figure 33 (c) shows that the correlations between axial flame temperature and mean equivalence ratio are not similar for the spatially nonuniform and the steady flames. Spatially-resolved temperature measurements may have helped explain these differences. Unfortunately, spatially-resolved temperature measurements across the flame surface were not obtained. One hindrance was the size of the thermocouple probe in relation to the burner. The lead wires extended 1.5 mm to each side of the thermocouple junction, and this interfered with getting measurements close to the walls. Also, the temperature rise caused by immersing the probe in the burner for a length of time made it difficult to take repeated measurements without changing the burner temperature. The experiments were very complex and time-consuming without such measurements, and the desirability of spatial temperature measurements was not recognized initially.

In the spatially nonuniform flames, the temperature measurement was at the axis of the burner, and in all but one case the centerline equivalence ratio was not greatly different from the mean equivalence ratio. One might then expect that the temperature measurement is an accurate indicator of the mean flame temperature. Figure 35 (b) compares the measured mean flame temperature (open symbols with dots) with the estimated temperatures based on the equivalence ratio measurements and $T(\phi)$ from equation (20) (filled symbols). The dotted line represents the estimated flame temperature for the centermost zone of the flame, at the burner axis. This is where the thermocouple measurement actually occurred. The dot-dashed line represents the estimated temperature of the hottest flame zone, regardless of its location. The dashed line shows the measured flame temperature. Clearly, a difference exists between the centerline estimate and the experimental measurements. This difference could explain why the previous model's predictions were unable to match the experimental measurements. The measured temperatures were not greater than the estimated maximum temperature for the flame (for the two cases where the measurement is slightly greater, the differences are within expected experimental error). This would suggest that the spatially-nonuniform flames are strongly dominated by the hottest region of the flame, which makes sense based on the nonlinear effect of temperature on NO_x production. Or, perhaps, the uniform flame data are not a good basis for modeling these spatially nonuniform flames. The diffusion of heat and chemical species across the flame surface could account for some part of the differences between the uniform and spatially-

nonuniform flames. Furthermore, tight spatial clearances within the burner accentuate the effect of the quartz walls on the flames, where the spatial nonuniformities necessarily approach the walls. For the pulsing flames the equivalence ratio uniformity is better, and the walls are expected to have less of an effect.

Figure 28 and Figure 35 together indicate that the spatially nonuniform flames cannot be well characterized by the experimental measurements. The following discussion proposes an explanation for this behavior and corrects some of the data. The source of the problem is a bias in the mean equivalence ratio calculated using the probe sampling measurements.

Figure 22 through Figure 27 show the spatial equivalence ratio distributions for the spatially-nonuniform steady flames. In each of these figures, the equivalence ratio of the leanest region matches the equivalence ratio of the premixed gases entering the burner. This is the minimum possible equivalence ratio for each case, since the injected methane can only increase the richness of the mixture where the jet sheet penetrates. Note that in these figures, the probe measurements do not extend to the walls of the quartz chimney tube, and the lean region dominates the left-hand zones of each equivalence ratio distribution. It is very likely that the minimum equivalence ratio extends to left-side walls of the quartz tube, where the methane jet did not penetrate. Since the methane concentration gradients are mild in these zones, the probe

measurement is a reasonable estimate of the mean equivalence ratio for these zones. However, a quite different situation exists on the right-hand side of the figures, since the pure methane tends to penetrate preferentially to the right. Note that in all cases except Experiment 84, the richest measured equivalence ratios are at the very limit of the probe coverage area (i.e., at three o'clock). Concentration gradients are higher in these regions, and the local equivalence ratio can vary sharply around the perimeter of the burner. Since the sample drawn by the probe is localized, the measured equivalence ratio may not be a valid estimate of the mean equivalence ratio of the zone.

It is reasonable to assume that the richest regions of the equivalence ratio distribution have not been adequately covered, and that the mean equivalence ratio based on the seventeen sampled points therefore underestimates the true mean equivalence ratio. For Experiment 81, this is definitely true. Notes taken at the time of the test show that the flame temperature and the NO_x emissions both increased when the injected methane was turned off. The increases would only occur if the mean equivalence ratio (with pure methane injection) had been very rich, since the equivalence ratio of the premixed gases was 0.93 (lean overall). Furthermore, a blue halo of secondary combustion occurred at the exit of the quartz chimney tube where the post-flame gases mixed with room air. However, the weighted average of the seventeen probe measurements is $\bar{\phi} = 1.0$. This certainly underestimates the true mean equivalence ratio.

For the other spatially nonuniform flame experiments, the laboratory notes do not indicate that rich mixtures existed. However, it is possible that their mean equivalence ratios are also underestimated. The optical measurements provide a check on the accuracy of the spatial equivalence ratio measurements. The optical beam passes 1 mm below the flameholder and along the x-axis of the probe measurements (refer to Figure 7). Thus, the beam passes through the richest zones of each of the spatially nonuniform flames, and so the method measures the high methane concentrations in the three o'clock zone.

Optical measurements exist for Experiments 81 through 84, but do not exist for Experiments 87a and 87b. The insulation slipped during the latter two experiments, blocking the optical beam. However, the extinction for those experiments can still be estimated. Five probe measurements of equivalence ratio along the x-axis exist for each of the flames. The general form of Beer's law, equation (4), gives the incremental absorption of the infrared beam as it passes through the reactant gases. The 20-mm diameter of the quartz tube is divided into five zones of length 4 mm each; each zone is assumed to be at the same equivalence ratio as the probe measurement. The incremental absorption of the infrared beam is calculated for each zone and the mean equivalence ratio is estimated using equation (15). This calculation serves two purposes. First, it compares the existing optical measurements with the probe measurements for internal

consistency. Second, it provides an estimate of the expected optical equivalence ratio measurement for Experiments 87a and 87b.

Table 5 compares the measurements and estimates of equivalence ratio for the spatially nonuniform flames. The second column shows the weighted average of the seventeen probe measurements, $\bar{\phi}_{THC}$. The third column shows the optical measurement for Experiments 81 through 84, $\bar{\phi}_{OPT}$. The fourth column shows the equivalence ratio estimated using the procedure described above, $\bar{\phi}_{x\text{-axis}}$. This is called the "x-axis" equivalence ratio since the calculation is based on the probe measurements along the x-axis of the sampling pattern. The next column shows a similar estimate, $\bar{\phi}_{y-axis}$, but the probe measurements along the y-axis are used. (No optical measurements were made along the y-axis; the calculated y-axis equivalence ratio estimate shows the directional bias in the measurements.) The last column reports the difference between the optically-measured equivalence ratio and the probe-averaged equivalence ratio. The four optical equivalence ratio measurements are significantly higher than the probe-averaged mean equivalence ratio. The last column shows that the optical measurements are greater by the 95 percent confidence interval of the optical calibration (2σ or 0.09), on average. Therefore, it is 95 percent likely that the difference between the optical measurements and the probe-averaged mean equivalence ratios is *significant*. Note that the optical measurement for Experiment 81 indicates an overall rich flame.

Table 5 Comparison of Mean Equivalence Ratio Measurements and Estimates for Spatially Nonuniform Flames

Experiment Number	$\bar{\phi}_{THC}$ (Probe)	$\bar{\phi}_{OPT}$ (Optical)	$\bar{\phi}_{x\text{-axis}}$ Estimate	$\bar{\phi}_{y\text{-axis}}$ Estimate	$\bar{\phi}_{OPT} - \phi_{THC}$
81	1.0	1.09	1.06	0.98	0.09
82	0.79	0.89	0.82	0.78	0.10
83	0.86	0.93	0.88	0.79	0.07
84	0.71	0.80	0.73	0.69	0.09
87a	0.78	-	0.81	0.76	-
87b	0.74	-	0.77	0.72	-

Comparing the optically-measured equivalence ratio with the x-axis equivalence ratio estimate, the optical measurement is consistently higher. This supports the assumption that the highest methane concentrations exist beyond the reach of the probe. The x-axis estimated equivalence ratios are also higher than the probe-averaged mean equivalence ratios, a consequence of restricting attention to the axis that contains the highest methane concentrations. The y-axis equivalence ratio estimates are all lower than the probe-averaged mean equivalence ratio. This reveals a directional bias in the optical measurements and the estimated equivalence ratios. Since the optical measurements and the x-axis estimates pass through the richest zones of the spatially nonuniform flames, these measurements overestimate the true mean equivalence ratio. The optical measurements should therefore be considered an upper limit to the true mean equivalence ratio. Similarly, the y-axis equivalence ratio estimates are probably biased lower than the true mean equivalence ratio. If the x-axis and the y-axis equivalence ratio estimates are averaged, the results are within 0.03 of the probe-averaged mean equivalence ratio. It seems reasonable that optical measurements along both the x-axis and the y-axis would have given a better measurement of the true mean equivalence ratio than the single optical measurement or the probe-averaged measurement.

The individual probe measurements of equivalence ratio in each zone are probably reasonably accurate. However, the inability of the probe measurements to sample close to the quartz walls, particularly in the richest zones, biases the probe-averaged mean

equivalence ratios. Lyons encountered a bias in her probe-averaged equivalence ratios, calculating mean equivalence ratios up to ten percent higher than the known equivalence ratio of the reactant gases [19]. In her case the probe-averaged equivalence ratio overestimates the true mean equivalence ratio, and she concludes that "[f]iner measurements taken near the wall may have produced more accurate values for $\bar{\phi}$." Accurate probe sampling to determine mean values is therefore not a trivial matter, and particular attention must be paid to the boundaries of the sample area. The current experiment would have been improved by obtaining more samples closer to the walls. Another improvement would have been avoiding high-penetration methane jets, thereby minimizing the concentration gradients near the walls.

Consider the probe-averaged mean equivalence ratio as a lower limit for the true mean equivalence ratio. Assume that the optical measurements for Experiments 87a and 87b would have been similar to the other four experiments, i.e., $\bar{\phi}_{OPT} = \bar{\phi}_{THC} + 0.09$. The upper limit for the true mean equivalence ratio is $\bar{\phi}_{OPT}$ for Experiments 81 through 84, and 0.87 and 0.83 for Experiments 87a and 87b, respectively. Figure 36 shows the spatially nonuniform flame data using the lower and upper estimates of the mean equivalence ratio. The agreement between the spatially nonuniform and the steady flame data is much closer than it was using the probe-averaged equivalence ratio alone (refer to Figure 28). The exception is Experiment 81, which shows greatly reduced NO_x emissions compared to the steady flames. This reduction is expected for overall rich

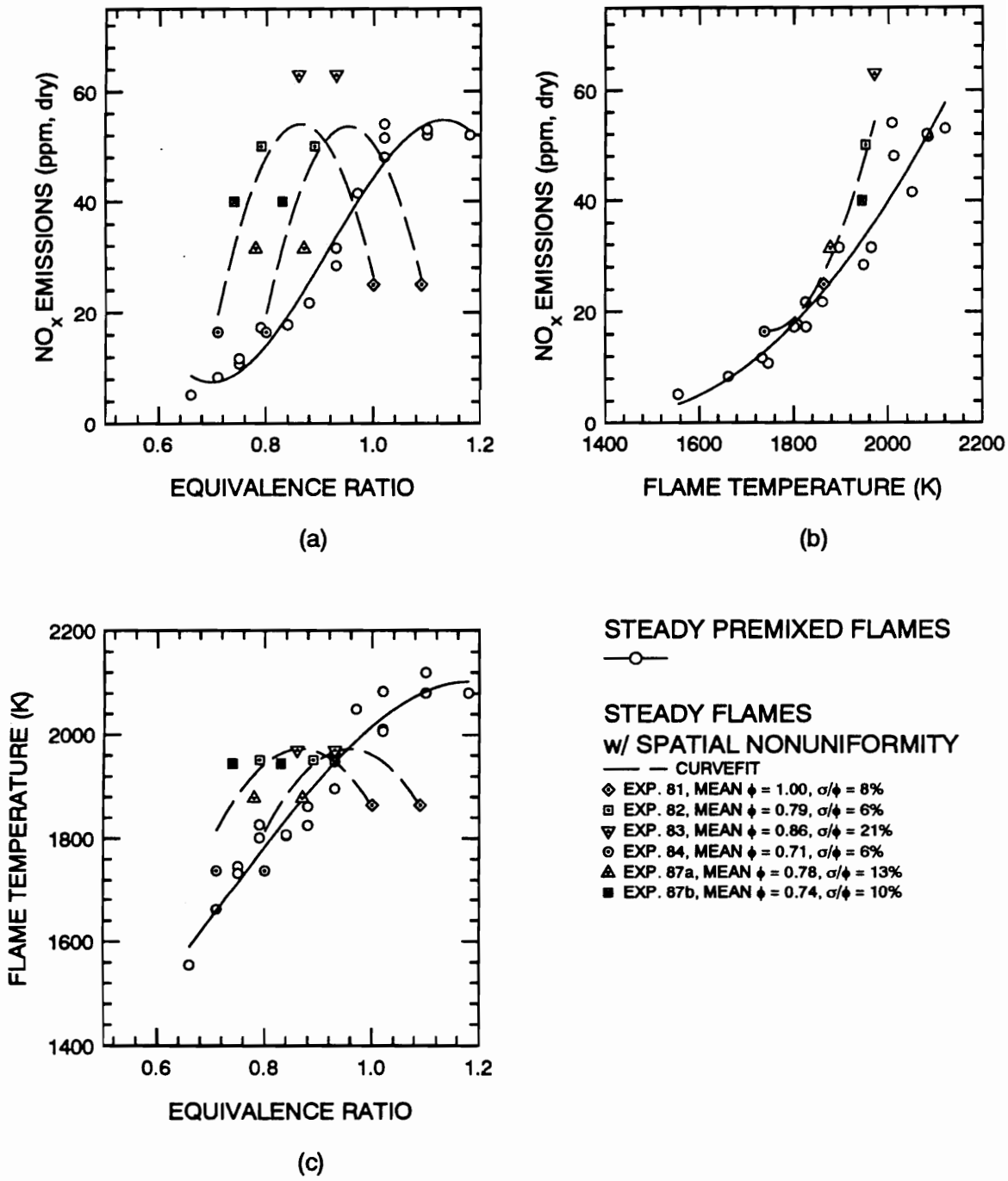

Figure 36 Comparison of Lower and Upper Mean Equivalence Ratio Estimates for Spatially Nonuniform Flames

flames, and for overall stoichiometric flames with nonuniform equivalence ratio distributions. The data for the spatially nonuniform flames should fall somewhere between the limits shown in Figure 36, but unfortunately this additional information does not help correct the predictions of the spatial model. Although the weighting factors for the zones could be altered, this would have to be done on an arbitrary basis. This analysis has exposed the bias of the spatial equivalence ratio measurements, and perhaps it explains the poor performance of the model. However, note that the temperature measurements, and in particular Figure 36 (b), are not affected by these results.

4.2 EMPIRICAL MODEL USING TEMPERATURE FLUCTUATIONS

A second model explains the effect of the temporal fluctuations in equivalence ratio on the NO_x emissions of the pulsing flames. This model uses the estimated temperature fluctuations of the flame zone to predict the expected NO_x emissions. Unfortunately, fluctuating flame temperatures could not be measured directly in the flame zone due to the fragility of the fine wire thermocouple. Fluctuating temperatures were measured in the hot post-flame gases as close as possible to the flame zone, while the large thermocouple measured the axial mean temperature profile all the way to the flame itself. It is important to know the temperature fluctuations in the flame zone to

understand the NO_x production since that process is highly temperature dependent. Therefore, the following procedure was developed to extrapolate the measured temperature fluctuations back to the flame zone.

4.2.1 Extrapolation Procedure

Figure 37 illustrates this procedure. The temperature-versus-time record from the fine thermocouple measurement closest to the flame is extrapolated (step A→B). As a first requirement, the mean of the extrapolated temperatures should match the mean flame temperature indicated by the large thermocouple. This corrects for any catalytic effects on the fine thermocouple, and anchors the otherwise somewhat risky extrapolation to a physically meaningful measurement. The mean temperature of the record is subtracted from every point, so that the temperature record becomes fluctuations about a mean of zero (step B→C). All subsequent manipulations of this zero-mean temperature record change only the unsteady components, and the mean flame temperature is added to the modified record in the last step (step G→H).

The temperature-versus-time record is transformed into its equivalent temperature-versus-frequency record via a *discrete Fourier transform* (DFT, step C→D) [35]. The resulting autospectrum G_{TT} shows which frequencies dominate the temperature record. Normally, the methane injection frequency and its first few harmonics are identifiable.

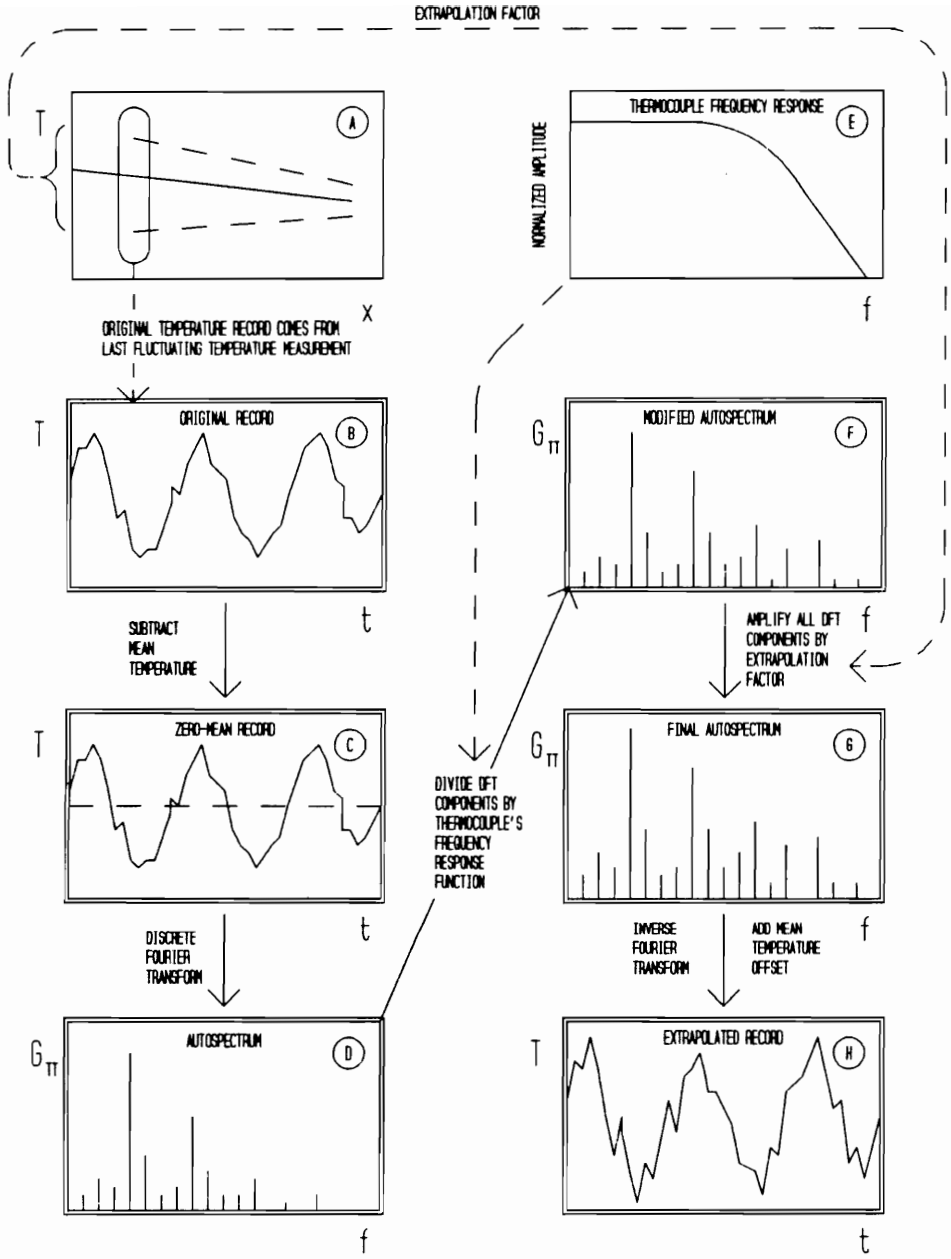

Figure 37 Procedure to Extrapolate Flame Temperatures in Pulsing Flames

The fine thermocouple responds differently to temperature fluctuations at different frequencies, so that the magnitudes of high-frequency components are likely to be attenuated. At this point, the frequency response function A(f) for the thermocouple is calculated (step E). Since this curve is a function of temperature, the mean flame temperature is assumed. Furthermore, since it is difficult to fit a general curve to the frequency response function, its value is calculated directly for the same discrete frequencies as the autospectrum. The frequency response function is always less than unity, reflecting that the thermocouple always has losses and attenuation. Each spectral component of the autospectrum is divided by the frequency response function at the same frequency (step D→F). In this way, the high frequency components are amplified more than the low frequency components, correcting for the attenuated response of the thermocouple.

The modified autospectrum now estimates the actual gas temperature fluctuations at the fine thermocouple's measurement location. The extrapolation proceeds by estimating the growth of the amplitude of the fluctuations as the flame zone is approached. Figure 31 shows the minimum, mean, and maximum temperature profiles in the burner. The difference between the maximum and minimum temperatures is a measure of the amplitude of the temperature fluctuations. A linear fit is made to the minimum and maximum temperatures, and these lines are extended to estimate the difference between the maximum and minimum temperatures at the flame zone. Each

spectral component of the autospectrum is multiplied by an *extrapolation factor,* defined as the amplitude of the estimated flame zone temperature divided by the amplitude of the gas temperature at the last measurement location (step F→G).

The extrapolated temperature-versus-time record is reconstructed through an inverse DFT [35]. The large thermocouple mean temperature is added to the record as a DC offset, and the extrapolation procedure is complete (step G→H). The new record estimates the actual gas temperature fluctuations at the flame zone. The amplitude of the record is greater than the original thermocouple measurement, and some of the higher frequency components are enhanced. The computer program for the extrapolation procedure is listed in Appendix D.

4.2.2 Results of Extrapolation

The temperatures of the pulsing flames were estimated following the extrapolation procedure. The extrapolation factors for Experiments 70, 76, and 77 are 1.18, 1.08, and 1.25, respectively. Figure 38 shows the autospectra of the original temperature records (dotted curve) and the modified autospectra (solid curve). The autospectra have a spectral resolution of 0.25 Hz. The Nyquist frequency of the data is 25 Hz. This is the highest frequency component that can be regained from the sampled temperature records. However, frequencies over 12.5 Hz were not needed and only the first 50 components

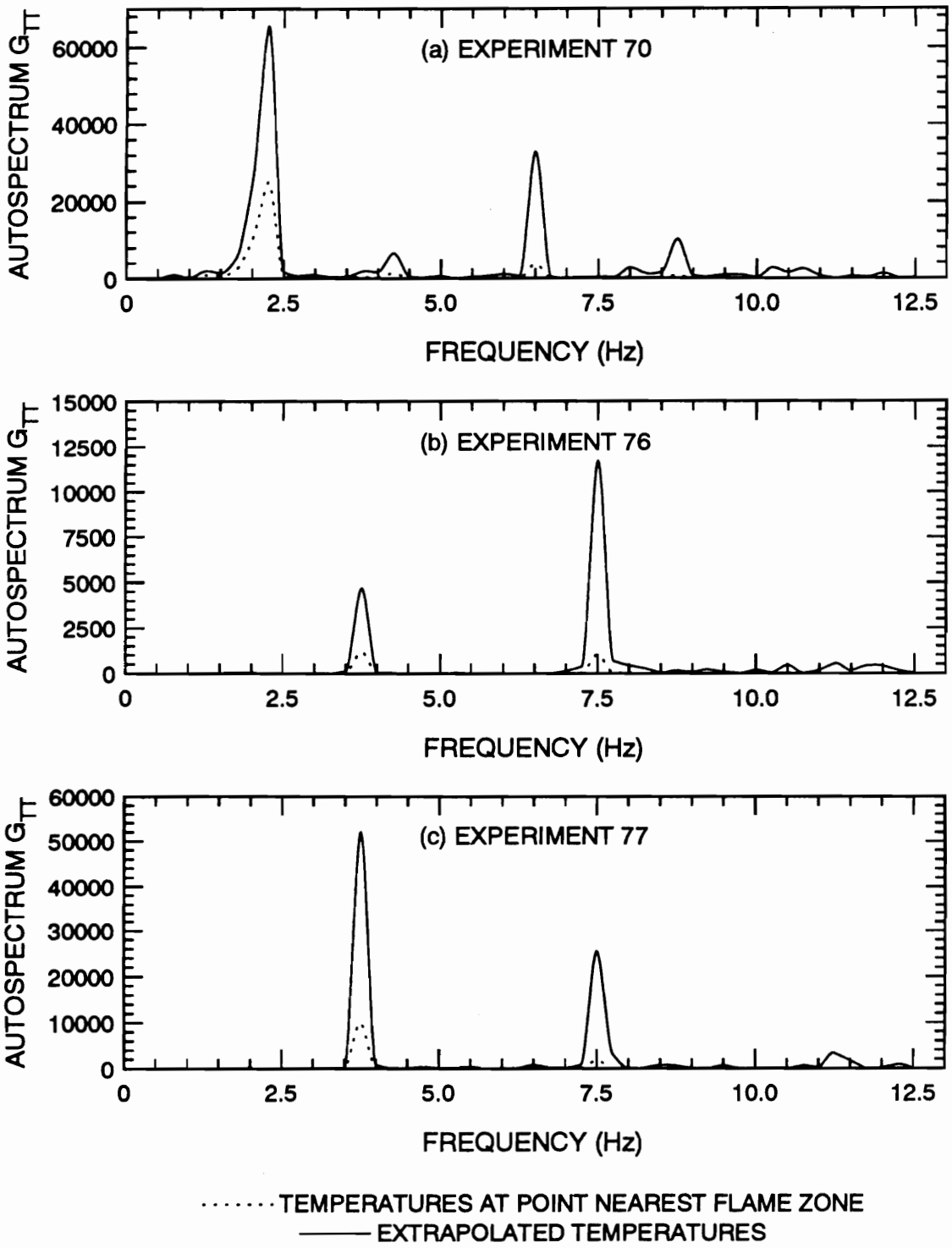

Figure 38 Autospectrum of Temperature Measurements in Pulsing Flames, Comparison of Original and Extrapolated Autospectra

of the DFT were calculated. Figure 38 shows that the temperature records are dominated by the methane injection frequency and its harmonics. For Experiments 70 and 77, the fundamental injection frequency dominates (2.25 Hz and 3.75 Hz, respectively). The modified autospectra show that while the fundamental frequency still dominates, the strength of the harmonic components is significantly amplified. This is primarily due to step D→F of the extrapolation procedure, which corrects for the attenuation of the higher frequencies. However, for Experiment 76, the first harmonic of the modified autospectra is stronger than the fundamental (fundamental at 3.75 Hz). This could certainly arise from the sharp falloff of the frequency response function; as the frequency increases, the amplification of the autospectrum term gets larger. In fact, it is necessary to cut off the extrapolation procedure at some frequency to avoid over-amplifying minor high frequency components which are solely due to noise. The practical frequency limit for these thermocouples is about 10 Hz. Is the strength of the first harmonic for Experiment 76 real or an artifact of the extrapolation procedure? While the original autospectrum shows that the fundamental and the first harmonic components are equally strong, this does not confirm that the first harmonic of the modified autospectrum should be as strong as it is. Similarly, the magnitude of the second harmonic frequency for Experiment 70 could be suspect. An independent estimation of the flame temperatures made in the next section serves as a check on these results.

The original temperature measurements (dotted curve) and the extrapolated flame zone temperatures (solid curve) are shown in Figure 39. Note that the amplitude of the temperature fluctuations for each case has doubled through extrapolation and frequency compensation. The fundamental pulse frequency is still evident, but the greatest difference between the original and extrapolated temperatures is the increased harmonic content. In Experiments 70 and 77, the amplitude of the fundamental is dominant over the effects of the harmonics. In Experiment 76, however, the first harmonic is strong enough that it is as important as the fundamental.

Another tool of signal analysis is the *probability density function* (pdf). The pdf emphasizes the dominant temperatures of the records; it indicates which temperatures are the most likely to be measured by a random sampling of the flame temperature [35]. The pdf is calculated by dividing the range of possible temperatures (the minimum to the maximum) into a series of equal-width temperature intervals (20 are used here). The number of times that a temperature measurement falls within each temperature interval is counted, and the sum is normalized by the number of samples (200). The integral of the pdf, from its lowest to its highest temperature limits, is unity; i.e.

$$\int_{T_{min}}^{T_{max}} pdf(T)\, dT = 1 \quad .$$

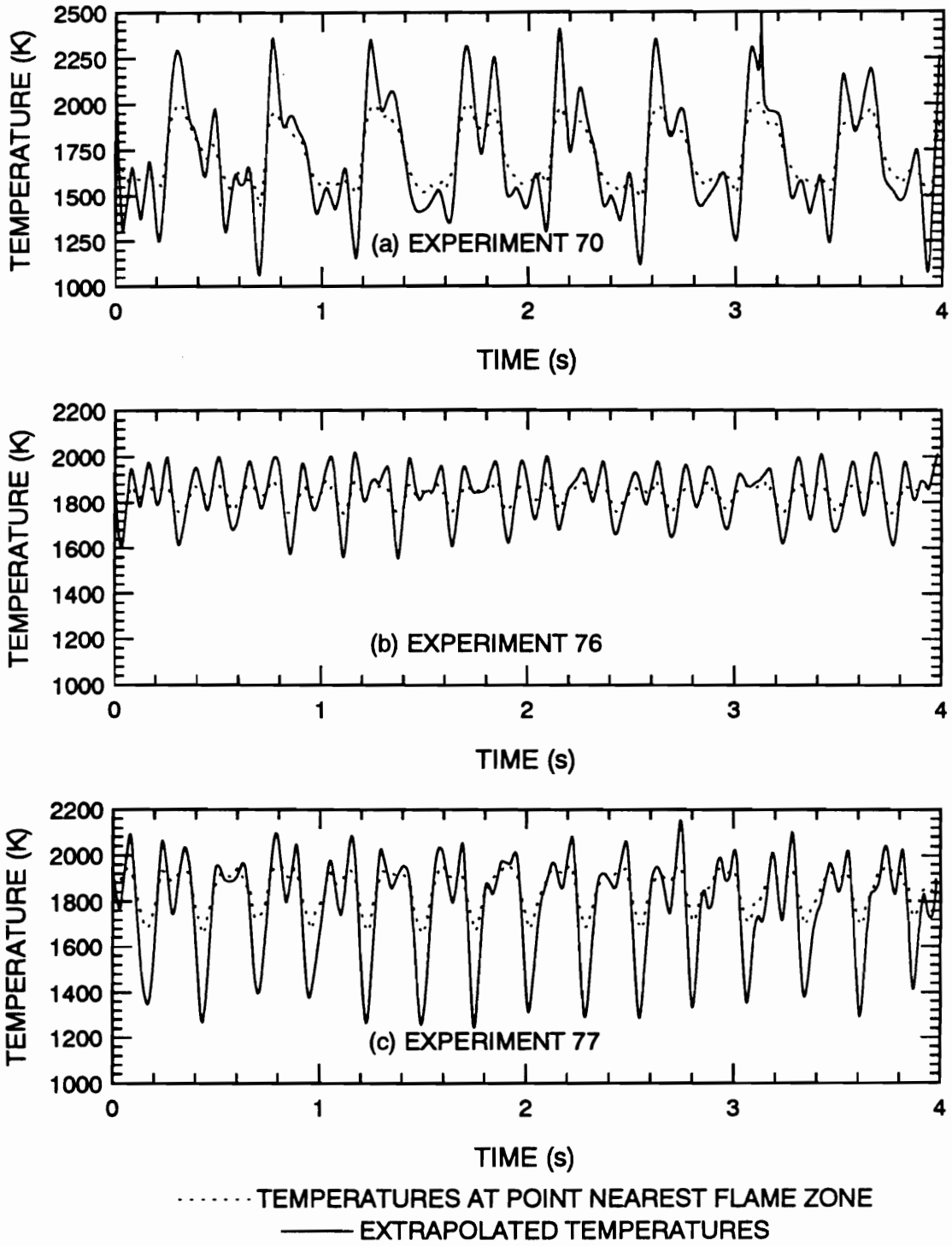

Figure 39 Comparison of Original Fluctuating Temperature Measurements and Extrapolated Estimates of Flame Temperatures

The probability density functions for the extrapolated pulsing flame temperatures are shown in Figure 40. The peaks represent the most likely temperatures to be measured, or said another way they show at which temperatures the flame spends most of its time. Note that in every case the most likely temperature is not the mean flame temperature. For Experiment 70, the most likely temperature is below the mean temperature, and for Experiments 76 and 77 the most likely temperature is higher than the mean temperature. While these most likely temperatures might be expected to dominate the NO_x production of each flame, the nonlinear effect of temperature on NO_x production emphasizes the importance of the high-temperature fluctuations. The width of the pdf is critical, because the greatest amount of NO_x is formed at the highest temperatures, and a wider pdf indicates a greater deviation from a well-premixed flame. One would therefore expect the strongest deviation from a steady flame for Experiment 70 (despite its low *most probable* temperature), and the least deviation for Experiment 76. Figure 33 (b) shows that the deviation from steady flames is similar for all of the pulsing flames, but these flames have both temporal and spatial effects. When only the temporal effects are considered (in Section 4.2.4), the magnitude of the temporal effects agrees with the pdfs shown in Figure 40.

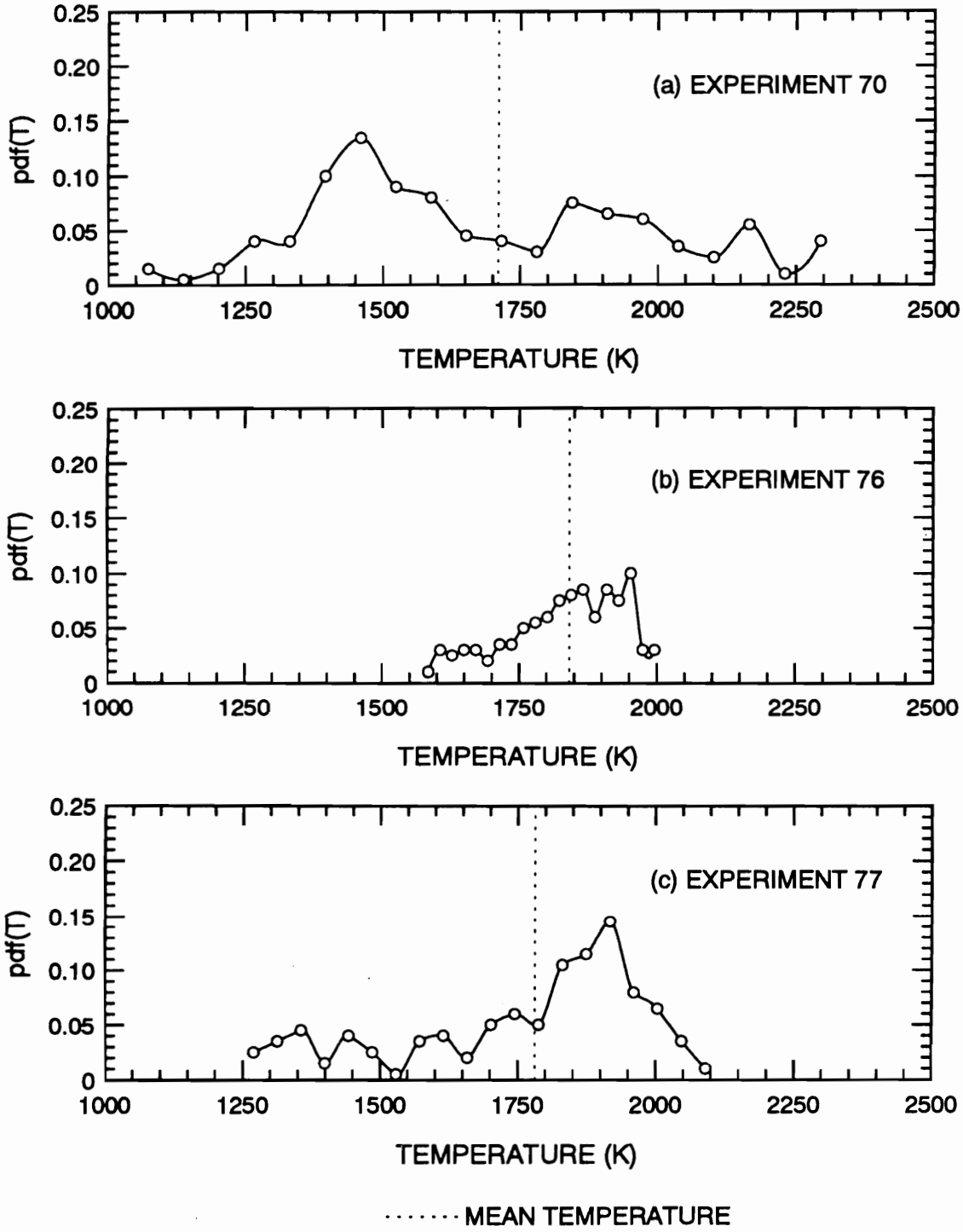

Figure 40 Probability Density Functions for the Extrapolated Flame Temperatures of the Pulsing Flames

4.2.3 Optically Estimated Flame Temperatures

Admittedly, the extrapolation of any property can result in large errors. In order to check the accuracy of the extrapolation procedure, the temperature of the flame zone was estimated with an independent measurement. The optical measurements of equivalence ratio fluctuations indicate the instantaneous richness of the flame zone. Assuming that the instantaneous temperature of a pulsing flame will be the same as the temperature of a steady flame at the same equivalence ratio, another estimate of the actual flame zone temperature can be derived. The record for $\phi(t)$ from Figure 32 is multiplied by the experimental curvefit $T(\phi)$ from the steady flames (equation (20)) to yield another estimate for T(t). The temperature record is shifted by a constant to force its mean temperature to match the measured mean flame temperature. Despite this modification, this second estimate is valuable as a check of the frequency and amplitude of the thermocouple-extrapolated flame temperatures.

Figure 41 compares the thermocouple-extrapolated flame temperatures (solid curve) with the equivalence ratio-estimated flame temperatures (dotted curve). The agreement is good. The mean temperatures have been forced to agree, but the match in the amplitude of the records is almost surprising. The extrapolation procedure perhaps overcorrects for the harmonic content, especially for the second harmonic of Experiment 70. "Sharp" features in the original temperature record are associated with the high

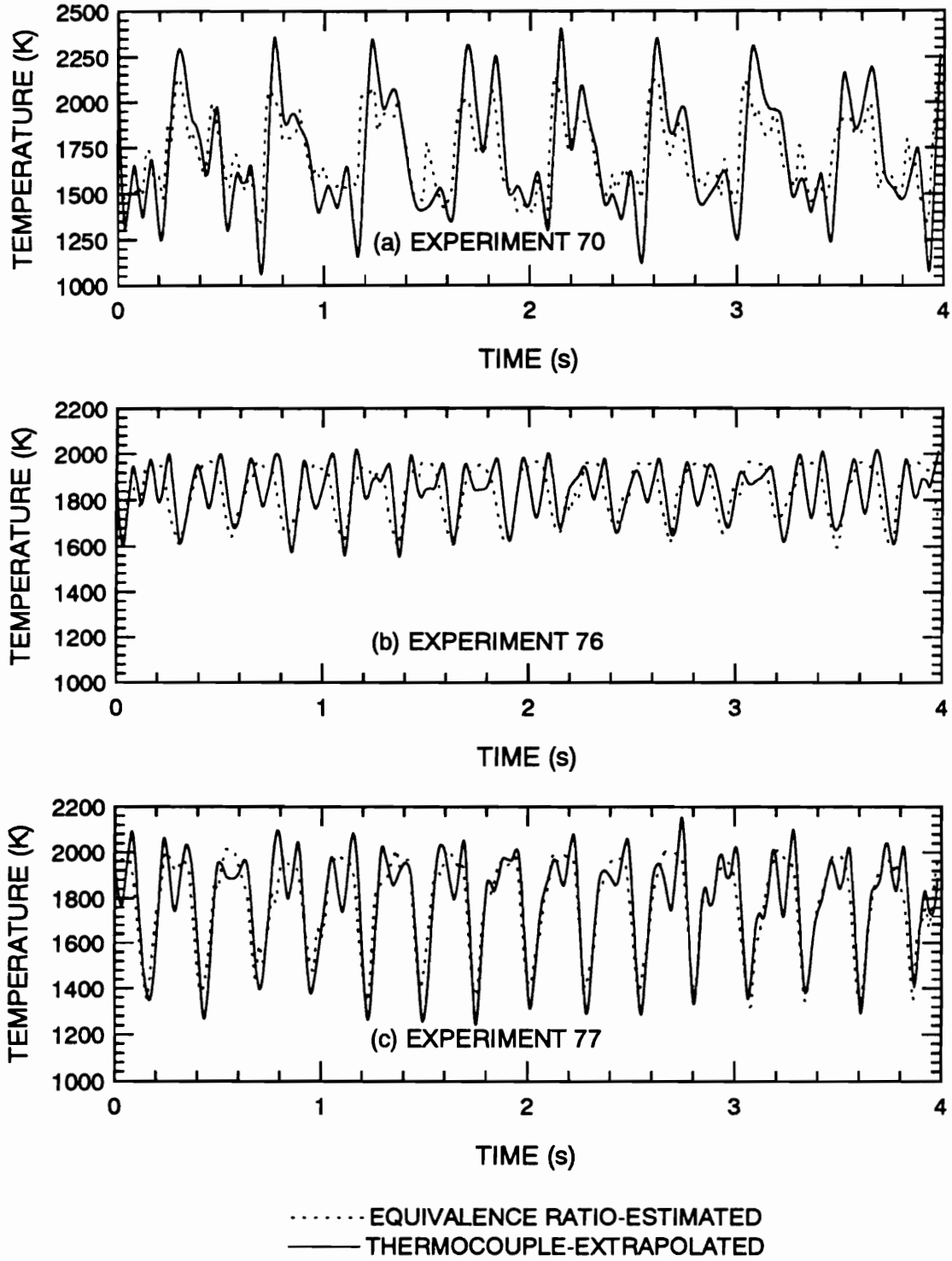

Figure 41 Comparison of Thermocouple-Extrapolated and Equivalence Ratio-Estimated Pulsing Flame Temperatures

frequency components of the autospectrum, and the frequency compensation accentuates these features in the extrapolated waveforms. However, the amplitude of the two estimates are in close agreement, particularly for Experiments 76 and 77. These results show that the original temperature measurements can be corrected with the extrapolation procedure described previously.

Figure 42 compares the probability density functions of the two flame temperature estimates. Both pdfs have similar shapes and predict nearly identical most probable temperatures. The differences are evident in the wider limits for the extrapolated pdfs, especially for Experiment 70. However, these differences are primarily in the tails of the distributions, and at low probabilities.

Figure 43 compares the autospectra from the thermocouple-extrapolated and equivalence ratio-estimated temperatures. The purpose of this comparison is to examine whether the harmonic frequencies in the extrapolated temperatures are consistent with the fluctuations in equivalence ratio. Figure 43 (a) indicates that the second harmonic is truly stronger than the first harmonic for Experiment 70. The extrapolation procedure correctly compensated for the response of the thermocouple in this case. The difference in the amplitude of the temperature fluctuations between the thermocouple-extrapolated and equivalence ratio-estimated records is due to overestimating the extrapolation factor (thereby overamplifying all of the frequency components). Figure 43 (b) indicates that

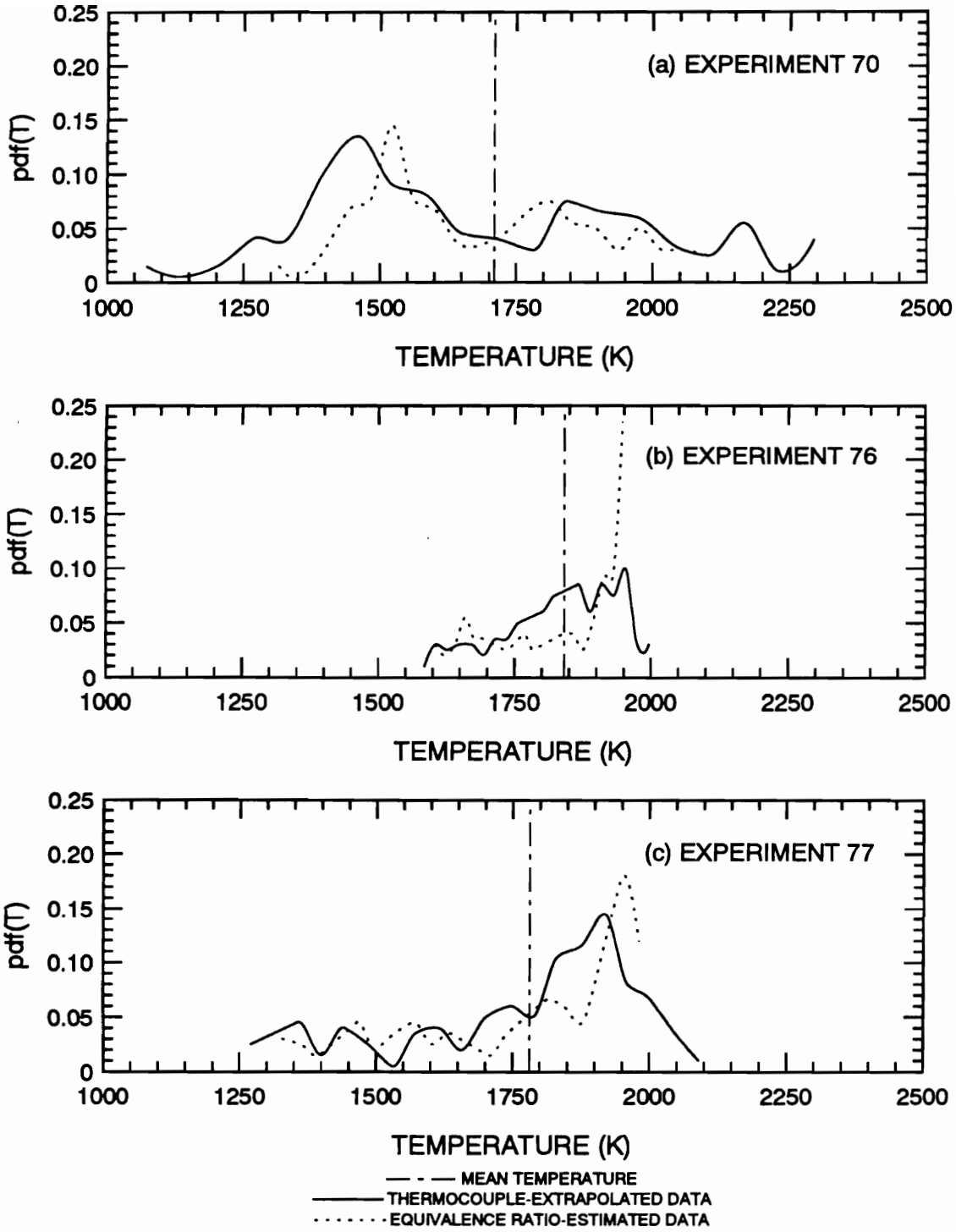

Figure 42 Comparison of Probability Density Functions for Extrapolated and Optically-Estimated Flame Temperatures

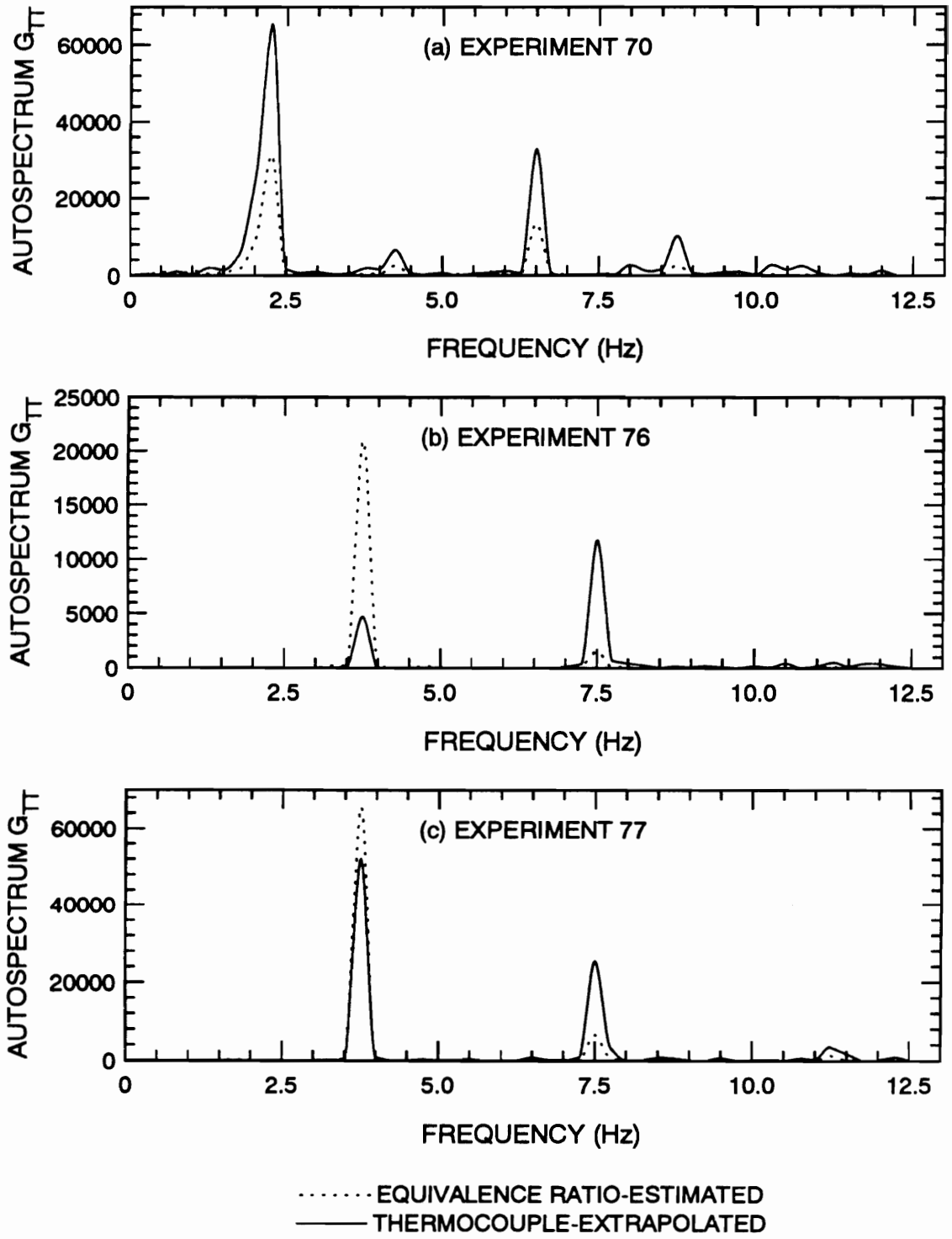

Figure 43 Comparison of Autospectra from Thermocouple-Extrapolated and Equivalence Ratio-Estimated Temperatures

the strength of the first harmonic in the thermocouple-extrapolated record of Experiment 76 is overestimated. Figure 41 (b) shows good agreement between the amplitudes of the two temperature estimates, but an unusually high harmonic content in the thermocouple-extrapolated estimate. In this case, the opposite conclusions are found for the extrapolation procedure: the frequency response correction introduced some errors, but the extrapolation factor was estimated accurately. Figure 43 (c) shows that Experiment 77 was a success. The relative magnitude of the fundamental and its harmonics is correct, and the estimated temperatures are in excellent agreement.

4.2.4 Temporal Model

The temporal model uses the $NO_x(T)$ curvefit from the steady flames (equation (18)) to estimate the NO_x emissions from the pulsing flames. It integrates the product of the temperature pdf of a pulsing flame and the NO_x emissions produced by a steady flame at the same temperature, that is

$$\overline{NO_x} = \int_{T_{min}}^{T_{max}} pdf(T) \cdot NO_x(T)\, dT \quad . \tag{24}$$

Equation (24) is approximated using the discrete data of the experiment:

$$\overline{NO_x} = \sum_{T_{min}}^{T_{max}} pdf(T) \cdot NO_x(T) \quad , \tag{25}$$

in which the extrapolated flame temperatures are used for the pdf. Figure 44 shows the NO_x emissions for the pulsing flames predicted using equation (25) (symbols with dots). For Experiment 70, the results account for almost all of the increase in NO_x with respect to steady flames. For Experiment 77 this model accounts for two thirds of the increase in emissions. This could be interpreted in many ways, but one obvious explanation is that the other third of the increase in NO_x emissions is due to the small but unavoidable spatial nonuniformity of these flames. Certainly, the spatial nonuniformity of the flames will contribute to some increase in NO_x. There is very little difference between the prediction and the steady flame data for Experiment 76. However, the measured increase in NO_x emissions exists. In keeping with the previous interpretation, this flame could be strongly dominated by its spatial effects rather than its temporal effects. Among the pulsing flames, Experiment 76 had the smallest amplitude temperature fluctuations, and would therefore be expected to have the smallest effect of its temperature fluctuations on NO_x emissions. Furthermore, Figure 33 (b) indicates that the effect of spatial equivalence ratio nonuniformities increases as the mean flame temperature increases. This trend could explain the relative contribution of spatial effects in these pulsing flames.

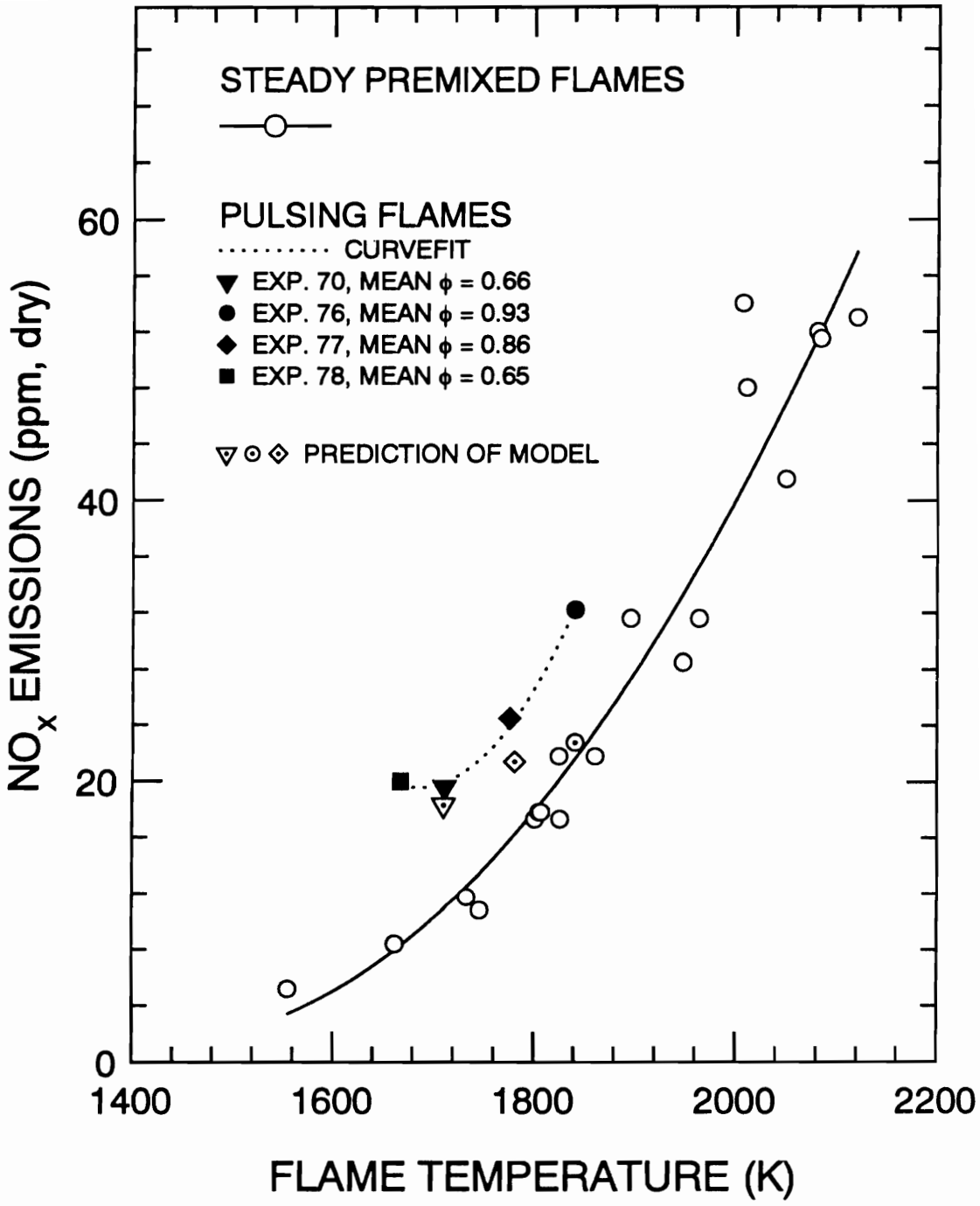

Figure 44 Prediction of NO_x Emissions from Pulsing Flames

Gouldin's inequality (equation (3)) claims to indicate when the effect of temperature fluctuations on NO_x emissions should be negligible. The left-hand side of equation (3) has been evaluated with the extrapolated flame temperatures. An activation energy of 75,400 cal/kmol was assumed, corresponding to the rate-determining step of the thermal NO_x mechanism [50]. The results of the calculation are given in Table 6. The NO increase in the third column is defined as

$$\Delta NO_x(\%) = \frac{NO_{x,\,measured} \times 100}{NO_x(T)} \quad .$$

Gouldin predicted that temporal effects are negligible only when the term on the left-hand side of equation (3) is $<< 1$. Table 6 indicates that the temporal effects should be non-negligible for each of the experiments, since the value of the left-hand-side term is greater than unity. Gouldin did not claim to predict the *magnitude* of the temporal effects on NO_x emissions, yet these results scale with the predictions of the temporal model and with the measured NO_x increases. The temperature fluctuations of Experiment 70 should have the most significant effect on the NO_x emissions, and the temperature fluctuations of Experiment 76 should have the least effect. The results for Experiment 77, where the value of the left-hand term is intermediate, are reflected in the prediction of the temporal model. The temperature fluctuations have some effect, but the NO_x increase is smaller than for Experiment 70. The temporal model accounts for a NO_x increase of about six percent for Experiment 76. This result either defines the

Table 6 Evaluation of Gouldin's Inequality Using Pulsing Flame Data

Experiment Number	Gouldin's Inequality	NO_x Increase (%)
70	15	68
76	1.4	6
77	6.8	36

practical interpretation of "non-negligible" as a NO_x increase on the order of 6 percent, or it suggests that the NO_x prediction of the temporal model should be higher for this case. This latter interpretation presumes that "non-negligible" is defined by some larger NO_x increase, and this arbitrary assumption is unwarranted.

The characteristics of the probability density functions are the best indicators of the relative increase in NO_x predicted by the model. The amplitude of the temperature fluctuations is expected to influence the NO_x emissions, and Experiment 70 had the widest limits and the highest predicted increase in NO_x due to its temperature fluctuations. More important than the width of the temperature extremes, however, is the probability of the high temperature fluctuations. Figure 40 shows that Experiment 70 had relatively high pdf probabilities (> five percent) for temperatures 450 K higher than the mean temperature. For Experiment 76, the significant temperature excursions are only 100 K higher than the mean. For Experiment 77, there are important temperature fluctuations 125 K higher than the mean temperature, and still significant excursions 225 K higher than the mean temperature. The temperature pdfs clearly reflect the relative magnitude of the NO_x emissions predicted by the model.

Unfortunately for the completeness of this work, the model for spatial effects is insufficiently accurate to account for the difference between the temporal model's predictions and the measured NO_x emissions for the pulsing flames. The experimental

data for the spatially nonuniform flames indicate that the effect of the spatial nonuniformities increases as the mean flame temperature increases. This supports the idea that the spatial effects in Experiment 70 would be the least, and the spatial effects in Experiment 76 would be the greatest. However, an independent quantitative estimate of the spatial effects in the pulsing flames cannot be obtained with the experimental data.

CHAPTER 5

CONCLUSION

5.1 SUMMARY

The effects of temporal fluctuations and spatial nonuniformity of equivalence ratio on NO_x emissions in premixed flames have been investigated. Three types of flames were studied: temporally steady homogeneously premixed flames, temporally steady flames with spatially nonuniform equivalence ratio distributions, and temporally unsteady (pulsing) flames. The pulsing flames also have a small but unavoidable degree of spatial nonuniformity. Three quantities were measured in these flames: mean NO_x emissions, equivalence ratios, and temperatures. Equivalence ratios were measured temporally, spatially, and in their mean. Mean and fluctuating temperatures were measured. Both temporal and spatial unmixedness were quantified, and their effect on NO_x emissions was shown.

In addition, an optical technique was developed to measure temporal fluctuations in equivalence ratio. The strengths and limitations of this system were described. A

compensation technique for the frequency response of fine thermocouples was developed, and good agreement was obtained between the thermocouple and optical measurements. Empirical models for the spatially nonuniform and pulsing flames explain most of the differences between the spatially nonuniform flames, the pulsing flames, and the steady flames.

5.2 CONCLUSIONS

The original goal of the experiment was to measure and explain the effect of temporal variations in equivalence ratio on NO_x emissions in premixed flames. Its purpose was to quantify the magnitude of the problem and to discover if temporal variations are equally significant contributors to NO_x emissions as spatial nonuniformities in equivalence ratio. An additional purpose was the development of a technique for the required temporally-resolved equivalence ratio measurements.

To a large extent, these goals have been satisfied. The measurements have shown that both temporal and spatial variations in equivalence ratio can lead to substantially increased NO_x emissions, compared to steady uniform flames at the same mean flame temperature. The effect of spatial nonuniformities is greatest at the highest mean flame temperatures, and the increases in NO_x were moderate to insignificant at lower mean flame temperatures. However, anomalies in the spatially nonuniform flame data were

observed. The correlation between mean flame temperature and mean equivalence ratio differed from the correlation for steady flames, and this difference affected the predictions of an empirical model used to predict NO_x emissions. Part of this problem is due to a bias in the estimated mean equivalence ratio, which underestimates the true mean equivalence ratio by up to 0.10. The small burner diameter was another problem in this respect, and the burner walls probably intervened in the combustion process. As Figure 29 and Figure 35 show, neither the data nor the empirical model were able to consistently correlate the unmixedness to the increase in NO_x emissions.

The unsteady flames were complicated by the simultaneous presence of temporal fluctuations and spatial nonuniformities in equivalence ratio. However, the burner design minimized the spatial nonuniformities. The data show that the unsteady flames consistently produce more NO_x than steady flames at the same mean flame temperature, and the greater the amplitude of the equivalence ratio fluctuations, the greater the increase in NO_x emissions above the uniformly premixed case having the same mean temperature. The empirical model attributes part to all of the increase in NO_x to temporal effects in unsteady flames, but the remainder of the increase in NO_x must be assumed to be due to spatial effects. The results of the empirical model for the equivalence ratio fluctuations make sense in terms of the amplitude of the temperature fluctuations for the different cases, and the results are particularly satisfactory when the probability density functions for the experimental cases are considered. Indeed, the

probability density functions of equivalence ratio are much more informative than a more vaguely defined "amplitude" of the fluctuations for nonsinusoidal, nonsymmetric waveforms.

The research has shown that fluctuations in equivalence ratio can have a significant effect on NO_x emissions from premixed flames, greater than the effect of spatial nonuniformities under certain conditions. This has particularly important consequences for designers of lean premixed gas turbine combustors. The chief consequence is that temporal equivalence ratio fluctuations must be measured and controlled to reduce NO_x emissions; probe sampling will not detect the fluctuations. The research has developed a nonintrusive technique for temporally-resolved equivalence ratio measurements that may someday be applied to industrial-scale experiments.

5.3 RECOMMENDATIONS FOR FUTURE WORK

The following are suggestions to improve any future variations of the experiment. First, a larger burner should be used to minimize the thermal and chemical effects of the quartz chimney walls on the flame. Thermocouple probes would have less impact on the flame, and the lean flammability limits of the burner would be lower. Flow velocities could be increased for improved resolution of temporal fluctuations and higher fluctuation frequencies. A perfect candidate for this type of investigation is the burner developed

by Langhorne et al. to study an active control system for combustion oscillations [54]. This burner could impose controlled methane fluctuations at up to 76 Hz and it had a 70-mm diameter quartz chimney. However, the increased scale of the burner would also lead to other complications. The optical technique developed for the current experiment would need modifications to reduce the extinction over the longer path length (for example, shift the frequency of the infrared source slightly away from 3391 nm). The current research showed the importance of temperature measurements in the flame, and the thermocouple compensation techniques developed here should be adequate up to 10 Hz. However, for higher frequencies alternative temperature measurement techniques would have to be used. Various thermocouple compensation techniques exist for single junction [55-61] and dual junction [62,63] probes. The frequency limitations of these techniques are in the kHz range.

The dissertation discusses the possible catalytic effects of the hot flameholder on the flame in Section 3.2. These catalytic effects could be investigated by changing the gage of the stainless steel flameholder screen. By modifying the surface area of the steel in contact with the flame gases, the relative effect of catalytic reactions would be altered. Another approach would be to put a thermocouple-type anticatalytic ceramic coating on the flameholder.

The current research clearly shows the need for improved temporally resolved diagnostics techniques. While nonintrusive techniques for temporal resolution of temperature and equivalence ratio fluctuations exist, these techniques are generally expensive and not readily applicable to industrial-scale experiments. CARS thermometry, for example, requires a powerful laser and is limited to a sampling rate of about 25 Hz [64-66]. Thermometry by Rayleigh scattering is affected by particulates and changes in the composition of the gases [60]. For temporal equivalence ratio measurements, effort should be devoted to the development of an infrared absorption probe that could go into a full-scale combustor. The optical technique used in this experiment would require a faster detector for turbulent flows, and the lock-in amplifier would be incompatible with turbulent flows due to its limited temporal response. A chemiluminescent technique for temperature and equivalence ratio measurements has also shown promise for practical applications [67].

While the experiment described in this dissertation addressed the effect of mean equivalence ratio and fluctuation amplitude of equivalence ratio on NO_x emissions, our understanding of the effect of the frequency of the temperature fluctuations on NO_x emissions still needs improvement. It is likely that a flame has a cutoff frequency, beyond which it is decreasingly able to respond to fluctuations in equivalence ratio or temperature [68]. This cutoff frequency would be on the order of the inverse of the chemical reaction time, possibly in the range of turbulent flow fluctuations. The

implication is that NO_x emissions would not be affected by temporal fluctuations in equivalence ratio if the frequency of the oscillation is sufficiently high. The author is currently working on this problem with Nasser Darabiha of *Ecole Centrale Paris*. A full chemical kinetic model of the burner used in this experiment is being developed, and the frequency of the equivalence ratio fluctuations in the model can be changed freely. However, an experimental program should accompany the theoretical work. Well-controlled frequencies over 100 Hz probably cannot be achieved with mechanical fuel injectors, and turbulent flames are subject to a wide range of frequencies. An experiment using acoustically-modulated equivalence ratio fluctuations, with an emphasis on measuring the effect of the frequency on the NO_x emissions, would be a useful contribution.

Although this research has demonstrated the importance of considering temporal as well as spatial effects on NO_x emissions, the experiment did not address the *causes* of temporal equivalence ratio fluctuations in practical combustors. This is the true source of NO_x control problems and an inadequately understood area of combustor design. Combustor acoustics should be studied for their probable effects on mixing and combustion chemistry, not just for their effect on mechanical fatigue failures. This research should especially concentrate on the possible interactions between combustor acoustics and the fuel feed systems, to understand under which conditions the acoustics can modulate the flow rates of fuel and air. Some work in active control systems is

already under way [54,69], but direct effort is required to improve passive minimization of temporal equivalence ratio fluctuations.

REFERENCES

1 Correa, S., *"A Review of NO_x Formation Under Gas-Turbine Combustion Conditions,"* Combustion Science and Technology, vol. 87, pp. 329-362, (1992).

2 Davis, L. B., and Washam, R. M., *"Development of a Dry Low NO_x Combustor,"* ASME Paper 89-GT-255, (1989).

3 Bowman, C. T., *"Control of Combustion-Generated Nitrogen Oxide Emissions: Technology Driven by Regulation,"* 24th Symposium (International) on Combustion, The Combustion Institute, pp. 859-878, (1992).

4 Kuwata, Y., Turbine Technology Department, General Electric Company, Personal Communication (1991).

5 Mahan, J. R., and Roby, R. J., Department of Mechanical Engineering, Virginia Polytechnic Institute and State University, Personal Communication (1991).

6 Zeldovich, Y. B., Acta Physicochim. URSS, vol. 21, p. 577, (1946).

7 Richter, G. N., Wiese, H. C., and Sage, B. H., *"Oxides of Nitrogen in Combustion. Premixed Flame,"* Combustion and Flame, vol. 6, pp. 1-8, (1962).

8 Richter, G. N., Reamer, H. H., and Sage, B. H., *"Oxides of Nitrogen in Combustion. Investigations in a Premixed Flame,"* Chemical Engineering Science, vol. 17, pp. 813-823, (1962).

9 Opsahl, A. W., and Seagrave, R. C., *"The Effect of Oscillatory Combustion on the Formation of Atmospheric Pollutants,"* Combustion and Flame, vol. 14, pp. 325-339, (1970).

10 Fletcher, R. S., and Heywood, J. B., *"A Model for Nitric Oxide Emissions from Aircraft Gas Turbine Engines,"* AIAA Paper No. 71-123, American Institute of Aeronautics and Astronautics, New York, (1971).

11 Pompei, F., and Heywood, J. B., *"The Role of Mixing in Burner-Generated Carbon Monoxide and Nitric Oxide,"* Combustion and Flame, vol. 19, pp. 407-418, (1972).

12 Appleton, J. P., and Heywood, J. B., *"The Effects of Imperfect Fuel-Air Mixing in a Burner on NO Formation From Nitrogen in the Air and the Fuel,"* 14th Symposium (International) on Combustion, The Combustion Institute, pp. 777-786, (1972).

13 Thompson, D., Brown, T. D., and Beer, J. M., *"Formation of NO in a Methane-Air Flame,"* 14th Symposium (International) on Combustion, The Combustion Institute, p. 787, (1972).

14 Gouldin, F. C., *"Controlling Emission from Gas Turbines - The Importance of Chemical Kinetics and Turbulent Mixing,"* Combustion Science and Technology, vol. 7, pp. 33-45, (1973).

15 Vranos, A., *"Turbulent Mixing and NO_x Formation in Gas Turbine Combustors,"* Combustion and Flame, vol. 22, pp. 253-258, (1974).

16 Gouldin, F. C., *"Role of Turbulent Fluctuations in NO Formations,"* Combustion Science and Technology, vol. 9, pp. 17-23, (1974).

17 Semerjian, H. G., and Vranos, A., *"NO_x Formation in Turbulent Premixed Flames,"* 16th Symposium (International) on Combustion, The Combustion Institute, (1976).

18 Semerjian, H. G., Ball, I. C., and Vranos, A., *"Pollutant Emissions From 'Partially' Mixed Turbulent Flames,"* 17th Symposium (International) on Combustion, The Combustion Institute, pp. 679-687, (1978).

19 Lyons, V. J., *"Fuel/Air Nonuniformity—Effect on Nitric Oxide Emissions,"* AIAA Journal, vol. 20, pp. 660-665, (1982).

20 Noyce, J. R., and Sheppard, C. G. W., *"The Influence of Equivalence Ratio Variation on Pollutant Formation in a Gas Turbine Type Combustor,"* Combustion Science and Technology, vol. 29, pp. 37-52, (1982).

21 Kaper, H. G., Leaf, G. K., Matalon, M., and Gorman, M., *"The Stability of Plane Flames Attached to a Flameholder,"* Combustion Science and Technology, vol. 43, pp. 271-286, (1985).

22 Glassman, I., Combustion, 2nd ed., Academic Press Inc., (1987).

23 Hegde, U. G., Reuter, D., Daniel, B. R., and Zinn, B. T., *"Flame Driving of Longitudinal Instabilities in Dump Type Ramjet Combustors,"* Combustion Science and Technology, vol. 55, pp. 125-138, (1987).

24 Kailasanath, K., Gardner, J. H., Boris, J. P., and Oran, E. S., *"Acoustic-Vortex Interactions and Low-Frequency Oscillations in Axisymmetric Combustors,"* AIAA Journal of Propulsion and Power, vol. 5, pp. 165-171, (1989).

25 Maughan, J. R., Warren, R. E., Tolpadi, A. K., and Roloff, T. P., *"Effect of Initial Fuel Distribution and Subsequent Mixing on Emissions From Lean, Premixed Flames,"* ASME Paper 92-GT-121, (1992).

26 Fric, T. F., *"Effects of Fuel-Air Unmixedness on NO_x Emissions,"* AIAA Paper 92-3345, Presented at AIAA/SAE/ASME/ASEE 28th Joint Propulsion Conference and Exhibit, July 6-8, 1992.

27 Reisel, J. R., Campbell, D. C., Laurendeau, N. M., and Drake, M. C., *"Laser-Saturated Fluorescence Measurements of Nitric Oxide in Laminar, Flat, $C_2H_6/O_2/N_2$ Flames at Atmospheric Pressure,"* Combustion Science and Technology, vol. 91, pp. 271-296, (1993).

28 Gulati, A., and Warren, Jr., R. E., *"NO_2-Based Laser-Induced Fluorescence (LIF) Technique to Measure Cold-Flow Mixing,"* AIAA Paper 92-0511, (1992).

29 Wirth, D. A., Soot Formation in Vitiated-Air Diffusion Flames, Master's Thesis, Virginia Polytechnic Institute and State University, (1989).

30 Chung, K. B., Department of Mechanical and Aerospace Engineering, Cornell University, Personal Communication (1991).

31 Stephanos, Steve, Rosemount Analytical Inc., La Habra, CA, Personal Communication (1992).

32 Incropera and DeWitt, Fundamentals of Heat and Mass Transfer, 2nd ed., John Wiley and Sons, (1985).

33 Koopmans, L. H., An Introduction to Contemporary Statistics, Duxbury Press, (1981).

34 Leonard, G., and Correa, S., *"NO_x Formation in Premixed High-Pressure Lean Methane Flames,"* Fossil Fuel Combustion Symposium 1990, ASME/PD vol. 30, S. N. Singh, ed., pp. 69-74, (1990).

35 Bendat, J. S. and Piersol, A. G., Random Data: Analysis and Measurement Procedures, 2nd ed., John Wiley and Sons, (1986).

36 Hayhurst, A. N., and Vince, I. M., *"Nitric Oxide Formation From N_2 in Flames: The Importance of 'Prompt' NO,"* Progress in Energy and Combustion Science, vol. 6, pp. 35-51, (1980).

37 Hayhurst, A. N., and Vince, I. M., *"The Origin and Nature of "Prompt" Nitric Oxide in Flames,"* Combustion and Flame, vol. 50, pp. 41-57, (1983).

38 Michaud, M. G., Westmoreland, P. R., and Feitelberg, A. S., *"Chemical Mechanisms of NO_x Formation for Gas Turbine Conditions,"* 24th Symposium (International) on Combustion, The Combustion Institute, pp. 879-887, (1992).

39 Drake, M. C., Correa, S. M., Pitz, R. W., Shyy, W., and Fenimore, C. P., *"Superequilibrium and Thermal Nitric Oxide Formation in Turbulent Diffusion Flames,"* Combustion and Flame, vol. 69, pp. 347-365, (1987).

40 Fenimore, C. P., *"Formation of Nitric Oxide in Premixed Hydrocarbon Flames,"* 13th Symposium (International) on Combustion, The Combustion Institute, pp. 373-380, (1972).

41 Iverach, D., Basden, K. S., and Kirov, N. Y., *"Formation of Nitric Oxide in Fuel-Lean and Fuel-Rich Flames,"* 14th Symposium (International) on Combustion, The Combustion Institute, pp.767-775, (1972).

42 Duterque, J., Avezard, N., and Borghi, R., *"Further Results on Nitrogen Oxides Production in Combustion Zones,"* Combustion Science and Technology, vol. 25, pp. 85-95, (1981).

43 Zabielski, M. F., Dodge, L. G., Colket III, M. B., and Seery, D. J., *"The Optical and Probe Measurement of NO: A Comparitive Study,"* 18th Symposium (International) on Combustion, The Combustion Institute, (1981).

44 Bromly, J. H., Barnes, F. J., Mandyczewsky, R., Edwards, T. J., and Haynes, B. S., *"An Experimental Investigation of the Mutually Sensitized Oxidation of Nitric Oxide and n-Butane,"* 24th Symposium (International) on Combustion, The Combustion Institute, pp. 899-907, (1992).

45 Hori, M., Matsunaga, N., Malte, P. C., and Marinov, N. M., *"The Effect of Low-Concentration Fuels on the Conversion of Nitric Oxide to Nitrogen Dioxide,"* 24th Symposium (International) on Combustion, The Combustion Institute, pp. 909-916, (1992).

46 Seery, D. J. and Zabielski, M. F., *"Comparisons Between Flame Species Measured by Probe Sampling and Optical Spectrometry Techniques,"* Combustion and Flame, vol. 78, pp. 169-177, (1989).

47 Drake, M. C. and Ratcliffe, J. W., *"Use of a Gas-Surface Chemiluminescence Analyzer for NO and NO_2 Measurements in Combustion,"* Combustion and Flame, vol. 87, pp. 152-156, (1991).

48 Jaasma, D., and Borman, G., *"Peculiarities Associated with the Measurement of Oxides of Nitrogen Produced by Diffusion Flames,"* Combustion Science and Technology, vol. 23, pp. 83-88, (1980).

49 Reynolds, W. C., STANJAN Chemical Equilibrium Solver (Computer Program), Stanford University, (1987).

50 Miller, J. A., and Bowman, C. T., *"Mechanism and Modeling of Nitrogen Chemistry in Combustion,"* Progress in Energy and Combustion Science, vol. 15, pp. 287-338, (1989).

51 Darabiha, N., Laboratoire E.M2.C, *Ecole Centrale Paris,* Personal Communication (1993).

52 Yuuki, A., and Matsui, Y., *"An Experimental Study on Flame Stability on Wire Meshes,"* Combustion Science and Technology, vol. 43, pp. 301-314, (1985).

53 Keller, J. O., and Hongo, I., *"Pulse Combustion: The Mechanisms of NO_x Combustion,"* Combustion and Flame, vol. 80, pp. 219-237, (1990).

54 Langhorne, P. J., Dowling, A. P., and Hooper, N., *"Practical Active Control System for Combustion Oscillations,"* Journal of Propulsion, vol. 6, no. 3, p. 324. (1989).

55 Yule, A. J., Taylor, D. S., and Chigier, N. A., *"Thermocouple Signal Processing and On-Line Digital Compensation,"* Journal of Energy, vol. 2, no. 4, pp. 223-231, (1978).

56 Lockwood, F. C., and Moneib, H. A., *"Fluctuating Temperature Measurements in a Heated Round Free Jet,"* Combustion Science and Technology, vol. 22, pp. 63-81, (1980).

57 Abdalla, A. Y., Bradley, D., Chin, S. B., and Lam, C., *"Temperature Fluctuations in a Jet-Stirred Reactor and Modeling Implications,"* 19th Symposium (International) on Combustion, The Combustion Institute, pp. 495-502, (1982).

58 Lenz, W., and Gunther, R., *"Measurements of Fluctuating Temperature in a Free-Jet Diffusion Flame,"* Combustion and Flame, vol. 37, pp. 63-70, (1980).

59 Chandran, S. B. S., Komerath, N. M., and Strahle, W. C., *"Scalar-Velocity Correlations in a Turbulent Premixed Flame,"* 20th Symposium (International) on Combustion, The Combustion Institute, pp. 429-435, (1984).

60 Chandran, S. B. S., Komerath, N. M., Grissom, W. M., Jagoda, J. I., and Strahle, W. C., *"Time Resolved Thermometry by Simultaneous Thermocouple and Rayleigh Scattering Measurements in a Turbulent Flame,"* Combustion Science and Technology, vol. 44, pp. 47-60, (1985).

61 Yoshida, A. and Tsuji, H., *"Measurements of Fluctuating Temperature and Velocity in a Turbulent Premixed Flame,"* 17th Symposium (International) on Combustion, The Combustion Institute, pp. 945-956, (1978).

62 Cambray, P. M., Vachon, T., Maciaszek, T., and Bellet, J. C., *"Instantaneous Compensation of Fine Wire Thermocouple Inertia in a Buoyant Turbulent Diffusion Flame,"* Proceedings of the 23rd ASME National Heat Transfer Conference, pp. 293-297, (1985).

63 Scattergood, T. R., A Dual-Junction Thermocouple Probe for Compensated Temperature Measurement in Reacting Flows, Master's Thesis, Virginia Polytechnic Institute and State University, (1992).

64 Fujii, S., Gomi, M., Eguchi, K., Yamaguchi, S., and Jin, Y., *"Time Resolved LDV and CARS Measurements in a Premixed Reacting Flow,"* Combustion Science and Technology, vol. 36, pp. 211-226, (1984).

65 Greenhalgh, D. A., Porter, F. M., and England, W. A., *"The Application of Coherent Anti-Stokes Raman Scattering to Turbulent Combustion Thermometry,"* Combustion and Flame, vol. 49, pp. 171-182, (1983).

66 Fujii, S., and Gomi, M., *"Instantaneous CARS Thermometry in Turbulent Flames,"* Combustion and Flame, vol. 48, pp. 233-240, (1982).

67 Reaney, J. E., The Use of Chemiluminescence for the Detection of Temperature and Fuel-to-Air Ratio in Turbulent Premixed Flames, Master's Thesis, Virginia Polytechnic Institute and State University, (1992).

68 Goldschmidt, V., Riley, J. F., Leonard, R. G., Wolfbrandt, G., and Baade, P., *"Transfer Function of Gas Flames: Methods of Measurement and Representative Data,"* ASHRAE Transactions, vol. 84, pp. 466-476, (1978).

69 Candel, S. M., *"Combustion Instabilities Coupled by Pressure Waves and Their Active Control,"* 24th Symposium (International) on Combustion, The Combustion Institute, (1992).

APPENDIX A THERMOCOUPLE TRANSIENT RESPONSE PROGRAM

```
*
*     DOUGLAS A. WIRTH
*     OCTOBER 1992
*
*     TCTEMP.FOR
*     THERMOCOUPLE TRANSIENT RESPONSE PROGRAM
*
*     MODELS THE TRANSIENT RESPONSE OF A 36-mil DIAMETER
*     TYPE R THERMOCOUPLE TO A STEP TEMPERATURE CHANGE.
*     (INITIALLY HOT, ALLOWED TO COOL TO ROOM TEMPERATURE)
*
*     ASSUMPTIONS:
*     [1]  CONDUCTION LOSSES NOT NEGLECTED
*     [2]  THERMOCOUPLE IS A 36-mil DIA. SPHERE
*     [3]  AMBIENT ENVIRONMENT IS AT 295 K
*     [4]  ASSUME 100% Pt FOR MATERIAL PROPERTIES
*
*     VARIABLES:
*     D1 = THERMOCOUPLE BEAD DIA. = 8.75E-4 m
*     D2 = LEAD WIRE DIA. = 2.5E-4 m
*     EMISS = EMISSIVITY OF THERMOCOUPLE BEAD, UNKNOWN
*     TEMP(i) = THERMOCOUPLE TEMPERATURE (K)
*     TW = AMBIENT TEMPERATURE = 295 K
*     TG = GAS TEMPERATURE (K)
*        TG ASSUMED EQUAL TO TW
*     RHO = THERMOCOUPLE DENSITY = 21450 kg/m^3
*     CP = THERMOCOUPLE SPECIFIC HEAT (J/kg*K)
*       CORRELATION:  CP = 124.9 + 0.0269 * T
*     NU = GAS VISCOSITY = 15.89E-06 m^2/s @ 300K
*          CORRELATION FOR 300K < TG < 1200K:
*          NU = -1.09E-5 + 6.81E-8*TG + 6.42E-11*TG**2
*     PR = PRANDTL NUMBER = 0.707 @ 300K
*          CORRELATION FOR TG < 1500K:
*          PR = 0.84 - 6.89E-4*T + 9.41E-7*TG**2
*               - 3.69E-10*TG**3
*     RAD = RAYLEIGH NUMBER BASED ON DIAMETER
*       RAD = g * ß * (TEMP(i)-TG) * D^3 / (NU * α)
*       g = ACCELERATION OF GRAVITY = 9.8 m/s^2
*       ß = BETA = 1 / TG
*       α = ALPHA = GAS THERMAL DIFFUSIVITY
```

```
*          = 22.5E-06 m^2/s @ 300K
*          CORRELATION FOR 300K < TG < 1200K:
*          ALPHA = -1.90E-5 + 1.16E-7*TG + 7.17E-11*TG**2
*      NUSSELT = NUSSELT NUMBER OF THERMOCOUPLE BEAD FOR FREE
*          CONVECTION OVER A SPHERE, USING A CORRELATION FROM
*          INCROPERA AND DEWITT, FUNDAMENTALS OF HEAT AND
*          MASS TRANSFER, 2nd ED.,
*          NUSSELT = 2.0 + 0.589*RAD^0.25 /
*                    [ 1 + (0.469/PR)^(9/16)]^(4/9)
*      NUSS2 = NUSSELT NUMBER FOR FREE CONVECTION
*          OVER A CYLINDER, USING A CORRELATION FROM
*          INCROPERA AND DEWITT, FUNDAMENTALS OF HEAT AND
*          MASS TRANSFER, 2nd ED.,
*          NUSS2 = 0.675*RAD^0.058
*      KG = GAS CONDUCTIVITY = 26.3E-03 W/m*K @ 300K
*         CORRELATION FOR 300K < TG < 1200K:
*         KG = 4.26E-3 + 8.07E-5*TG - 1.77E-8*TG**2
*      KPT = PLATINUM CONDUCTIVITY, CORRELATION FROM
*            TABULATED DATA: KPT = 70.75 - 0.00124*T
*                                  +9.19E-6 * T**2
*      DELT = TIME STEP (s)
*      SIGMA = STEPHAN-BOLTZMANN CONSTANT = 5.67E-8 W/m^2*K^4
*
*      GOVERNING EQUATION:
*
*      dTC/dt = -6/RHO/CP/D1**3 * {KG*NUSSELT*D1*(TC-TG) +
*               SIGMA*EMISS*D1**2*(TC^4 - TW^4)
*               + D2*SQRT(KPT*KG*NUSS2)*(TC-TG)}
*
*      PROCEDURE:  COMPARE EXPERIMENTAL RECORD OF THERMO-
*      COUPLE COOL-DOWN CURVE (TEMPERATURE VS. TIME) TO A
*      CALCULATED ESTIMATE OF COOL-DOWN BEHAVIOR ASSUMING
*      DIFFERENT BEAD EMISSIVITIES.  CALCULATE SUM-OF-ERRORS-
*      SQUARED AT EACH EMISSIVITY AND CHOOSE THE ONE WITH THE
*      LOWEST ERROR (i.e. BEST FIT TO EXPERIMENT) TO
*      REPRESENT THE THERMOCOUPLE EMISSIVITY.
*
       DIMENSION TIME(1000), TEMP(1000)
       CHARACTER*25 OUTFILE
       REAL*4 NU,NUSSELT,KG,NUSS2,KPT
*
*      COMPARE TO RECORD 20:  START SIMULATION AT 1200K AND
*      LET THERMOCOUPLE COOL DOWN FROM THERE, USING DIFFERENT
*      EMISSIVITIES
*
       TW4 = 295.0**4
       RHO = 21450.0
       SIGMA = 5.67E-8
```

```
      D1 = 9.0E-4
      D2 = 2.5E-4
      DELT = 0.008
      G = 9.8
*
*     START A LOOP FOR EMISSIVITY
*
      DO 50 NE = 1,9
      EMISS = NE/10.0
*     INITIALIZE TC BEAD TEMPERATURE
      TEMP(1) = 1200.0
      DO 100 I = 1,800
*     USE A FILM TEMPERATURE TO GET AIR PROPERTIES
      TFILM = (TEMP(I) + 295.0) / 2.0
      NU = -1.09E-5 + 6.81E-8*TFILM + 6.42E-11*TFILM**2
      ALPHA = -1.90E-5 + 1.16E-7*TFILM + 7.17E-11*TFILM**2
      KG = 4.26E-3 + 8.07E-5*TFILM - 1.77E-8*TFILM**2
      PR = 0.84 - 6.89E-4*TFILM + 9.41E-7*TFILM**2
     & - 3.69E-10*TFILM**3
      RAD1 = G * D1**3 / TFILM / NU / ALPHA
     & * (TEMP(I) - 295.0)
      RAD2 = G * D2**3 / TFILM / NU / ALPHA
     & * (TEMP(I) - 295.0)
      NUSSELT = 2.0 + 0.589 * RAD1**0.25 /
     & ( 1 + (0.469/PR)**(9./16.))**(4./9.)
      NUSS2 = 0.675 * RAD2**0.058
      CP = 124.9 + 0.0269 * TEMP(I)
      KPT = 10.75 - 0.00124*TEMP(I) + 9.19E-6*TEMP(I)**2
*     INCLUDE CONDUCTION LOSS THROUGH LEADS - MODELED AS
*     INFINITE-LENGTH CYLINDRICAL FINS
      COND = D2 * (TEMP(I) - 295.0) * SQRT(KG*NUSS2*KPT)
      CONV = KG * NUSSELT * D1 * (TEMP(I)-295.0)
      RAD = SIGMA * EMISS * D1**2 * (TEMP(I)**4 - TW4)
      DTDT = -6.0 / RHO / CP / D1**3 * (COND + CONV + RAD)
      TEMP(I+1) = TEMP(I) + DTDT * DELT
*     START TIME AT 1.504s TO MATCH RECORD 20 (1200K @ 1.504s)
      TIME(I) = 1.504 + (I-1)*DELT
 100  CONTINUE
      WRITE(*,55) EMISS
   55 FORMAT(/,' EMISSIVITY = ',F5.1)
      WRITE(*,20)
   20 FORMAT(/,' WHAT IS THE NAME OF THE OUTPUT FILE?')
      READ(*,25) OUTFILE
   25 FORMAT(A25)
      OPEN(5,FILE=OUTFILE,STATUS='NEW')
      DO 150 K = 1,800,10
      WRITE(5,160) TIME(K),TEMP(K)
 160  FORMAT(1X,F10.4,5X,F10.4)
```

```
150   CONTINUE
      CLOSE(5)
 50   CONTINUE
 999  STOP
      END
```

APPENDIX B THERMOCOUPLE TEMPERATURE CORRECTION PROGRAM

```
*
*     DOUGLAS A. WIRTH
*     OCTOBER 1992
*
*     TCORR.FOR
*     THERMOCOUPLE TEMPERATURE CORRECTION PROGRAM
*
*     MODELS A TYPE R THERMOCOUPLE AND PREDICTS
*     TEMPERATURE CORRECTION IN RANGE 300-2000K.
*
*     ASSUMPTIONS:
*     [1]  CONDUCTION LOSSES NOT NEGLECTED
*     [2]  THERMOCOUPLE IS A SPHERE
*     [3]  AMBIENT ENVIRONMENT IS AT 295 K
*     [4]  ASSUME 100% Pt FOR MATERIAL PROPERTIES
*
*     VARIABLES:
*     D1 = THERMOCOUPLE BEAD DIA.
*     D2 = LEAD WIRE DIA.
*     VEL = GAS VELOCITY, ASSUMED = 0.21 m/s @ STP
*     EMISS = EMISSIVITY OF THERMOCOUPLE BEAD, ASSUME = 0.3
*     TC = THERMOCOUPLE TEMPERATURE (K)
*     TW = AMBIENT TEMPERATURE = 295 K
*     TG = GAS TEMPERATURE (K)
*     CP = THERMOCOUPLE SPECIFIC HEAT (J/kg*K)
*       CORRELATION:  CP = 124.9 + 0.0269 * T
*     NU = GAS VISCOSITY = 15.89E-06 m^2/s @ 300K
*       CORRELATION FOR 300K < TG < 2200K:
*       NU = -6.77E-6 + 5.50E-8*TG + 7.31E-11*TG**2
*     PR = PRANDTL NUMBER = 0.707 @ 300K
*       CORRELATION FOR TG < 1500K:
*       PR = 0.84 - 6.89E-4*T + 9.41E-7*TG**2
*         - 3.69E-10*TG**3
*     RED1 = REYNOLD'S NUMBER BASED ON BEAD DIAMETER
*       = 0.21 * D1 * TG / NU / 273.0
*     RED2 = REYNOLD'S NUMBER BASED ON LEAD DIAMETER
*       = 0.21 * D2 * TG / NU / 273.0
*       (ACCOUNTS FOR ACCELERATION OF GASES WITH TEMP.)
*     NUSSELT = NUSSELT NUMBER OF THERMOCOUPLE BEAD FOR
*       FORCED CONVECTION OVER A SPHERE, USING A
*       CORRELATION FROM INCROPERA AND DEWITT,
*       FUNDAMENTALS OF HEAT AND MASS TRANSFER, 2nd ED.,
*       NUSSELT = 2.0 + PR**0.4 * (0.4*SQRT(RED1) +
```

```
*              0.06*RED1**0.66667)
*      NUSS2 = NUSSELT NUMBER FOR FORCED CONVECTION
*        OVER A CYLINDER, USING A CORRELATION FROM
*        INCROPERA AND DEWITT, FUNDAMENTALS OF HEAT AND
*        MASS TRANSFER, 2nd ED.,
*       NUSS2 = 0.3 + 0.62 * SQRT(RED2) * PR**0.3333*
*          ((RED2 / 282000.0)**0.625 + 1.0)**0.8 /
*          ((0.4/PR)**0.6667 + 1.0)**0.25
*      KG = GAS CONDUCTIVITY = 26.3E-03 W/m*K @ 300K
*        CORRELATION FOR 300K < TG < 2200K:
*        KG = 4.83E-3 + 8.45E-5*TG - 3.48E-8*TG**2
*             + 1.29E-11*TG**3
*      KPT = PLATINUM CONDUCTIVITY, CORRELATION FROM
*         TABULATED DATA: KPT = 70.75 - 0.00124*T
*                         +9.19E-6 * T**2
*      SIGMA = STEPHAN-BOLTZMANN CONSTANT = 5.67E-8 W/m^2*K^4
*
*      GOVERNING EQUATION:
*
*      dTC/dt = 0 = (KG*NUSSELT*D1)*(TG-TC) -
*            SIGMA*EMISS*D1**2*(TC**4 - TW**4)
*            + D2*SQRT(KPT*KG*NUSS2)*(TFIN-TC)}
*
       IMPLICIT DOUBLE PRECISION (A-H,O-Z)
       REAL*8 NU,NUSSELT,KG,NUSS2,KPT
       DIMENSION TIME(1000), TEMP(1000), DBEAD(3), DLEAD(3)
       CHARACTER*25 OUTFILE
       EMISS = 0.3
       TW4 = 300.0**4
       SIGMA = 5.67E-8
*      DATA FOR LARGE THERMOCOUPLE:
       DBEAD(1) = 9.16E-4
       DLEAD(1) = 2.54E-4
*      DATA FOR FINE THERMOCOUPLE #1:
       DBEAD(2) = 1.60E-4
       DLEAD(2) = 2.54E-5
*      DATA FOR FINE THERMOCOUPLE #2:
       DBEAD(3) = 1.75E-4
       DLEAD(3) = 2.54E-5
*
*      LOOP THROUGH THERMOCOUPLE CASES
*
       DO 1000 K = 1,3
       D1 = DBEAD(K)
       D2 = DLEAD(K)
       WRITE(*,20)
   20  FORMAT(/,' WHAT IS THE NAME OF THE OUTPUT FILE?')
       WRITE(*,22) DBEAD(K)
```

```
   22 FORMAT(' BEAD DIA. = ',E10.4,' m')
      READ(*,25) OUTFILE
   25 FORMAT(A25)
      OPEN(5,FILE=OUTFILE,STATUS='NEW')
      WRITE(*,35)
  35  FORMAT('       TC     /   TG-TC    /  TFIN')
*
*     LOOP THROUGH THERMOCOUPLE TEMPERATURES
*
      DO 100 I = 5,20
      TC = FLOAT(I)*100.0
*     INITIALIZE GUESSES FOR TFIN AND TG
      TFIN = TC / 2.0
      TG = TC
      DT = 10.0
 300  CONTINUE
*     ITERATE 5 TIMES TO FIND TG
      DO 221 J=1,5
      TFILM = (TG + TFIN) / 2.0
      IF(TFILM.LT.1483.56) PR=.8418 - 6.89E-4*TFILM
     & + 9.407E-07*TFILM**2 - 3.692E-10*TFILM**3
      IF(TFILM.GE.1483.56) PR=.4207 + .0003594*TFILM
     & - 1.37E-07*TFILM**2 + 1.01E-11*TFILM**3
      NU = -6.77E-6 + 5.50E-8*TFILM + 7.31E-11*TFILM**2
      RED2 = 0.21 * D2 * TFILM / NU / 273.0
      NUSS2 = 0.3 + 0.62 * SQRT(RED2) * PR**0.3333*
     & ((RED2 / 282000.0)**0.625 + 1.0)**0.8 /
     & ((0.4/PR)**0.6667 + 1.0)**0.25
      CP = 124.9 + 0.0269 * TC
      KG = 4.83E-3 + 8.45E-5*TG - 3.48E-8*TG**2
     &       + 1.29E-11*TG**3
      A = D2 * EMISS * SIGMA / KG / NUSS2
      TG = TFIN + A*(TFIN**4 - TW4)
      IF(TG.LT.TC) TG = TC
*      WRITE(*,*) TG
 221  CONTINUE
*      WRITE(*,*) ' ONE'
*     CALCULATE PROPERTIES USING FILM TEMPERATURES.
      TFILM = (TG + TC) / 2.0
      IF(TFILM.LT.1483.56) PR=.8418 - 6.89E-4*TFILM
     & + 9.407E-07*TFILM**2 - 3.692E-10*TFILM**3
      IF(TFILM.GE.1483.56) PR=.4207 + .0003594*TFILM
     & - 1.37E-07*TFILM**2 + 1.01E-11*TFILM**3
      NU = -6.77E-6 + 5.50E-8*TFILM + 7.31E-11*TFILM**2
      RED1 = 0.21 * D1 * TFILM / NU / 273.0
      NUSSELT = 2.0 + PR**0.4 * (0.4*SQRT(RED1) +
     &         0.06*RED1**0.66667)
      CP = 124.9 + 0.0269 * TC
```

```
      KPT = 70.75 - 0.00124*TC + 9.19E-6*TC**2
      CONV = D1 * KG * NUSSELT * (TG - TC)
      COND = D2 * SQRT(KPT*NUSS2*KG) * (TFIN - TC)
      RAD = D1**2 * EMISS * SIGMA * (TW4 - TC**4)
      F1 = CONV + COND + RAD
      WRITE(*,*) ' F1 = ', F1
*     INCREMENT TFIN
 350  TFIN = TFIN + DT
*     ITERATE 5 TIMES TO FIND TG
      DO 222 J=1,5
      TFILM = (TG + TFIN) / 2.0
      IF(TFILM.LT.1483.56) PR=.8418 - 6.89E-4*TFILM
     & + 9.407E-07*TFILM**2 - 3.692E-10*TFILM**3
      IF(TFILM.GE.1483.56) PR=.4207 + .0003594*TFILM
     & - 1.37E-07*TFILM**2 + 1.01E-11*TFILM**3
      NU = -6.77E-6 + 5.50E-8*TFILM + 7.31E-11*TFILM**2
      RED2 = 0.21 * D2 * TFILM / NU / 273.0
      NUSS2 = 0.3 + 0.62 * SQRT(RED2) * PR**0.3333*
     & ((RED2 / 282000.0)**0.625 + 1.0)**0.8 /
     & ((0.4/PR)**0.6667 + 1.0)**0.25
      KG = 4.83E-3 + 8.45E-5*TG - 3.48E-8*TG**2
     &       + 1.29E-11*TG**3
      A = D2 * EMISS * SIGMA / KG / NUSS2
      TG = TFIN + A*(TFIN**4 - TW4)
      IF(TG.LT.TC) TG = TC
*      WRITE(*,*) TG
 222  CONTINUE
*      WRITE(*,*) ' TWO'
*     EVALUATE PROPERTIES AT THE FILM TEMPERATURES.
      TFILM = (TG + TC) / 2.0
      IF(TFILM.LT.1483.56) PR=.8418 - 6.89E-4*TFILM
     & + 9.407E-07*TFILM**2 - 3.692E-10*TFILM**3
      IF(TFILM.GE.1483.56) PR=.4207 + .0003594*TFILM
     & - 1.37E-07*TFILM**2 + 1.01E-11*TFILM**3
      NU = -6.77E-6 + 5.50E-8*TFILM + 7.31E-11*TFILM**2
      RED1 = 0.21 * D1 * TFILM / NU / 273.0
      NUSSELT = 2.0 + PR**0.4 * (0.4*SQRT(RED1) +
     &         0.06*RED1**0.66667)
      CP = 124.9 + 0.0269 * TC
      KPT = 70.75 - 0.00124*TC + 9.19E-6*TC**2
      CONV = D1 * KG * NUSSELT * (TG - TC)
      COND = D2 * SQRT(KPT*NUSS2*KG) * (TFIN - TC)
      RAD = D1**2 * EMISS * SIGMA * (TW4 - TC**4)
      F2 = CONV + COND + RAD
      WRITE(*,*) ' F2 = ', F2
*
*     CHECK WHETHER THE FUNCTION F HAS CHANGED SIGN, TO
*     SEE WHETHER THE SOLUTION HAS BEEN PASSED.
```

```
*
      IF(ABS(F1).LE.1.0D-8.OR.ABS(F2).LE.1.0D-8) THEN
*      IF(ABS(DT).LE.0.05) THEN
*        ESCAPE FROM THE LOOP
         GOTO 150
      ENDIF
      IF(F1*F2.GT.0.0D0) THEN
*        NO CHANGE OF SIGN: KEEP LOOKING
         F1 = F2
         GOTO 350
      ENDIF
      IF(F1*F2.LE.0.0D0) THEN
*        CHANGE OF SIGN: GO BACK ONE STEP, AND START
*        INCREMENTING BY SMALLER STEPS.
         TFIN = TFIN - DT
         DT = DT / 10.0
         GOTO 300
      ENDIF
 150  CONTINUE
      WRITE(5,160) TC,TG-TC,TFIN
      WRITE(*,160) TC,TG-TC,TFIN
      WRITE(5,155) CONV,COND,RAD,CONV+COND+RAD
 155  FORMAT(' CONV = ',E10.4,/,' COND = ',E10.4,/,' RAD =  ',
     & E10.4,/,' SUM =  ',E10.4)
 160  FORMAT(3(1X,F10.2))
 100  CONTINUE
      CLOSE(5)
 1000 CONTINUE
 999  STOP
      END
```

APPENDIX C SPATIAL EQUIVALENCE RATIO DISTRIBUTIONS

Table 7 lists the equivalence ratio measurements for experiments 80, 81, 82, and 83. While experiment 80 was not a steady spatially nonuniform flame, the data is presented here because it was the only pulsing flame where the spatial equivalence ratio was measured. The x and y coordinates are the probe locations over the flameholder, where the origin is the axis of the burner. Table 8 lists the equivalence ratio measurements for experiments 84, 87a, and 87b.

Table 7 Spatial Equivalence Ratio Distributions for Experiments 80, 81, 82, and 83

X (mm)	Y (mm)	EXP. 80	EXP. 81	EXP. 82	EXP. 83
0.00	0.00	0.69	1.02	0.79	0.80
4.00	0.00	0.73	1.12	0.90	1.02
8.00	0.00	0.78	1.23	0.90	1.20
2.83	2.83	0.75	1.05	0.83	1.02
5.66	5.66	0.78	1.11	0.81	1.17
0.00	4.00	0.76	0.97	0.79	0.85
0.00	8.00	0.81	0.94	0.77	0.84
-2.83	2.83	0.72	0.94	0.77	0.75
-5.66	5.66	0.76	0.92	0.76	0.68
-4.00	0.00	0.69	0.95	0.76	0.69
-8.00	0.00	0.72	0.93	0.75	0.66
-2.83	-2.83	0.67	0.94	0.76	0.72
-5.66	-5.66	0.70	0.92	0.75	0.67
0.00	-4.00	0.70	0.99	0.78	0.76
0.00	-8.00	0.75	0.94	0.76	0.71
2.83	-2.83	0.71	1.04	0.81	0.88
5.66	-5.66	0.75	1.01	0.80	1.14

Table 8 Spatial Equivalence Ratio Distributions for Experiments 84, 87a, and 87b

X (mm)	Y (mm)	EXP. 84	EXP. 87a	EXP. 87b
0.00	0.00	0.71	0.76	0.75
4.00	0.00	0.80	0.90	0.87
8.00	0.00	0.79	1.01	0.90
2.83	2.83	0.75	0.92	0.83
5.66	5.66	0.71	0.95	0.82
0.00	4.00	0.67	0.84	0.74
0.00	8.00	0.68	0.83	0.73
-2.83	2.83	0.68	0.73	0.69
-5.66	5.66	0.67	0.70	0.67
-4.00	0.00	0.68	0.69	0.68
-8.00	0.00	0.67	0.67	0.66
-2.83	-2.83	0.68	0.69	0.79
-5.66	-5.66	0.67	0.68	0.66
0.00	-4.00	0.70	0.72	0.71
0.00	-8.00	0.68	0.69	0.67
2.83	-2.83	0.77	0.79	0.68
5.66	-5.66	0.74	0.77	0.73

APPENDIX D TEMPERATURE EXTRAPOLATION PROGRAM

```
*
*     PROGRAM TEMP.FOR
*
*     DOUGLAS A. WIRTH
*     FEBRUARY 1993
*
*     PROGRAM CONVERTS A DATA FILE WITH THERMOCOUPLE
*     VOLTAGES INTO TEMPERATURES, CALCULATES THE MEAN
*     AND THE PROBABILITY DENSITY FUNCTION (pdf) OF THE
*     DISTRIBUTION.
*
*     THERE ARE 200 DATA POINTS, IN THE 5th COLUMN
*     OF THE DATA FILE.  THE AMPLIFIER GAIN WAS 52.
*
      IMPLICIT DOUBLE PRECISION (A-H,O-Z), INTEGER (I-N)
      DIMENSIONTEMP(200),TI(200),TR(200),GTT(200),KOUNT(20),
     & APRIME(51),A(3),B(3),C(3)
*
*     TEMP = TEMPERATURE
*     TI AND TR = IMAGINARY AND REAL COMPONENTS OF THE DFT
*     GTT = AUTOSPECTRUM COMPONENTS
*     KOUNT = SUM MAINTAINED FOR pdf FUNCTION
*     APRIME = THERMOCOUPLE AMPLITUDE RESPONSE
*     A, B, AND C ARE COEFFICIENTS FOR THE TEMPERATURE
*             CORRECTIONS.
      CHARACTER*30 INFILE, OUTFILE
*     COEFFICIENTS FOR 6.3 mil THERMOCOUPLE
      A(1) = 14.9
      B(1) = -5.15E-02
      C(1) = 5.08E-05
*     COEFFICIENTS FOR 6.9 mil THERMOCOUPLE
      A(2) = 15.7
      B(2) = -5.43E-02
      C(2) = 5.35E-05
*     COEFFICIENTS FOR 36 mil THERMOCOUPLE
      A(3) = 18.3
      B(3) = -0.122
      C(3) = 1.765E-04
      WRITE(*,5)
    5 FORMAT (' WHAT IS THE NAME OF THE DATA FILE?')
```

```
      READ(*,7) INFILE
    7 FORMAT(A30)
      OPEN(5,FILE=INFILE,STATUS='OLD')
*      OPEN(5,FILE='B:\77\MX_19_77.DAT',STATUS='OLD')
*      OPEN(5,FILE='B:\70\MX_17_70.DAT',STATUS='OLD')
      TMIN = 10000.
      TMAX = -1000.
      TMEAN = 0.0
*
*     APPLY A CORRECTION TO ACCOUNT FOR RADIATION AND
*     CONDUCTION LOSSES.  THIS IS A DC SHIFT.
*
   49 WRITE(*,57)
   57 FORMAT(' ENTER A [1] FOR 6.3 mil TC DIAMETER,',/,
     & ' ENTER A [2] FOR 6.9 mil TC DIAMETER:',/,
     & ' ENTER A [3] FOR 36 mil TC DIAMETER:')
      READ(*,59) ND
   59 FORMAT(I1)
      IF(ND.EQ.1) D1 = 1.60E-4
      IF(ND.EQ.2) D1 = 1.753E-4
      IF(ND.EQ.3) D1 = 9.14E-4
      IF(D1.EQ.0.0) GOTO 49
*
*     READ IN THERMOCOUPLE VOLTAGES AND CONVERT TO RAW
*     TEMPERATURES.
*
      DO 100 I = 1,200
      READ(5,*) D,D,D,D,TEMP(I)
*     CONVERT TO THE ORIGINAL MILLIVOLTS
      V = TEMP(I) / 52.0 * 1000.0
*     USE A FOUR-PIECE CURVE FIT TO THE DATA FOR TYPE R
*     THERMOCOUPLES FROM OMEGA HANDBOOK.
      IF(V.LT.5.0) TC = 8.886 + 135.5*V - 5.719*V**2
      IF((V.GE.5.0).AND.(V.LE.10.0)) TC = 68.56 + 102.7*V
     & - 1.337*V**2
      IF((V.GE.10.0).AND.(V.LE.15.0)) TC = 149.0 + 86.90*V
     & - 0.5606*V**2
      IF(V.GE.15.0) TC = 328.5 + 62.94*V + 0.2413*V**2
*     NOW CONVERT FROM CENTIGRADE TO KELVIN
*     AND ADD TEMPERATURE CORRECTION
      TEMP(I) = TC + 273.0
      TCORR = A(ND) + B(ND)*TEMP(I) + C(ND)*TEMP(I)**2
      TEMP(I) = TEMP(I) + TCORR
      TMEAN = TMEAN + TEMP(I)
      IF(TEMP(I).GE.TMAX) TMAX = TEMP(I)
      IF(TEMP(I).LE.TMIN) TMIN = TEMP(I)
  100 CONTINUE
      CLOSE(5)
```

```
*
*     SAVE THE ORIGINAL RAW TEMPERATURES
*
      OPEN(5,FILE='OLDTEMP.DAT',STATUS='NEW')
      DO 235 I = 1, 200
      WRITE(5,345) FLOAT(I-1)/50.0, TEMP(I)
 235  CONTINUE
      CLOSE(5)
      TMEAN = TMEAN / 200.0
*
*     TMEAN NOW REPRESENTS THE MEAN TEMPERATURE.
*
      WRITE(*,142) TMEAN,TMIN,TMAX
  142 FORMAT(' THE MEAN TEMPERATURE IS ',F10.2,' K.',/,
     & ' TMIN = ',F7.2,/,' TMAX = ',F7.2)
*     JUMP OUT OF PROGRAM IF ALL YOU WERE INTERESTED IN WAS
*     THE MEAN TEMPERATURE.  (i.e. FOR LARGE TC)
      IF(ND.EQ.3) GOTO 999
*
*     CALCULATE THE DFT AND AUTOSPECTRUM OF THE TEMPERATURE
*     RECORD.  THE DATA WAS COLLECTED AT 50 Hz FOR 4 SECONDS
*     (200 POINTS), FOR A SPECTRAL RESOLUTION OF 0.25 Hz.
*     CALCULATE ONLY THE FIRST 50 COMPONENTS.
*
      N = 200
*     MAKE TEMP(I) A ZERO-MEAN RECORD.
      DO 250 I = 1,N
      TEMP(I) = TEMP(I)-TMEAN
 250  CONTINUE
      CALL DFT(N,TEMP,TR,TI,GTT)
*
*     SAVE THE DFT COMPONENTS AND AUTOSPECTRUM TO A FILE
*
      OPEN(6,FILE='GTT.DAT',STATUS='NEW')
      DO 300 M = 1,51
*      WRITE(6,310) M-1,TR(M),TI(M),GTT(M)
* 310  FORMAT(1X,I2,1X,E12.6,1X,E12.6,1X,E12.6)
      WRITE(6,310) 0.25*(M-1),GTT(M)
 310  FORMAT(1X,F7.3,1X,E12.6)
 300  CONTINUE
      CLOSE(6)
*
*     NOW THAT THE COMPONENTS ARE KNOWN, CORRECT FOR THE
*     THERMOCOUPLE'S INABILITY TO RESPOND FULLY AT ALL
*     FREQUENCIES.  DIVIDE THE SPECTRAL COMPONENTS BY A',
*     THE AMPLITUDE RESPONSE OF THE THERMOCOUPLE.  THE A'
*     DATA COMES FROM THE SUBPROGRAM TCRESP.
*
```

```
      CALL TCRESP(D1,TMEAN,APRIME)
  3   CONTINUE
*
*     THE AMPLITUDE OF THE TEMPERATURE FLUCTUATION NEEDS TO
*     BE EXTRAPOLATED BACK TO THE FLAME ZONE FROM ITS LAST
*     MEASURED POSITION.  READ IN THE AMPLIFICATION, AND
*     MULTIPLY ALL SPECTRAL COMPONENTS BY THIS NUMBER.
*
      WRITE(*,37)
  37  FORMAT(' WHAT IS THE EXTRAPOLATION FACTOR?')
      READ(*,39) EFAC
  39  FORMAT(F10.5)
      WRITE(*,41) EFAC
  41  FORMAT(' THE EXTRAPOLATION FACTOR IS ',F10.5)
      DO 299 M = 1,51
      TR(M) = TR(M) * EFAC / APRIME(M)
      TI(M) = TI(M) * EFAC / APRIME(M)
      GTT(M) = TR(M)**2 + TI(M)**2
 299  CONTINUE
*
*     SAVE THE NEW DFT COMPONENTS AND AUTOSPECTRUM TO A FILE
*
      OPEN(6,FILE='GTTPRIME.DAT',STATUS='NEW')
      DO 301 M = 1,51
*      WRITE(6,310) M-1,TR(M),TI(M),GTT(M)
* 310  FORMAT(1X,I2,1X,E12.6,1X,E12.6,1X,E12.6)
      WRITE(6,311) 0.25*(M-1),GTT(M)
 311  FORMAT(1X,F7.3,1X,E12.6)
 301  CONTINUE
      CLOSE(6)
*
*     GO BACK AND REBUILD THE TEMPERATURE RECORD ACCORDING
*     TO THE MODIFIED SPECTRAL COMPONENTS.
*
      TMIN = 10000.
      TMAX = -1000.
      PI2 = 6.283185307
      DO 400 I=1,N
      SUMR = 0.0
      SUMI = 0.0
      DO 450 M=1,51
      X = PI2*(M-1)*(I-1)/N
      SUMR = SUMR + TR(M)*COS(X)
      SUMI = SUMI + TI(M)*SIN(X)
 450  CONTINUE
      TEMP(I) = SUMR + SUMI + TMEAN
      IF(TEMP(I).GE.TMAX) TMAX = TEMP(I)
      IF(TEMP(I).LE.TMIN) TMIN = TEMP(I)
```

```
 400  CONTINUE
      WRITE(*,142) TMEAN,TMIN,TMAX
*
*     SAVE THE NEW TEMPERATURE DATA
*
      OPEN(5,FILE='NEWTEMP.DAT',STATUS='NEW')
      DO 234 I = 1, 200
      WRITE(5,345) FLOAT(I-1)/50.0, TEMP(I)
 234  CONTINUE
 345  FORMAT(1X,F5.3,3X,F7.2)
      CLOSE(5)
*
*     CALCULATE THE pdf
*
*      WRITE(*,*) ' CALLING SUBROUTINE PDF'
      CALL PDF(TMIN,TMAX,TEMP,KOUNT,BIN)
*      WRITE(*,*) ' BACK TO MAIN PROGRAM'
*      WRITE(*,*) ' BIN = ', BIN
*     STORE THE COEFFICIENTS OF THE pdf IN KOUNT.DAT
      OPEN(7,FILE='KOUNT.DAT',STATUS='NEW')
      DO 97 K=1,20
      WRITE(7,99) TMIN+BIN*(K-1), KOUNT(K)/200.0
  97  CONTINUE
  99  FORMAT(3X,F10.1,3X,F10.5)
      CLOSE(7)
      WRITE(*,*) ' END OF PROGRAM.'
 999  STOP
      END
*
*************************************************************
*
       SUBROUTINE DFT(N,X,XR,XI,GXX)
*
*     CALCULATE THE DFT AND AUTOSPECTRUM -
*     BASED ON PRIOR EXPERIENCE, ONLY FIRST 50
*     COMPONENTS ARE NEEDED.
*
      IMPLICIT DOUBLE PRECISION (A-H,O-Z), INTEGER (I-N)
      DIMENSION X(200),XR(200),XI(200),GXX(200)
*
*     X IS THE INPUT WAVEFORM [X(t)]
*     XR(m) IS THE REAL PART OF THE DFT COMPONENTS
*     XI(m) IS THE IMAGINARY PART OF THE DFT COMPONENTS
*     GXX(m) IS THE AUTOSPECTRUM OF X(t).
*
*     COMMON STATEMENT FOR OTHER WAYS OF CALLING SUBROUTINE
*      COMMON / PARAM / X,XR,XI,GXX
      PARAMETER (PI = 3.14159)
```

```
      DO 200 M = 1,51
*
*     M IS AN INDEX THAT SHOULD REALLY RUN FROM 0 TO 50,
*     BUT THE ARRAYS CANNOT HAVE AN INDEX OF ZERO.
*
      SUMR = 0.0
      SUMI = 0.0
      DO 250 I = 1,N
      SUMR = SUMR + X(I) * COS(2. * PI * (M-1) * (I-1) / N)
      SUMI = SUMI + X(I) * SIN(2. * PI * (M-1) * (I-1) / N)
 250  CONTINUE
*
*     MULTIPLY COMPONENTS BY TWO FOR A ONE-SIDED TRANSFORM
*
      XR(M) = SUMR * 2.0 / N
      XI(M) = SUMI * 2.0 / N
      GXX(M) = XR(M)**2 + XI(M)**2
 200  CONTINUE
*
*     EXCEPT FOR THE FIRST COMPONENT, WHICH SHOULD NOT BE
*     MULTIPLIED BY TWO.
*
      XR(1) = XR(1) / 2.0
      XI(1) = XI(1) / 2.0
      GXX(1) = XR(1)**2 + XI(1)**2
      RETURN
      STOP
      END
*
*************************************************************
*
      SUBROUTINE TCRESP(D1,T,APRIME)
*     THERMOCOUPLE TRANSIENT RESPONSE PROGRAM
*
*     MODELS THE TRANSIENT RESPONSE OF A 6.3-mil OR 6.9-mil
*    DIAMETER TYPE R THERMOCOUPLE TO A SINUSOIDAL TEMPERATURE
*     INPUT.
*
*     ASSUMPTIONS:
*     [1]  CONDUCTION LOSSES NOT NEGLECTED
*     [2]  THERMOCOUPLE IS A SPHERE
*     [3]  AMBIENT ENVIRONMENT IS AT 295 K
*     [4]  ASSUME 100% Pt FOR MATERIAL PROPERTIES
*
*     VARIABLES:
*     D1 = THERMOCOUPLE BEAD DIA. = 1.60E-4 m (6.3 mil)
*                                OR = 1.753E-4 m (6.9 mil)
*     D2 = LEAD WIRE DIA. = 2.5E-5 m
```

```
*      VEL = GAS VELOCITY, ASSUMED = 0.21 m/s @ STP
*      EMISS = EMISSIVITY OF THERMOCOUPLE BEAD, ASSUME = 0.3
*      TC = THERMOCOUPLE TEMPERATURE (K)
*      TW = AMBIENT TEMPERATURE = 295 K
*      TG = GAS TEMPERATURE (K)
*      RHO = THERMOCOUPLE DENSITY = 21450 kg/m^3
*      CP = THERMOCOUPLE SPECIFIC HEAT (J/kg*K)
*        CORRELATION:  CP = 124.9 + 0.0269 * T
*      NU = GAS VISCOSITY = 15.89E-06 m^2/s @ 300K
*           CORRELATION FOR 300K < TG < 2200K:
*           NU = -6.77E-6 + 5.50E-8*TG + 7.31E-11*TG**2
*      PR = PRANDTL NUMBER; CORRELATION FROM TABULATED DATA:
*        FOR T<1500K, PR = 0.8418 - 6.894E-4*TG
*                   + 9.407E-7*TG^2 - 3.692E-10*TG^3
*        FOR T>1500K, PR = 0.4207 + 3.594E-4*TG
*                   - 1.370E-7*TG^2 + 1.010E-11*TG^3
*      RED1 = REYNOLD'S NUMBER BASED ON BEAD DIAMETER
*           = 0.21 * D1 * TG / NU / 273.0
*      RED2 = REYNOLD'S NUMBER BASED ON LEAD DIAMETER
*           = 0.21 * D2 * TG / NU / 273.0
*           (ACCOUNTS FOR ACCELERATION OF GASES WITH TEMP.)
*      NUSSELT = NUSSELT NUMBER OF THERMOCOUPLE BEAD FOR
*          FORCED CONVECTION OVER A SPHERE, USING A
*          CORRELATION FROM INCROPERA AND DEWITT,
*          FUNDAMENTALS OF HEAT AND MASS TRANSFER, 2nd ED.,
*          NUSSELT = 2.0 + PR**0.4 * (0.4*SQRT(RED1) +
*                    0.06*RED1**0.66667)
*      NUSS2 = NUSSELT NUMBER FOR FORCED CONVECTION
*          OVER A CYLINDER, USING A CORRELATION FROM
*          INCROPERA AND DEWITT, FUNDAMENTALS OF HEAT AND
*          MASS TRANSFER, 2nd ED.,
*          NUSS2 = 0.989 * RED2**0.330 * PR**0.333
*      KG = GAS CONDUCTIVITY = 26.3E-03 W/m*K @ 300K
*          CORRELATION FOR 300K < TG < 2200K:
*          KG = 4.83E-3 + 8.45E-5*TG - 3.48E-8*TG**2
*               + 1.29E-11*TG**3
*      KPT = PLATINUM CONDUCTIVITY, CORRELATION FROM
*            TABULATED DATA: KPT = 70.75 - 0.00124*T
*                                  +9.19E-6 * T**2
*      SIGMA = STEPHAN-BOLTZMANN CONSTANT = 5.67E-8 W/m^2*K^4
*      DT = TIME STEP (s)
*
*      GOVERNING EQUATION:
*
*      dTC/dt = 6/RHO/CP*{(KG*NUSSELT*D1**2)*(TG-TC) -
*               SIGMA*EMISS/D1*(TC**4 - TW**4)
*               + D2*SQRT(KPT*KG*NUSS2)/D1**3*(TFIN-TC)}
*
```

```
*       IN THIS PROGRAM I HAVE ASSUMED THAT TFIN = TG
*
        IMPLICIT DOUBLE PRECISION (A-H,O-Z), INTEGER (I-N)
        DIMENSION TG(2002), TC(2002), APRIME(51)
        CHARACTER*25 OUTFILE
        REAL*4 NU,NUSSELT,KG
    7   FORMAT(F10.4)
*        WRITE(*,10)
*   10   FORMAT(/,' WHAT IS THE AMPLITUDE OF THE
      & TEMP. FLUCTUATION?')
*        READ(*,7) A
         A = 10.0
*        WRITE(*,20)
*   20 FORMAT(/,' WHAT IS THE NAME OF THE DATA FILE?')
*        READ(*,25) OUTFILE
*   25 FORMAT(A25)
*        OPEN(5,FILE=OUTFILE,STATUS='NEW')
        OPEN(6,FILE='TCRESP.OUT',STATUS='NEW')
*        WRITE(5,45) T,A
        WRITE(6,45) T,A
   45 FORMAT(' MEAN TEMPERATURE = ',F10.0,/,
      & ' AMPLITUDE =',F10.0,/)
        WRITE(6,47)
   47 FORMAT(' FREQ. (Hz)   APRIME   PHASE (DEGREES)
      &  TMEAN / T')
*   49 WRITE(*,57)
*   57 FORMAT(' ENTER A [1] FOR 6.3 mil TC DIAMETER,',/,
*      & ' ENTER A [2] FOR 6.9 mil TC DIAMETER:')
*        READ(*,59) ND
*   59 FORMAT(I1)
*        IF(ND.EQ.1) D1 = 1.60E-4
*        IF(ND.EQ.2) D1 = 1.753E-4
*        IF(D1.EQ.0.0) GOTO 49
*
*      RUN THE SIMULATION FOR 10 CYCLES, IRES POINTS PER CYCLE
*      INITIAL CONDITION : TC = T, THE MEAN TEMPERATURE
*
        TC(1) = T
        TW4 = 295.0**4
        RHO = 21450.0
        SIGMA = 5.67E-8
        EMISS = 0.3
        D2 = 2.5E-5
        DELT = 0.0
*       IRES AND RES GIVE THE RESOLUTION OF THE PROGRAM;
*       A SINGLE SINUSOIDAL CYCLE IS DIVIDED INTO IRES
*       INCREMENTS, SO THE LARGER IRES THE SMALLER THE
*       TIME STEP.
```

```
      IRES = 200
      RES = 200.0
*
*     PROGRAM CALCULATES THERMOCOUPLE RESPONSE AT 50
*     FREQUENCIES, CORRESPONDING TO THE 50 DFT COMPONENTS;
*     SPECTRAL RESOLUTION IS 0.25 Hz.
      DO 299 K=1,51
      F = 0.25*(K-1)
*      WRITE(*,40) F
*      WRITE(5,40) F
   40 FORMAT(' FREQ (Hz) = ',F10.4)
*     DT IS A TIME STEP.  DT IS SCALED SO THAT IRES TIME
*     STEPS WILL OCCUR PER CYCLE, REGARDLESS OF FREQUENCY.
*     FREQ = 0.0 IS A SPECIAL CASE.
      IF(F.GT.0.0) DT = 1.0 / RES / F
      IF(F.EQ.0.0) DT = 0.01
      DO 99 I=1,IRES*10+1
*     TG = T + A * SIN (2*PI*F*TIME); TIME = (I-1)/(IRES*F)
      TG(I) = T + A * SIN (6.283185 * (I-1) / RES)
      IF(F.EQ.0.0) TG(I) = T
*     EVALUATE PROPERTIES AT TFILM
      TFILM = (TG(I) + TC(I)) / 2.0
      IF(TFILM.LT.1483.56) PR=.8418 - 6.89E-4*TFILM
     & + 9.407E-07*TFILM**2 - 3.692E-10*TFILM**3
      IF(TFILM.GE.1483.56) PR=.4207 + .0003594*TFILM
     & - 1.37E-07*TFILM**2 + 1.01E-11*TFILM**3
      NU = -6.77E-6 + 5.50E-8*TFILM + 7.31E-11*TFILM**2
      RED1 = 0.21 * D1 * TFILM / NU / 273.0
      NUSSELT = 2.0 + PR**0.4 * (0.4*SQRT(RED1) +
     &          0.06*RED1**0.66667)
*     GET OTHER PROPERTIES AT THE GAS TEMPERATURE
*     (ASSUME TFIN = TG)
      TFILM = TG(I)
      IF(TFILM.LT.1483.56) PR=.8418 - 6.89E-4*TFILM
     & + 9.407E-07*TFILM**2 - 3.692E-10*TFILM**3
      IF(TFILM.GE.1483.56) PR=.4207 + .0003594*TFILM
     & - 1.37E-07*TFILM**2 + 1.01E-11*TFILM**3
      NU = -6.77E-6 + 5.50E-8*TFILM + 7.31E-11*TFILM**2
      RED2 = 0.21 * D2 * TFILM / NU / 273.0
      NUSS2 = 0.989 * RED2**0.330 * PR**0.333
      CP = 124.9 + 0.0269 * TC(I)
      KG = 4.83E-3 + 8.45E-5*TG(I) - 3.48E-8*TG(I)**2
     &     + 1.29E-11*TG(I)**3
      KPT = 70.75 - 0.00124*TC(I) + 9.19E-6*TC(I)**2
*     CALCULATE dTC/dt
      RAD = -SIGMA*EMISS*(TC(I)**4 - TW4)
      COND = D2*SQRT(KPT*KG*NUSS2)/D1**2*(TG(I)-TC(I))
      CONV = KG*NUSSELT/D1*(TG(I)-TC(I))
```

```
      DTDT = 6.0/RHO/CP/D1*(RAD + COND + CONV)
      DELT = DTDT * DT
      TC(I+1) = TC(I) + DELT
   99 CONTINUE
*     CALCULATED THERMOCOUPLE TEMPERATURE FOR PAST 20 CYCLES.
*     NOW FIND THE AMPLITUDE OF THE THERMOCOUPLE FLUCTUATION.
*     ALSO FIND THE MEAN TEMPERATURE, SEE IF IT IS A FUNCTION
*     OF THE FREQUENCY.  SEARCH ONLY THE LAST FULL CYCLE.
      TCMAX = -1000.0
      TCMIN = 10000.0
      SUM = 0.0
      DO 399 J = 9*IRES+1,10*IRES+1
      SUM = SUM + TC(J)
      IF(TC(J).GE.TCMAX) TCMAX = TC(J)
      IF(TC(J).GE.TCMAX) JPHASE = J
      IF(TC(J).LE.TCMIN) TCMIN = TC(J)
      CYCLE = FLOAT(J-9*IRES-1)/RES
*      WRITE(5,30) CYCLE, TG(J), TC(J)
   30 FORMAT(F6.3,1X,F8.2,1X,F8.2)
  399 CONTINUE
*     APRIME IS THE AMPLITUDE OF THE THERMOCOUPLE
*     FLUCTUATION NORMALIZED BY THE GAS TEMPERATURE
*     FLUCTUATION; FOR THE STEADY PROBLEM, APRIME IS THE
*     STEADY TC NORMALIZED BY THE (CONSTANT) GAS TEMPERATURE.
      APRIME(K) = (TCMAX - TCMIN) / (2.0 * A)
      IF(K.EQ.1) APRIME(K) = TCMAX / T
*     PHASE SHIFT IS MEASURED BY THE LOCATION OF THE MAXIMUM
*     TEMPERATURE - ZERO DEGREES SHOULD OCCUR IF THE MAX IS
*     AT J = 1/4 CYCLE
      PHASE = -360.0/RES * FLOAT(JPHASE - (IRES*9+IRES/4+2))
      IF(PHASE.GT.0.0) PHASE = -360.0 + PHASE
      IF(F.EQ.0.0) PHASE = 0.0
      TMEAN = SUM / (RES+1.0)
      FACTOR = TMEAN / T
*      WRITE(5,35) TMEAN,TCMAX,TCMIN,APRIME(K)
   35 FORMAT(' TC TMEAN = ',F10.2,' K',/,
     &' TCMAX = ',F10.2,' K',/,' TCMIN = ',F10.2,' K',/,
     &' [TCMAX-TCMIN]/[2*A] = ',F10.4)
      WRITE(6,250) F, APRIME(K), PHASE, FACTOR
  250 FORMAT(1X,F6.1,7X,F7.4,2X,F7.2,5X,F10.4)
  299 CONTINUE
      CLOSE(5)
      CLOSE(6)
  999 RETURN
      END
*
*************************************************************
*
```

```
      SUBROUTINE PDF(XMIN,XMAX,X,KOUNTER,BINSIZE)
*
*     DIVIDE TEMPERATURE RANGE INTO 20 SUBRANGES.  SUM THE
*     NUMBER OF TIMES TEMP(I) FALLS INTO EACH SUBRANGE AND
*     NORMALIZE BY THE TOTAL NUMBER OF POINTS IN THE RECORD.
*
      IMPLICIT DOUBLE PRECISION (A-H,O-Z), INTEGER (I-N)
      DIMENSION X(200),KOUNTER(20)
      BINSIZE = (XMAX - XMIN)/20.0
*      WRITE(*,*) ' BIN = ', BINSIZE
      DO 90 K = 1, 200
      KNT = INT((X(K) - XMIN)/BINSIZE)+1
      KOUNTER(KNT) = KOUNTER(KNT)+1
  90  CONTINUE
*      FIND THE TWO LOCAL MAXIMA IN THE pdf NEAR THE TAILS
*      KLO = 1
*      KHI = 11
*     IDENTIFY THE HIGHEST PROBABILITY FOR THE LOWEST TEMP
*      DO 91 K = 10,1,-1
*      IF (KOUNTER(K).GE.KOUNTER(KLO)) KLO = K
*  91  CONTINUE
*      IDENTIFY THE HIGHEST PROBABILITY FOR HIGHEST TEMP
*      DO 93 K = 11,20
*      IF (KOUNTER(K).GE.KOUNTER(KHI)) KHI = K
*  93  CONTINUE
*      WRITE(*,95) TMIN+BINSIZE*(KLO-1),TMIN+BINSIZE*(KHI-1)
*  95  FORMAT(/,' pdf',/,' LOWEST TEMP ->',F7.2,/,
*     & ' HIGHEST TEMP ->',F7.2)
*       WRITE(*,*) ' LEAVING SUBROUTINE PDF'
       RETURN
       END
```

APPENDIX E UNCERTAINTY ANALYSIS

This appendix presents an uncertainty analysis for the measurements of gas flow rates, NO_x emissions, flame temperatures, and equivalence ratios (rotameter-based, probe-based, and optical). Uncertainties are calculated according to the method of root mean square addition. Uncertainties for certain variables are estimated statistically using 95 percent confidence intervals.

ROTAMETER CALIBRATIONS: Rotameter calibration uncertainties are affected by the uncertainty in the ambient pressure and temperature, displaced volume of gas, and elapsed time. Ambient temperature was measured with a mercury thermometer with an uncertainty of 1 °C in 300 K. Air pressure was known to the nearest 1 mm Hg in 760 mm Hg. These errors contribute to the uncertainty in correcting the measured flows to standard temperature and pressure conditions. The soap bubble meter for the methane rotameter calibration has a volume of 220 ml, and it can be read to within one 2 ml division. Although the electronic stopwatch has a resolution of 0.001 seconds, the reaction time of a human operator is approximately 0.020 seconds. The shortest elapsed flow time was about 10 seconds, for a time uncertainty of 0.2 percent. A final component of the uncertainty is the resolution of the scale for the rotameter float. The

full-scale uncertainty is one division in 150 divisions full scale. The uncertainty in the methane rotameter calibration is therefore

$$E_{CH_4} = \sqrt{E_{temp}^2 + E_{press}^2 + E_{vol}^2 + E_{time}^2 + E_{float}^2}$$

$$E_{CH_4} = \sqrt{\left(\frac{1}{300}\right)^2 + \left(\frac{1}{760}\right)^2 + \left(\frac{2}{220}\right)^2 + \left(\frac{0.020}{10.0}\right)^2 + \left(\frac{1}{150}\right)^2}$$

$$E_{CH_4} = 0.012 = 1.2 \textit{ percent.}$$

A dry gas flow meter was used for the air rotameter calibration. The resolution of the volume indicator is 0.01ℓ on a dial that records 1ℓ per full revolution. Although the same electronic stopwatch was used, reaction time is less important than the ability to recognize the precise arrival time of the dial needle at a division for very low flow rates. At the very lowest flow rates the needle creeped past each division on a time scale longer than the 20 ms reaction time of the stopwatch operator. The worst case uncertainty in the time measurement is estimated at 1 second in 200. The uncertainty in the air rotameter calibration is

$$E_{air} = \sqrt{E_{temp}^2 + E_{press}^2 + E_{vol}^2 + E_{time}^2 + E_{float}^2}$$

$$E_{air} = \sqrt{\left(\frac{1}{300}\right)^2 + \left(\frac{1}{760}\right)^2 + \left(\frac{0.01}{1.0}\right)^2 + \left(\frac{1}{200}\right)^2 + \left(\frac{1}{150}\right)^2}$$

$$E_{air} = 0.014 = 1.4 \textit{ percent.}$$

ROTAMETER EQUIVALENCE RATIO: When mixtures of air and methane are created, the uncertainty in the equivalence ratio is related to the uncertainty of the individually metered gas flows. The uncertainty in the equivalence ratio is

$$E_{\phi} = \sqrt{\left(E_{CH_4}\right)^2 + \left(E_{air}\right)^2}$$

$$E_{\phi} = \sqrt{(0.012)^2 + (0.014)^2}$$

$$E_{\phi} = 0.018 = 1.8 \textit{ percent.}$$

OPTICAL EQUIVALENCE RATIO: The optical system was calibrated using premixed flows from the air and methane rotameters. Therefore, the uncertainty in the optical measurement includes the uncertainty in the equivalence ratio of the mixture. A larger component of the uncertainty, however, is due to the signal drift over the course of an experiment. A statistical analysis of the drift estimates the 95 percent confidence limits as ± 0.09, or about ± 9 percent. While the resolution of the A/D board is another component of the uncertainty, it is negligible at one part in 4096. The uncertainty of the optical measurement of equivalence ratio is

$$E_{opt} = \sqrt{(0.018)^2 + (0.09)^2 + (0.0002)^2}$$

$$E_{opt} = 0.092 = 9.2 \textit{ percent.}$$

NO_x EMISSIONS: Uncertainties in the measured NO_x emissions arise from uncertainties in the calibration gas mixture, calibration drift, and resolution of the output meter. The calibration gas mixture was certified to ± 2 percent. Calibration drift was no more than one percent over the course of any experiment. The output scale of the meter could be read to one division in 100 divisions full scale. The uncertainty in the NO_x emissions is therefore

$$E_{NO_x} = \sqrt{(0.02)^2 + (0.01)^2 + (0.01)^2}$$

$$E_{NO_x} = 0.025 = 2.5 \textit{ percent.}$$

Note that this represents an estimate of the random error, and systematic errors from probe sampling technique and other possible sources are discussed in the main text.

PROBE-BASED EQUIVALENCE RATIO (THC ANALYZER): The uncertainty analysis for the THC analyzer is similar to that for the NO_x analyzer, but the individual components of the uncertainty are estimated to be smaller. The calibration mixture for the THC analyzer was the premixed flow from the air and methane rotameters, with an

equivalence ratio uncertainty of 1.8 percent. Calibration drift for the THC analyzer was low, less than 0.5 percent over the course of any experiment. The digital output meter has a resolution of one part in 200 parts full scale. The estimated uncertainty for the probe-based THC analyzer equivalence ratio measurements is

$$E_{THC} = \sqrt{(0.018)^2 + (0.005)^2 + (0.005)^2}$$

$$E_{THC} = 0.019 = 1.9 \textit{ percent.}$$

FLAME TEMPERATURES: Uncertainty in the flame temperature measurements is affected by the accuracy of the temperature correction terms, resolution of the A/D board, and uncertainty in the position of the thermocouple junction within the flame front. An estimate of the temperature correction term error is obtained by assuming an error in the junction emissivity of 33 percent and an error in the junction diameter of five percent. The root mean square of the sum of these errors (still about 33 percent) applies only to the correction added to the junction temperature. For the large thermocouple, the magnitude of the temperature correction term is 500 K for a junction temperature of 2000 K. The estimated uncertainty in the temperature correction term is therefore $\{(0.33)(500) / 2000\} = 0.083$, or 8.3 percent. Although the resolution of the A/D board is one part in 4096, the full range of the A/D board could not be used for the thermocouple readings. A/D resolution error is estimated to be about 1 part in 820 since only one-fifth of the full voltage range was used. Furthermore, the estimated uncertainty

of the amplifier gain is four percent. Combining these uncertainties results in a voltage uncertainty of essentially four percent. The random error in the positioning of the thermocouple probe is estimated by the largest spread in temperature measurements obtained from steady flames at the same equivalence ratio. This is roughly analogous to the 95 percent confidence intervals for the temperature measurements. This estimate is 80 K at a mean temperature of 2040 K, or four percent. The estimated uncertainty in the large thermocouple measurements is then

$$E_{temp} = \sqrt{E_{tcorr}^2 + E_{voltage}^2 + E_{position}^2}$$

$$E_{temp} = \sqrt{(0.083)^2 + (0.04)^2 + (0.04)^2}$$

$$E_{temp} = 0.10 = 10 \textit{ percent.}$$

The uncertainty in the fine thermocouple temperatures is expected to be lower, since the magnitude of the temperature correction terms is smaller and the positioning of the thermocouple is less critical outside of the flame. Uncertainty in the fine thermocouple temperatures is estimated at five percent, although this does not include systematic errors due to catalytic surface reactions and the extrapolation procedure. Since the mean temperatures of the fine thermocouple measurements were tied to the large thermocouple flame measurements in all manipulations of the data, the true uncertainty of the fine thermocouple measurements should also be estimated as ten percent.

VITA

Douglas Allen Wirth was born on September 27, 1964 in Baltimore, Maryland. He graduated as co-Valedictorian from Mount Hebron High School in 1982 and attended Virginia Tech in the following fall. While at Tech, he majored in mechanical engineering and graduated Magna Cum Laude. He participated in the cooperative education program for eight quarters with the Baltimore Gas and Electric Company. He is a member of Phi Delta Theta fraternity, and Tau Beta Pi and Pi Tau Sigma honor societies. He met Suzanne Scheid at Tech in 1984.

After graduation, he married Suzanne and returned to Virginia Tech for graduate school. He received his Master of Science in Mechanical Engineering in June 1989, having studied optical tomography and soot formation in flames. He then went to Cornell University to study infrared spectroscopy, but returned to Virginia Tech in January 1991 to continue his pursuit of the Ph.D. During this phase he spent the first half of 1993 living in Paris, France, pursuing theoretical aspects of his doctoral research at *Ecole Centrale Paris*.

Douglas A. Wirth

Douglas A. Wirth